MICROSTRUCTURE, WETTING ANGLE AND CORROSION OF ALUMINUM-SILICON ALLOYS

by

Shvetashva Suri

A Thesis Submitted in

Partial Fulfillment of the

Requirements for the Degree of

Master of Science

in Engineering

at

The University of Wisconsin-Milwaukee

December 2016

ABSTRACT

MICROSTRUCTURE, WETTING ANGLE AND CORROSION OF ALUMINUM-SILICON ALLOYS
by

Shvetashva Suri

The University of Wisconsin-Milwaukee, 2016
Under the Supervision of Professors Pradeep Rohatgi and Nathan Salowitz

In this study the effect of composition, surface roughness and water droplet size on contact angle and corrosion properties of cast Aluminum-Silicon alloys containing Si from 5% to 50% have been examined. The water contact angle was measured on a given sample using a goniometer. In addition, the effect of surface roughness and droplet size on contact angle has been measured for alloys at a fixed composition. The microstructures can be found in this report with sizes of primary and eutectic Silicon as well as inter-particle spacing between Silicon. Contact angle measurements are accompanied with a photographic validation of the water droplet contact angles on the goniometer. For the samples inspected, the contact angle was observed to generally increase with roughness and droplet size. The contact angle decreases with weight percent Silicon for samples roughened with 240 grit and 800 grit sand paper. For fully polished samples, no clear trend was observed with weight percent Silicon. Lastly, the corrosion current was measured on all samples in both abraded state and fully polished state and these values were compared to comment on the change in resistance to corrosion with weight %Si and change in state of polish. No systematic variation in the corrosion potential or current was observed with weight percentage of Silicon (Si). However, a relative peak in corrosion resistance was observed for Al-22%Si for both abraded and polished samples.

To my parents and teachers

TABLE OF CONTENTS

LIST OF FIGURES

LIST OF TABLES

ACKNOWLEDGMENTS

In the course of doing this research I have had cause to interact with a lot of people whose goodwill, help, advice and directives have been very helpful. It is in this regards that I want to acknowledge my research advisors, the indefatigable Professor Pradeep Rohatgi, who has been pivotal to the completion of this work and Dr Nathan Salowitz, a leading light in the area of mechanics of materials. His insights and suggestions have been quite helpful. I would also like to thank National Science Foundation (NSF) for funding my work from January 2016 to May 2016. I will not fail to mention Dr. Afsaneh Dorri Moghadam and Dr. Meysam Tabandeh Khorshid. These two people were always willing to answer my questions, give advice and comment on my work at various times. At this point, I would also like to thank Behnam Gohari for providing me insight into this field along with the help he offered for analyzing my work. I would like to thank my very good friends Zhongying Wang and Huali Han for providing me all the help required in finishing this thesis along with moral support.

Some other people worth acknowledging are members of my family that have always stood by me in all my endeavours. They include ; my mother, Mrs Suniti Suri for her constant moral and domestic support; my father Mr. V.K. Suri; my sister Sheifaly ; and my brother in-law, Mr. Winiston K. Jose. In the course of my studies I have had friends and colleagues whose encouragement added value to the research. As such, I am grateful to such friends and colleagues like John Mortimer, Guy Reynolds, Kyle Brown, Michael Beining and Seena. I indeed owe all of you a world of gratitude and for this I say thank you.

1. Introduction

To reduce weight in automotive and aerospace industries, for economic and environmental reasons, Aluminum-Silicon (Al-Si) alloys have become a widely used. Al makes the component lighter and Si improves the working conditions at ambient and temperatures up to 200^{o}C. Together, they give the machine components excellent characteristics such as low cost machinability, castability, high specific strength and recyclability [1].

Aluminum (Al) with Silicon (Si) as the major alloying element forms a major component of all castings produced and have a wide range of application in automotive, marine and aerospace industry due to their qualities like castability, mechanical properties, corrosion resistance and wear resistance. In addition, minor amounts of alloying elements such as Copper (Cu) and Magnesium (Mg) are added to improve mechanical properties and to improve response to heat treatment especially in hypoeutectic alloys. The aim of this work is studying the role of composition and morphology of microstructural constituents (e.g. size of primary Silicon and eutectic interdendritic Al-Si) on wetting properties and corrosion of Al-Si based casting alloy at standard environmental conditions.

The most common alloying elements added to Al-Si alloys are Cu and Mg, to improve mechanical strength and ability to be heat treated at elevated temperatures [2]. However, Cu and Mg are present in lesser amounts in hypoeutectic alloys such as A356, A360 and A368 used in this study and to simplify the study, material was classified by its major alloying element, silicon. These hypoeutectic alloys were selected because they had a substantial amount of Si as compared to other components. The microstructure of these casting alloys consists of α-Al

dendrites surrounded by eutectic Si and many intermetallic phases such as Al_2Cu, Mg_2Si, Fe-bearing phases etc. The morphology governs the mechanical properties, which in turn is affected by the cooling rate or modification of chemical composition (e.g. %Si content) [3]. Use of these alloys above 230^{o}C is limited due to the hardening of Si phases and dissolution of Cu- and Mg-phases [3].

1.1 Al-Si Alloys

As discussed in the previous section Al-Si alloys comprise about 85-90% of the total Aluminum-cast products produced [4]. Although use of these alloys comes with excellent wear resistance, fluidity, pressure tightness and shrinkage, they also come at the expense of machinability and welding characteristics [4].

The Al-Si equilibrium diagram is characterized by two phases: hypoeutectic (having the alloying element Si in an amount less than 12.6 wt.%) and hypereutectic (containing more than 12.6 wt.% Si). The hypoeutectic alloys exhibit good corrosion resistance and castability but not very good wear resistance. The hypereutectic alloys such as 390 and 393, containing 15-25% silicon exhibit remarkable wear resistance and low Coefficient of Thermal Expansion (CTE), a property much desired in metallic structures [4].

Fabrication process of Al-Si alloys is the quality control step for making quality Al-Si alloys. The factors involved in governing the mechanical properties of these alloys are microstructure and alloy constituents [4]. Grain size, silicon morphology and dendritic arm spacing are some of the critical microstructural features [4]. Sodium (Na) is normally added to improve the structure because addition of sodium does not usually modify the morphology of the eutectic phase, but forms intermetallic Al-Si-Na that provides useful properties [5]. Titanium (Ti), boron (B) and phosphorus (P) are added for grain refinement and modification to the solidification front [4].

Since their machinability is not so good as such, it can be improved by making the Si particles finer and more evenly distributed [4]. Further improvement in properties of these alloys can be achieved by additions of small amounts of other alloying elements such as copper (Cu), magnesium (Mg), zinc (Zn) and nickel (Ni) [4]. For example, good casting properties are achieved in hypoeutectic alloys by the addition of silicon but addition of copper improves tensile strength, thermal conductivity and machinability but a reduction in ductility and corrosion resistance [4]. The iron (Fe) and manganese (Mn), present in hypoeutectic alloys, interact to cause different morphologies in the pressure die casting process, causing a coarse morphology in the shot sleeve region and a compact one in the die cavity in the Fe-rich phase.

Al-Si alloys are very attractive because of their ability to refine grains, flexibility in casting components, modifying structures and application properties. Recently, new methods and designs are being developed to improve and implement these advantages for synthesizing composite materials using Al-Si alloys [4]. Table 1 below shows the composition of the two hypoeutectic alloys A-356 and A-360 which were used in this study.

Table 1: Composition of hypoeutectic Al-Si alloys

Alloy Type	Silicon Min-Max%	Magnesium Min-Max%	Copper Min-Max%	Manganese Min-Max%	Zinc Min-Max%	Iron Max%	Trace Max%
A356	6.5-7.5	0.2-0.4	0.2-0.4	0.35	0.35	0.6	0.15
A360	9-10	0.4-0.6	0.6	0.35	0.5	1.3	0.25

1.2 Wettability

A superhydrophobic surface is one which can repel water and moisture and can be applied in making self-cleaning surfaces. Some examples of superhydrophobic surfaces are leaves of Nelumbo nucifera (lotus leaves), Colocasi esculanta leaves, duck feathers and butterfly wings [4]. Superhydrophobic surfaces have been applied in fluid industry and water transfer systems for protection from fouling and inclusion of hazardous material in the flow systems [4].

To achieve self-cleaning with respect to a liquid, differential wettability of the surface is achieved which can be done by altering two parameters, namely, chemical composition of the surface and surface roughness [5,6]. An important parameter quantifying the wettability is the contact angle made by that liquid. Contact angle is defined as the angle made at the solid-liquid interface by the tangent to the liquid-vapor interface which is measured through the liquid [7]. For a surface to be repellant to wetting by a liquid, the contact angle made by that liquid should be greater than 90^{o}. Although making changes to the surface features is a more cost effective and promising approach to making surfaces self-cleaning, several other methods to increase the water contact angle have also been used, which include coating with a low surface energy material [8,9], spray atomization [10], micromachining, or etching with low surface energy molecules [12,15].

Components in water distribution systems such as valves, pumps, plumbing fittings and meters experience fouling such that these components get blocked due to the build up of water-borne contaminants [4]. Since these components are usually metallic, these blockages cause the material to be deteriorated over time in addition to causing inadequacy and inaccuracy in the flow [4]. Imparting self-cleaning and less wettable characteristics to these surfaces can enhance anti-fouling and corrosion resistant characteristics of these components which could lead to their better service conditions [4].

2. Background

2.1 Theoretical Consideration

There are two theoretical models used to describe the wetting of a solid substrate by a water droplet. The first model is one in which entire water droplet is in contact with the solid substrate called the Wenzel type of contact, in which the contact angle (CA) of a water droplet θ_W is given by equation (1) [7].

$$\cos\theta_W = R_{fw} \cos\theta_O \quad (1)$$

The second model is the rule-of-mixtures model in which there can be air gaps present in between the liquid and the solid substrate [7]. In this case the contact angle θ_{CB} of a liquid droplet with a surface composed of two different fractions is described by equation (2).

$$\cos\theta_{CB} = f_S \cos\theta_S + f_W \cos\theta_W \quad (2)$$

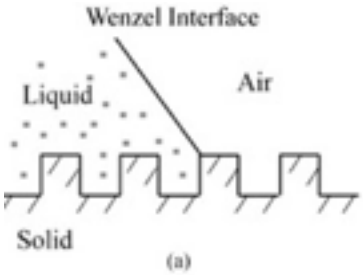

Figure 1: Schematics of configurations described by the Wenzel equation for the homogeneous interface, [13].

Figure 1 shows a schematic of the Wenzel model. θ_O in equations (1) is the contact angle for a completely smooth surface,. In the Wenzel model, the roughness factor, R_{fW}, is defined as the ratio of actual surface area to flat projected surface area [4]. Higher R_{fW} makes a hydrophilic surface more hydrophilic (θ_O is less than 90^o) or makes a hydrophobic surface more hydrophobic ((θ_O is gretaer than 90^o).

It has been studied by Gao and McCarthy [7] that the contact angle depends on the interaction of the solid and liquid at the three phase interfacial line and not at the entire interfacial or contact area. In the case of the uniform surface, the fraction of the length of the solid/water interface, $L_{SW}/L_{SW} + L_{WA}$, can be determined from solid/water contact area, A_{SW}, and the total contact area, $A_{SW} + A_{WA}$, according to Equation (3).

$$fsw = \frac{Lsw}{Lsw + Lwa} \approx \frac{Asw}{Asw + Awa} \tag{3}$$

The fraction of water can be determined using the fact that $f_{SW} + f_{WA} = 1$, it can be defined in terms of f_{SW} according to Equation (4).

$$fwa = \frac{Lwa}{Lsw + Lwa} \approx \frac{Awa}{Asw + Awa} = 1 - fsw \tag{4}$$

It has also been studied that metals and alloys (e.g. Al-Si alloys) have heterogeneous chemical composition and microstructure at the surface [8] e.g. grains occur in different orientations and different sizes ranging from micrometers to nanometers in polycrystalline metal surfaces. Different planar faces along the crystal interfaces have different surface energies and therefore different contact angles [9-11]. However, McHale [12] points out that in order for equation (2) to be valid, the droplet size should be large enough as compared to the features of a uniform surface so that the entire interfacial area can be considered the same.

2.1.1 Fundamentals of Contact Angle

Contact angle is the appeared angle between the droplet and the solid surface under equilibrium [13]. The equilibrium contact angle is specific for any given system and is a function of the

interfacial energies or the surface energies at the interface of solid-liquid, solid-air and liquid-air interface. The Young-Laplace equation helps to determine the shape of the droplet and the contact angle plays the role of the boundary condition [13]. Figure 2 shows the contact angle as the angle between tangents to solid-liquid interface and liquid-air interface.

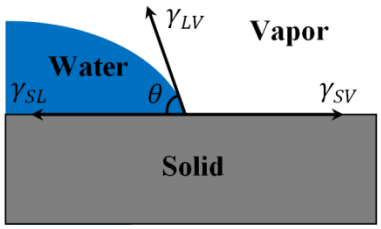

Figure 2: A water-vapor surface coming to the solid surface at the contact angle of θ.[14]

The net energy change for the propagation of the liquid front for an infinitesimal distance *dx* when a liquid droplet in contact with a solid surface making a contact angle θ is equal to $(\gamma_{SL} - \gamma_{SV} + \gamma_{LV}\cos\theta)dx$, where γ_{SL}, γ_{SV} and γ_{LV} are solid-liquid, solid-vapor and liquid-vapor interfacial energies, respectively. Thus, for the liquid droplet to be in equilibrium, the contact angle is given by

$$\cos\theta = \frac{\gamma_{SV} - \gamma_{SL}}{\gamma_{LV}} \tag{6}$$

Equation (6) is called the Young-Laplace equation. From equation (6), it can be seen that three situations are likely. If $(\gamma_{SV} - \gamma_{SL})/\gamma_{LV} > 1$, equation (6) is not valid but for this special condition the situation corresponds to that where the liquid droplet completely wets the solid substrate (θ=0^o). If $(\gamma_{SV} - \gamma_{SL})/\gamma_{LV} < -1$, again the equation (6) is not valid but for this special condition the liquid is completely repelled by the solid surface (θ=180^o), and the last situation is when $-1 < (\gamma_{SV} - \gamma_{SL})/\gamma_{LV} < 1$ in which $0 < \theta < 180^o$.

2.1.2 Wenzel model

The equation that governs the contact angle on a rough surface is given by the Wenzel model taking into account the effect of roughness. If we take into account the asperities and the pits on

a rough surface, then compared to a smooth surface the rough surface will have more interface area. A non-dimensional roughness factor $R_f > 1$ relates the contact angle on a rough surface, θ, to the contact angle on the smooth surface, θ_0, using surface force balance and empirical consideration.

$$\cos\theta = \frac{dA_{SL}}{dA_F}\frac{dA_{LA}}{dA_{SL}} = Rf\cos\theta_0 \tag{7}$$

$$R_f = \frac{A_{SL}}{A_F} \tag{8}$$

Equation (7) is called the Wenzel equation.*'A*' in equation (7) refers to the area, 'SL' refers to solid-liquid interface, 'LA' refers to the liquid-air interface and 'F' refers to the flat projected area. R_f, called the roughness factor as described previously is equal to the ratio of the total surface area , A_{SL}, to the flat projected surface area, A_F [13]. The dependence of contact angle on the roughness factor R_f for a different value of θ_0 is shown in figure 3. The Wenzel model predicts that with an increase in R_f, a hydrophobic surface ($\theta_0 > 90°$) becomes more hydrophobic while a hydrophilic surface ($\theta_0 < 90°$) becomes more hydrophilic [13].

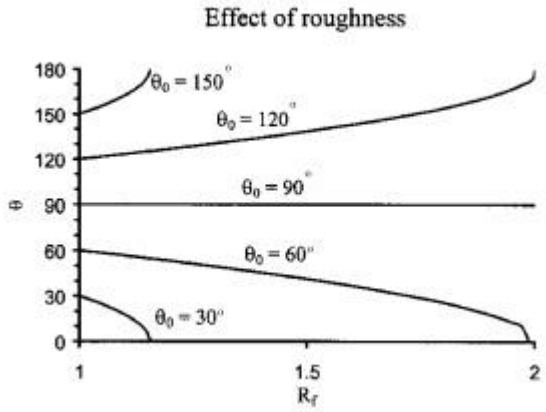

Figure 3: Contact angle for rough surface (θ) as a function of the roughness factor (R_f) for various contact angles of the smooth surface (θ_0) [14].

2.1.3 Rule of Mixture model

The rule of mixture gives the contact angle for a surface composed of two different phases, one with a fractional area f_1 and contact angle θ_1 and the other with fractional area f_2 and contact angle θ_2, so that $f_1 + f_2 = 1$ [13]. The contact angle is given by the following equation:

$$\cos\theta = f_1 \cos\theta_1 + f_2 \cos\theta_2 \quad (9)$$

The rule of mixtures on a macroscopic scale where part of a drop is in contact with air and part with water. The microscopic rule of mixture is where part of the drop is in contact with air and part with silicon and the sizes of entities are in micron scale.

Two situations in wetting of a rough surface should be distinguished: the homogeneous interface without any air pockets shown in figure. 2(a) (called the Wenzel interface, where the contact angle is given by the Wenzel equation or Eq. 7), and the composite interface with two different fractions (called the rule of mixtures).

2.2 Al-Si Microstructure

The solidification process of Al-Si alloys occurs by the primary precipitation of dendrites. The solidification structure of hypoeutectic Al-Si is shown in figure 4 showing the α-Al dendrite structure in eutectic Al-Si. The primary aluminum grows in the <100> planar direction in hypoeutectic Al-Si. The dendrtitic structure consists of four secondary arms growing around a main primary arm. This is true for simple cubic structures [15].

For the cooling process of a molten metal a term undercooling is used which is to cool molten metal without forming crystals to a temperature below that at which crystallization normally takes place. The undercooling depends on the cooling rate, the concentration of the alloying element in the melt and the type of the alloying element [15]. It is a well-established fact that

undercooling increases with increasing concentration of the alloying element and with increasing cooling rate [15].

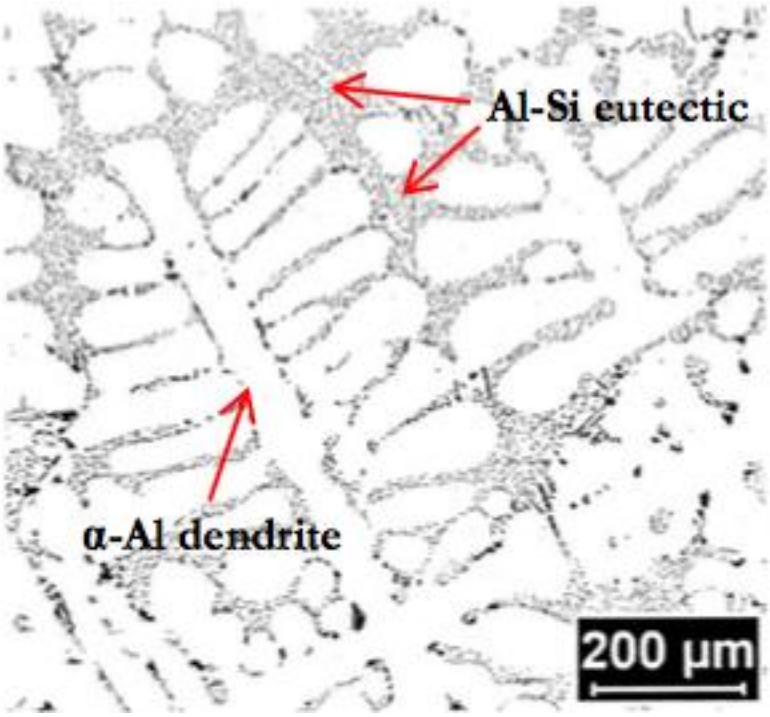

Figure 4: Solidification structure of hypoeutectic Al-Si alloy [36].

As the solidification process continues, Al and Si in the liquid mixture precipitate out simultaneously in equilibrium with the liquid mixture at constant temperature. This mixture is called Al-Si eutectic mixture [16-18]. For Al-Si system, this eutectic point is at 12.6 wt. % Si and a temperature of 577ºC. This point is shown on the phase diagram of Al-Si in figure 5. While referring to Al in solution with Si, a term called α-Al is used instead of pure Al. This is because Al exists in a form which dissolves 1.6 wt. % Si and this is the maximum solubility of Si in Al [22]. The solubility of Al in Si is almost negligible. [22].

Commercial Al-Si alloys, especially hypoeutectic, ones contain Cu and Mg in addition to Si. This leads to a more complicated morphology, solidification structure and process of these alloys. There is formation of intermetallic compounds in the microstructure due to the presence

of Cu, Mg and Fe after eutectic formation [22]. The most common intermetallic compounds and phases are Al_2Cu, Mg_2Si, α-$Al_{12}(Fe,Mn)_3Si_2$ and β-Al_5FeSi [22]. The morphology and features of microstructural constituents is affected by cooling rate, e.g. increasing cooling rate makes all microstructural features refined, decreases SDAS (secondary dendrite arm spacing), changes the eutectic Si into small rounder particles from elongated plate-like structure and also decreases the size of intermetallic compounds [22].

As has been observed and discussed in literature, increase of the solute content also refines the secondary dendrite arm spacing (SDAS) [22]. For Al-Si alloys, especially the hypoeutectic ones, the finer dendritic arm spacing leads to a more extensive distribution of Si in the interdendritic region. This property improves the tensile strength and is more prominent in hypoeutectic alloys with higher Si content, e.g. Al-9 wt. %Si [22].

As described earlier, an increase in solute content leads to a more refined secondary dendrite arm spacing which leads to better mechanical properties [24]. The microstructure of hypereutectic Al-Si alloys consists of dendritic α-Al surrounded by eutectic interdendritic Al-Si phase which is formed by Si distributed in the Al-rich phase, as an irregular phase. The eutectic mixture contains soft Al as matrix and the amount of eutectic mixture depends on level of Si [22].

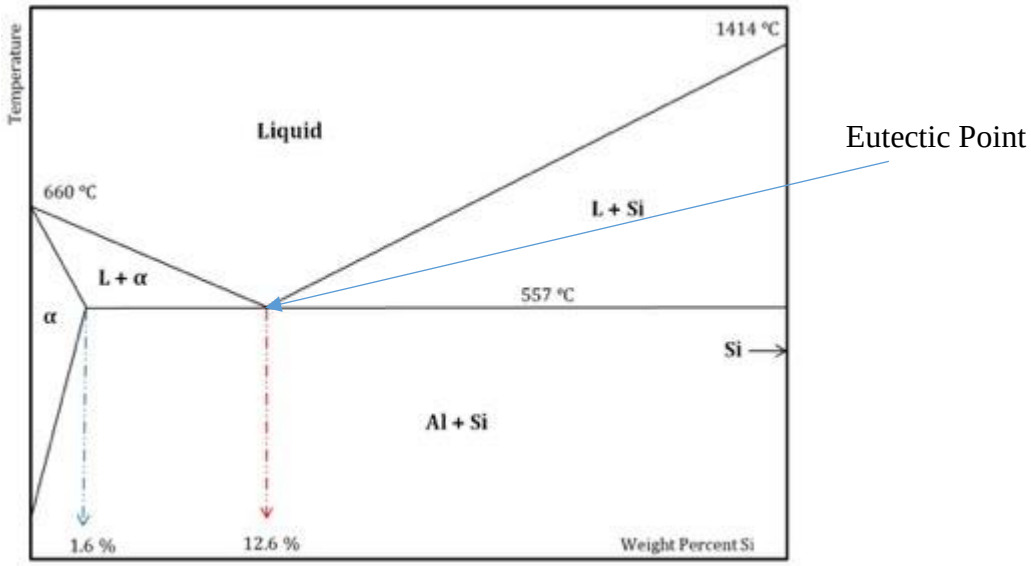

Figure 5: The schematic phase diagram of Al-Si.

2.3 Creating Surface Roughness

Some methods for creating surface roughness on metal surfaces are etching, deformation, electrolytic deformation such as anodization, and lithography most of which are not easily scalable to industry level. Creating surface roughness by adding another material as a coating is usually not mechanically reliable as it usually lacks mechanical durability. So, methods such as surface etching with acid solution or mechanical abrasion should be used. The surface of solids is usually heterogeneous as far as the structure and chemical composition are concerned. If the heterogeneities occur on a scalable length, then it is possible to create surface roughness using a selective etching technique. According to Vahid Hejazi [35] et al, in polycrystalline materials, nanoscale structures can be created at the top of microscale pillars because grain boundaries as well as the grain surfaces are attacked by the etchant to create nanoscale pores. However, roughening a surface by rubbing it against sand paper of suitable roughness creates microscale order of roughness. In this study, microscale roughness was created using mechanical abrasion while etching was not used.

2.4 Previous Work Done

Experiments have been performed and various techniques have been developed to change the wetting properties of surfaces. For composites, concretes and ceramics, introducing superhydrophobic materials in the bulk rather than on surface would make them waterproof [14]. The same methods can be used for polymers as well. Especially for underwater applications, experimental data have been collected and models have been tested, which show a good agreement with each other. Thus, these models can be used to design novel superhydrophobic composite materials.

It is more difficult to make superhydrophobic surfaces using metals than polymers and ceramics, because they have higher surface energies than polymers and ceramics [14-16]. A number of advances, however, have been made in the field of superhydrophobic metallic materials. For example, in 1950s, Bikerman [17] tested the wetting characteristics of stainless steel surfaces with different surface finishes and with contact angles around 90^{o} and concluded that increasing the surface roughness increases the resistance of water droplets to sliding. Qian and Shen [18] created surface roughness by chemical etching on surfaces of Al, Cu and Zn and studied its effect on wetting characteristics of these materials. The etchant used was a mixture of hydrochloric acid (HCl), water (H_2O) and hydrofluoric acid (HF) at room temperature. Shirtcliffe and McHale [19] made superhydrophobic Cu based surfaces using a coating and investigated the wettability characteristics of these surfaces. Sommers and Jacobi [20] achieved "anisotropic wettability on Al surfaces by altering the surface microtopography".

B_4C particles have been added to molten Al-7 wt%Si-0.3 wt% Mg alloys, at levels of 5 and 10 wt % using proprietary potassium-aluminum-titanium-fluorine (K-Al-Ti-F) flux [20]. The resulting composites were then tested mechanically and metallographically in the as-manufactured state and after heat treatment for 48 hours at $500^{o}C$ and $700^{o}C$ [20]. Many

properties were improved such as increase in stiffness, increase in modulus per unit volume percent particles added. Although little change in mechanical properties was observed by reaction at 500^{o}C but due to heat treatment at 700^{o}C an increase in stiffness and a decrease in ductility was observed due to an increase in volume fraction of stiff and brittle phases. Apart from these, properties of particulate Al-Si composites have been studied by J.U. Ejiofor and R.G. Reddy [4]. In addition, work has been done at UWM by Vahid Hejazi and Aneidi Nyong on wetting and investigation of superhydrophobicity of composite surfaces and Cu alloys respectively.

2.5 Problem Statement

The objective is to study the effect of composition, microstructure, size of water droplet and surface roughness (by varying the grit number of sand paper) on wetting angle and corrosion behavior of Al-Si alloys. This study will help identify the microstructure and compositions with higher contact angles and corrosion rates.

2.6 Approach and Major Tasks

This combination of Al and Si materials was used because while aluminum is a low-weight, inexpensive, and easy-to-work metal, silicon is easy to clean, and offers more mechanical strength and a combination of these is very suitable for marine, aerospace and automobile applications. Al-Si alloys are a major component of marine industry, so their corrosion and wetting properties become important.

Approach to be followed is that experiments will be conducted on common aluminum silicon alloys with varying surface roughness and water droplet size to determine the resulting contact angles. Data will be analyzed across parameters of silicon content, sand paper grit used to roughen the surface, and water droplet size to determine what factors are important and trends exist.

The approach to be followed consists of the following major tasks:-

1. Preparation of samples from the metal plates obtained from Mercury Marine
2. Mechanical abrasion of prepared samples using polishing with different grit number sand papers.
3. Giving a wait time of 24 hours to all the samples to allow a uniform formation of oxide layer on their surface.
4. Measurement of contact angles on the polished samples.
5. Re-polishing the samples to the fully polished state using 1μm Alumina slurry.
6. Giving a wait time of 24 hours again for the formation of uniform oxide layer.
7. Measurement of contact angle on fully polished samples.
8. Observation of microstructure of each fully polished sample under optical microscope.
9. Preparation of fresh samples (with same %Si as in samples prepared in step 1) from the Mercury Marine samples by polishing them with 400 grit sand paper.
10. Again giving a wait time of 24 hours after polishing before doing the corrosion test on the samples.
11. Doing corrosion test on these samples using corrosion cell and potentiostat.
12. Re-polishing these samples to fully polished state using 1μm Alumina slurry.
13. Giving a wait time of 24 hours between polishing and doing the corrosion test.
14. Doing the corrosion test on the samples in the fully polished state.

3. Experimental Section

To determine which wettability model best applies to the Al-Si samples under consideration and observe the influence of second-phase effects on wettability, experiments are conducted on aluminum-silicon alloys of varying silicon content. The studies were performed in atmospheric air, allowing time for native oxide layers to form as would be representative of components in

working conditions.

Major tasks perfomed for experimental work has been discussed below:

3.1 Sample Preparation.

Aluminum-silicon samples were obtained from Mercury Marine in the form of 5 mm thick metal plates. Sample preparation was started by first sectioning off 2 cm x 2 cm square pieces from the 5 mm thick metal plates. Finally, to obtain well-supported samples, these pieces were mounted on hot phenolic resin using a Buehler hot phenolic mounting machine.

3.2 Mechanical Abrasion.

After mounting the samples, the next step was grinding the samples to obtain the required surface finish. The required surface finish was obtained by polishing the samples using sand papers with 240, 400, 600, 800 and 1200 grit numbers. This was done by first mechanically abrading the sample starting with the roughest sand paper (240 grit) to the finest grit (1200). The higher the grit number, finer is the surface finish provided by it, because grit number is a reference to the number of abrasive particles per square inch of sand paper. After polishing all samples with 1200 grit sand paper, micro- and nanoscale roughness was obtained by abrading each aluminum sample with one of the six grit size pieces sand paper for 30-60 s by rubbing the samples against sand paper pasted on a Buehler grinding wheel rotating at about 200 rpm. This process employed is called polishing. After polishing the samples, they were kept in a desiccator for about 24 hours to allow a uniform layer of oxide to be formed on them. After that, the samples were taken for measuring contact angle on them. After contact angle had been measured to obtain fully polished surface the samples were polished with a soft cloth impregnated with 1 μm alumina. This was done to enable microstructural analysis of the samples using optical microscope. Corrosion testing of the samples was done after microstructural analysis.

3.3 Wetting Measurement with Different Sized Water Droplets

After the polishing the samples, they were taken to the Self-Organization, Green and Biomimetic Tribology Laboratory in University of Wisconsin-Milwaukee with a Rame Hart 250 model [38] goniometer. Contact angles were measured for each sample at least three to four times until a consistent value was obtained. For each sample 4 μL, 6 μL, 8 μL and 10 μL droplets of Aquafina bottled water were used to measure contact angle. For each droplet size a minimum of three readings was taken. For each measurement a new droplet was used from the dropping syringe. Each droplet was placed at a different spot. In between placing the droplets, the last droplet was wiped with a soft tissue paper. The contact angle reported and used in the graphical plots is the average contact angle of the measurements made for each size. Rame Hart 250 model goniometer was used for measuring the contact angle shown in figure 6 below.

Figure 6: Rame Hart 250 model goniometer.

3.4 Microstructure Investigation

For understanding the variation of contact angle with %Si content, the microstructure of all Al-Si samples was measured under an optical microscope with a Nikon TSL100 camera and Clemex Vision V5 [40] software. The microstructure was observed under this microscope. The

size of primary Silicon was measured. The interparticle spacing between primary Silicon was also measured. The eutectic Silicon dispersed in the Al matrix was also observed. The interdendritic spacing of eutectic Silicon was measured. The size of eutectic Silicon was also measured as shown in figure 7. The microstructure was analyzed at 200x and the length measurement tool of Clemex Vision V5 [40] software was used to measure the size of primary Silicon, length of longest interdendritic eutectic Al-Si and spacing between eutectic Al-Si.

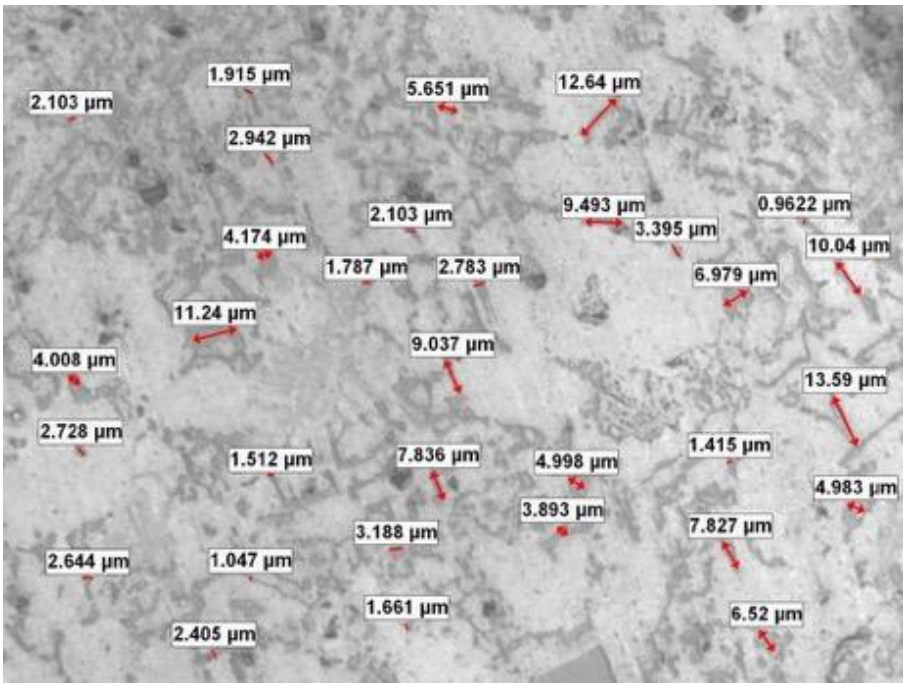

Figure 7: Microstructural analysis showing size of interdendritic eutectic Al-Si in Al-24%Si

The pictures of microstructural analysis of all Al-Si samples have been shown in Appendix B.

3.5 Investigation of Corrosion Behavior

The corrosion tests were performed with the following steps: It started by preparing a solution of 1 kilograms of Distilled Water and 35 grams of Sodium Chloride (3.5% of Distilled Water), adding both components and then mixing it. 3.5% NaCl solution was used because this solution best represents sea water, against which the corrosion testing needs to be done and the actual application of the material is set. These conditions at which test are done including the

concentration of solution are as per ASTM standard G50-10 (2015). After preparing the solution, the Corrosion Cell (manufactured by Biologic, capacity 250 ml [41]) started to be prepared by placing and fixing the working sample (Al-Si alloys) in a way its polished side faces the solution inside the Cell. Then the solution was poured into the Cell, and finally the Potentiostat (BioLogic SP 200 [41]), including the Reference electrode (Calomel) and the Counter electrode (Pt), was connected to the Cell. A Potentiostat is an electronic equipment which consists of and controls three electrodes and is used to run several electrochemical experiments. The potentiostat maintains the potential of the sample under observation or the working electrode in comparison to a reference electrode. This is done by altering the current at an auxiliary circuit consisting of a counter electrode. Figure 7 below shows a schematic of the potentiostat with CE as counter electrode, WE working electrode and Ref as reference electrode.

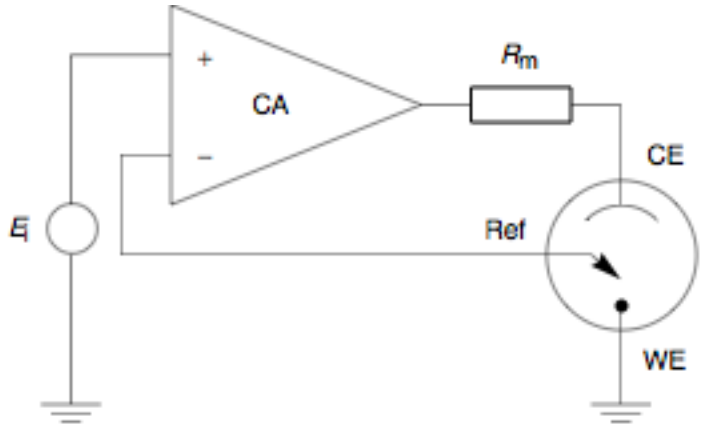

Figure 8: Schematic of a potentiostat. [50]

The Al–Si samples were fixed at working end of the glass corrosion cell such that 1 cm^2 of the sample was in contact with the electrolytic solution in the cell. With the experiment set up, the software EC-LAB version V10.33 was executed to start the analysis of the corrosion test. "Generalized corrosion (GC)" was set as the parameter setting of the corrosion test. The open circuit voltage of the working electrode called E_{oc} was checked till it became stable. After that,

the graph to be displayed was adjusted to be "E_{we} vs. log[i]", where 'we' refers to working electrode and 'i' is the current running in the corrosion cell, and selecting the folder where the analysis will be saved, the corrosion experiment could be started.

After an hour of running the potentiostat and the EC-LAB software, each test was done and ready to be analyzed. After running the test the "Tafel fit curves" also known as "potentiodynamic polarization curves" were obtained. The analysis of this data was done by copying the analysis data and the data of the experiment to an excel document, and creating a graph, using "Ewe" and "log (|<I>/mA|)" as coordinates for the data of the test, in it. After the Tafel analysis, the software gives the output in the form of E_{corr} and I_{corr}. which represent the corrosion potential and the corrosion current flowing through the sample.

4. Results and Discussion

4.1 Theoretical predictions of CA

The contact angle on a rough surface, θ, is related to the contact angle on the smooth surface, θ_0, using surface force balance and empirical considerations, through the non-dimensional roughness factor $R_f > 1$. This relation is shown in equation (7) in section 2.1.2. R_f is equal to the ratio of the surface area, A_{SL}, to its flat projected area, A_F [13].

R_a, which is used to calculate R_f, is defined within an evaluation length as the average of the height deviations above and below the mean line, and is calculated over that length. The relationship between the R_a and R_f is not straight forward due to the chaotic irregularity of the abraded surface generated and therefore, for the purpose of explaining the results, we assume that the non-dimensional R_f change with R_a [measured in micrometers], is given by the relationship[14]:

$$R_f = R_a/(3 + 0.5\ R_a) + 1 \qquad (10)$$

Table 2: Contact angles for fully polished (smooth) surfaces of various compositions of Al-Si alloys

Alloy Composition	Contact angle for fully polished samples θ_o
Al-22%Si	70.35
Al-24%Si	71.81
Al-25%Si	78.03
Al-32%Si	74.91
Al-50%Si	61.53

In table 2 the measured contact angle values for smooth surface of samples has been provided. These values were used in calculating the theoretical contact angles using Wenzel model in the following pages.

Mechanical abrasion of the surface with SiC paper results in the increase of the average surface roughness hence the roughness factor, R_f. Table 3 on the following page shows the values of measured contact angles as well as contact angles predicted by Wenzel model for different Al-Si alloys. The measured angle was averaged across all droplet sizes measured. Droplet size is known to have an effect on contact angle but is not accounted for in the Wenzel model. Outlier data was also excluded.

Table 3: Calculation of R_f value from R_a and prediction of CA from Wenzel model

Composition	Sand paper grit	R_a	R_f	Contact angle for smooth surface	Measured contact angle	Wenzel predicted Contact angle
Al-22% Si	240	0.58	1.18	70.35	71.73± 3.02	67.19
	400	0.342	1.11	70.35	74.98± 2.36	68.58
	800	0.26	1.08	70.35	65.29± 1.38	68.64
Al-24%Si	240	0.5	1.15	71.81	73.74± 0.47	68.89
	400	0.328	1.10	71.81	80.70± 2.66	69.85
	800	0.28	1.09	71.81	67.9± 1.00	70.12
Al-25%Si	240	0.72	1.21	78.03	71.04± 1.22	75.41
	400	0.7	1.21	78.03	73.22± 1.83	75.48
	800	0.5	1.14	78.03	65.54± 2.64	76.29
Al-32%Si	240	1.22	1.33	74.91	67.70± 1.65	69.62
	400	0.546	1.17	74.91	72.41± 1.33	72.32
	800	0.38	1.12	74.91	62.14± 1.98	73.06
Al-50%Si	240	0.86	1.25	61.53	65.55± 2.12	53.4
	400	0.78	1.23	61.53	65.13± 3.61	54.1
	800	0.46	1.142	61.53	72.5± 2.18	57

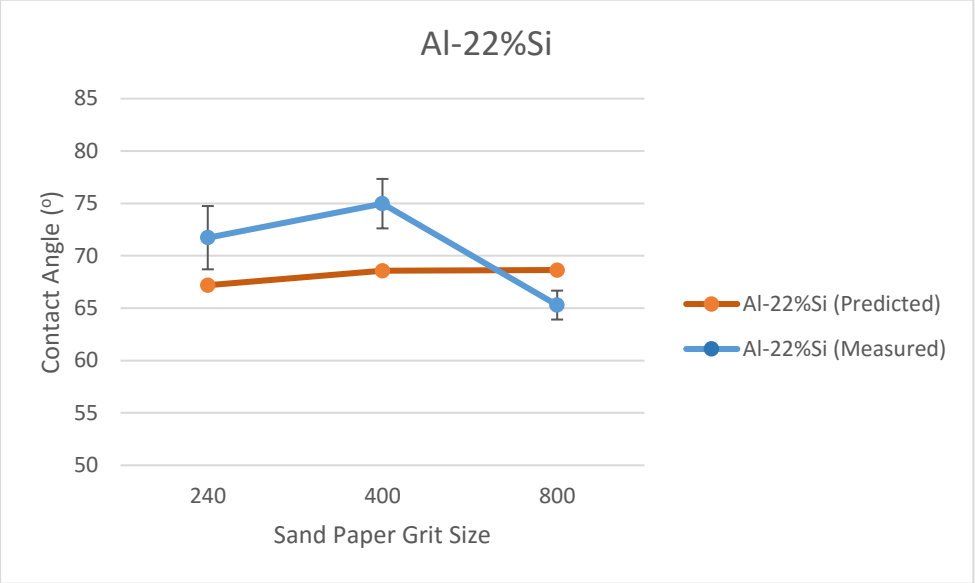

Figure 9: Comparison of experimental and Wenzel predicted contact angles for Al-22%Si

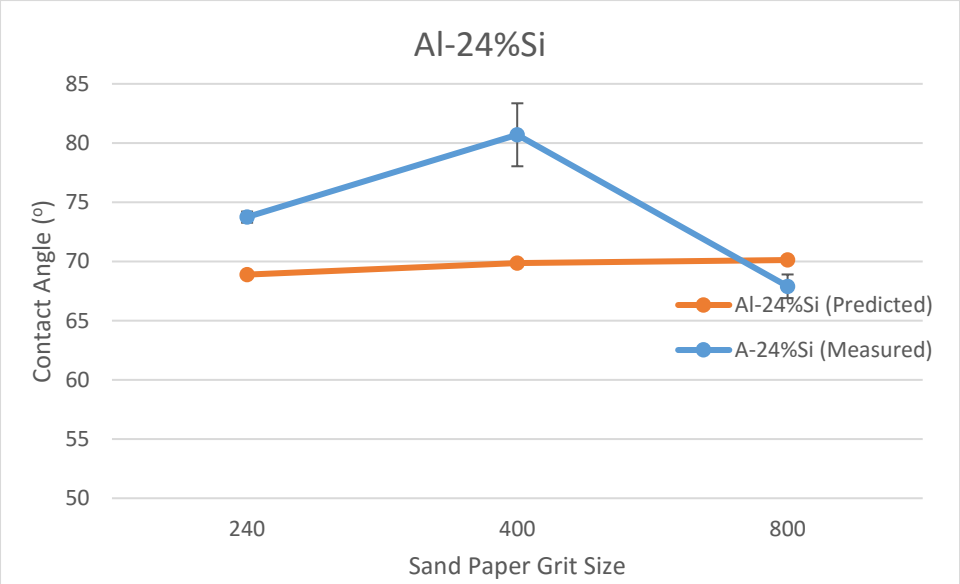

Figure 10: Comparison of experimental and Wenzel predicted contact angles for Al-24%Si

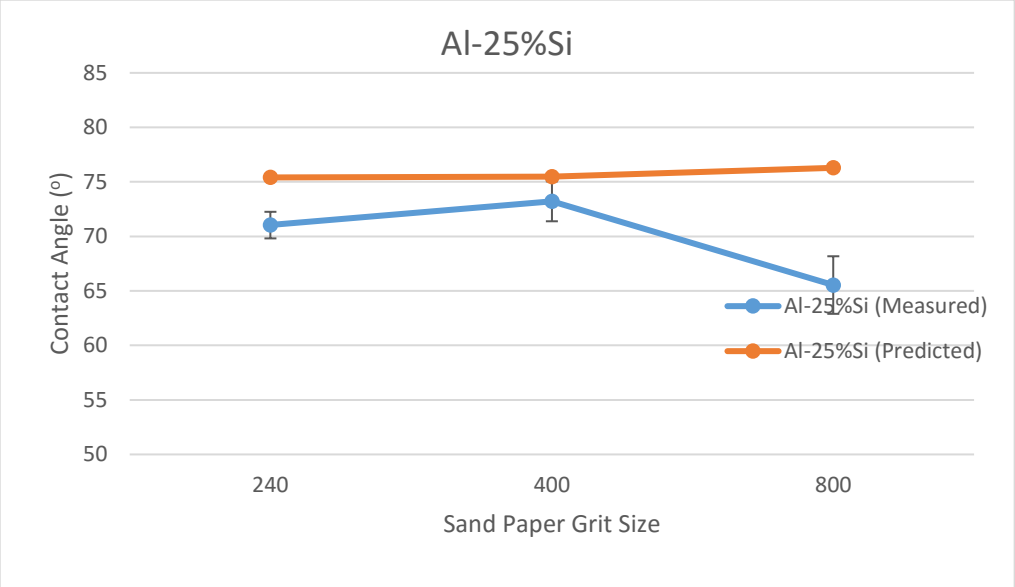

Figure 11: Comparison of experimental and Wenzel predicted contact angles for Al-25%Si

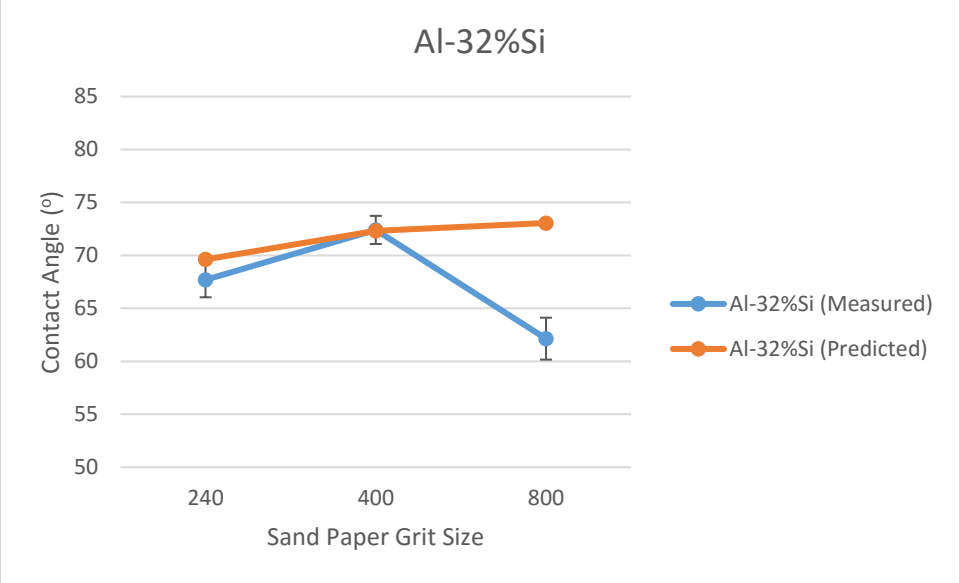

Figure 12: Comparison of experimental and Wenzel predicted contact angles for Al-32%Si

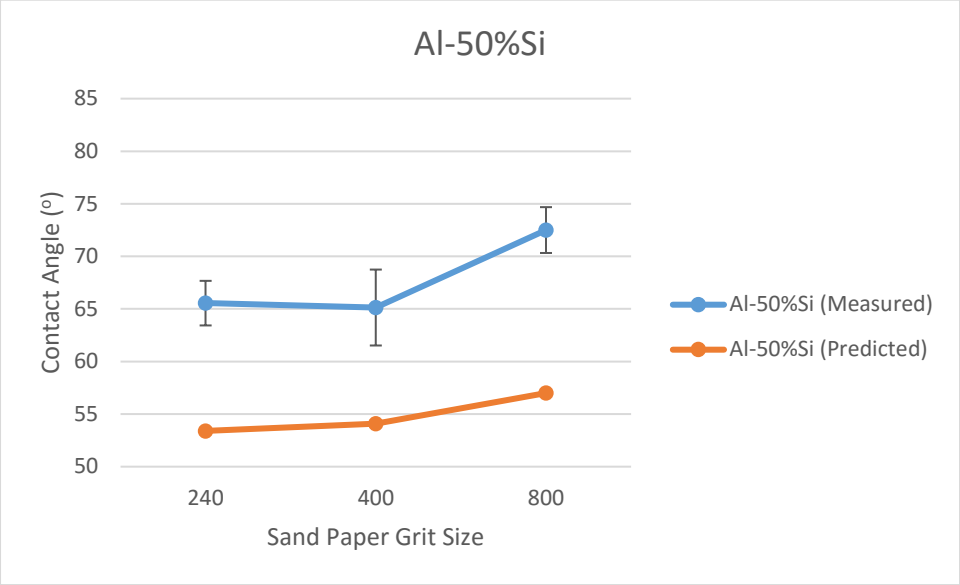

Figure 13: Comparison of experimental and Wenzel predicted contact angles for Al-50%Si

Figures 9-13 graphically show the variation of experimentally measured and theoretically predicted contact angles. For most of the alloy compositions (except 50%Si), the experimental contact angle tends to first increase and then decrease, while the theoretical contact angle stays almost constant. However, for 50%Si, the experimental contact angle tends to always increase.

Effect of composition and surface microstructure on the contact angle

To theoretically predict the contact angle for a composite interface such as that of Al-Si built of two fractions with fractional areas f_1 and f_2 such as α-Al and silicon phases, the contact angle can be predicted using following equation (15) [14]:

$$\cos\theta = f_1 \cos\theta_1 + f_2 \cos\theta_2 \qquad (11)$$

where θ_1 and θ_2 are the contact angles of the fractions, here smooth Al and Si, exposed to the ambient atmospheric conditions and polished to fully smooth surface finish, respectively.To predict the contact angle of the different Al-Si alloys using this equation, volume fractions of the two phases has been calculated using the rule of mixture.

Table 4: Volume % Si, Al, primary phase and eutectic phase theoretically predicted by lever rule

Sample	% Al	%Si	% Primary Phase	% Eutectic Phase
Al 356	93.0	7.0	51.14 Al	48.86
Al 368	91.0	9.0	32.88 Al	67.12
Al 360	90.50	9.50	28.31 Al	71.69
Al-22% Si	78.0	22.0	10.76 Si	89.24
Al-24% Si	76.0	24.0	13.04 Si	86.96
Al-25% Si	75.0	25.0	14.19 Si	85.81
Al-32% Si	68.0	32.0	22.20 Si	77.80
Al-50% Si	50.0	50.0	42.79 Si	57.21

The contact angle of Al exposed to the ambient atmosphere has been reported to be 75.4 ^{o} and the contact angle of Si exposed to the ambient atmosphere has been reported to be 36^{o} at room temperature [22-23]. This shows that more Si should imply lower contact angle.

Table 5 shows measured and predicted contact angles (predicted by rule of mixtures).

Table 5: Comparison of Measured CA and CA predicted by rule of mixture model

Composition	**Measured CA**	**CA by rule of mixtures**
Al-22%Si	71.49	67.09
Al-24%Si	75.62	66.34
Al-25%Si	75.53	65.96
Al-32%Si	81.05	63.34
Al-50%Si	73.9	56.56

It can be seen from Table 5 that the predicted contact angle is in agreement with the experimental values for lower %Si. As %Si increases the difference between measured contact angle and predicted contact angle increases.

4.2 Experimental Results of Wetting Properties

4.2.1 CA & Si%

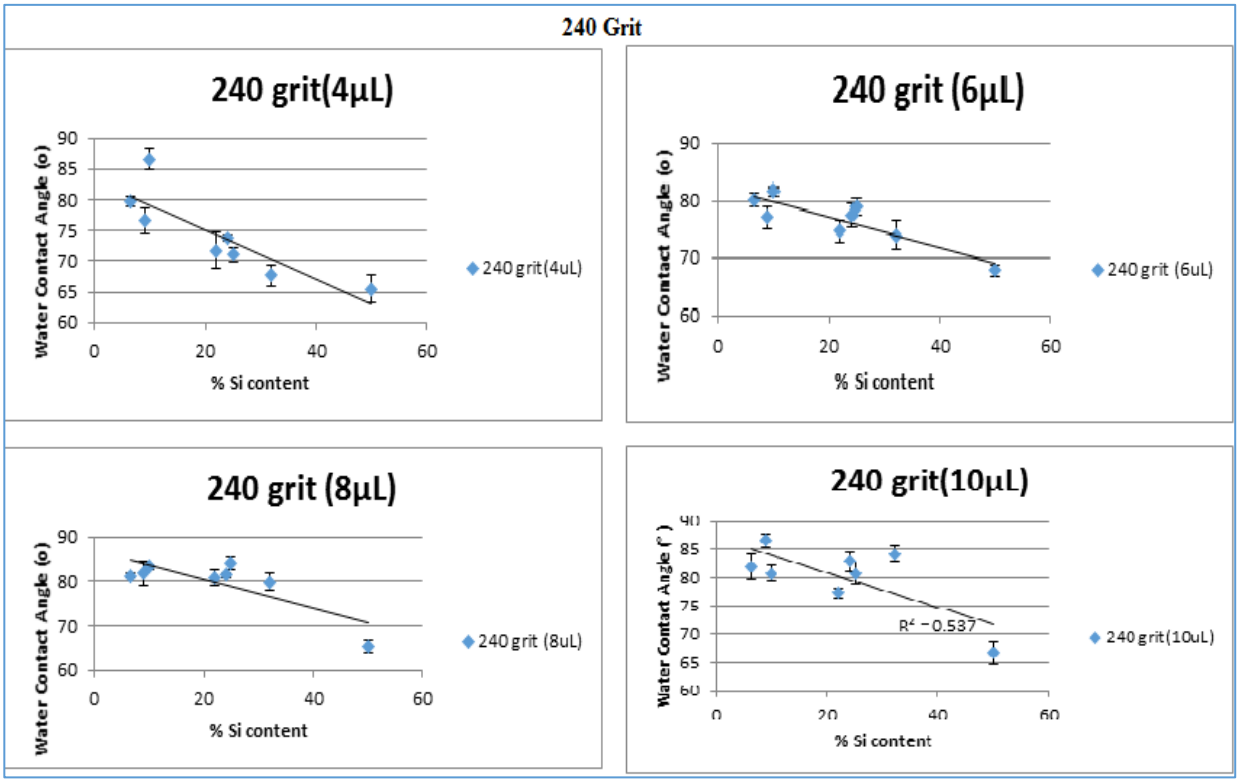

Figure 14: Effect of Silicon content on contact angle for 240 grit sand paper

We can clearly observe in Figure 14 that contact angle decreases with increasing Silicon content for droplet size of 4 µL. This is because the contact angle of Silicon is less than that of Aluminum. In other words, Silicon is more hydrophilic than Aluminum. Therefore, as the volume fraction of Silicon increases, the surface becomes more hydrophilic and thus the water contact angle decreases.

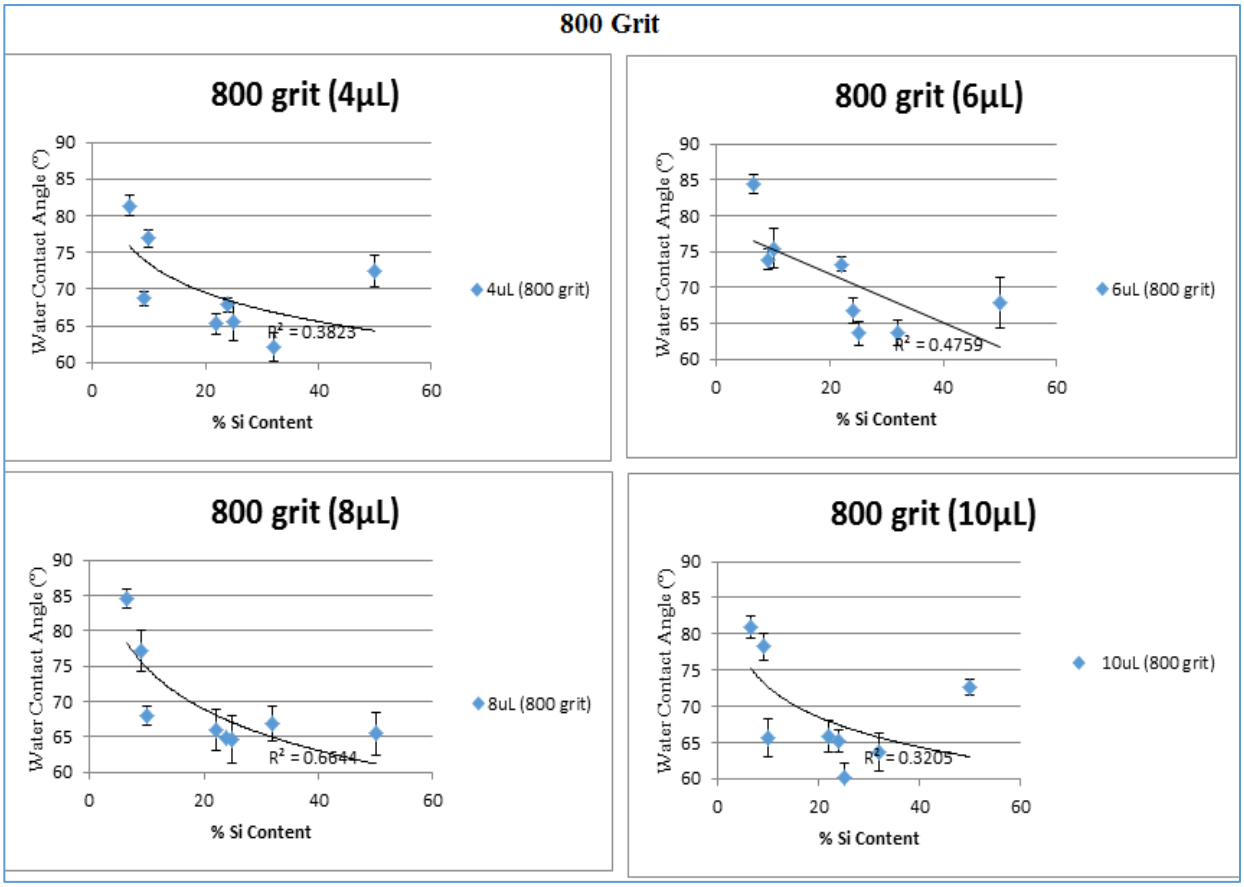

Figure 15: Variation of Contact Angle with Silicon content for samples polished with 800 grit size sand paper

In Figure 15 also we see that for samples polished with 800 grit size sand paper, contact angle decreases from nearly 80^o to about 65^o with change in silicon content from 7% to 50%. After reaching the eutectic composition, the contact angle either gradually decreases from about to 65^o to about 60^o or stays nearly constant. This may be explained by the fact that with increase in Si content, the hydrophilic component increases in volume fraction or surface area fraction because Silicon is more hydrophilic than Aluminum.

The variation for sample polished with 1200 grit size sand paper for 4 µL is a little different than for other droplet sizes in that it first decreases until 25% Si and then increases sharply for 32% Si. It starts from about 73^o for 22%Si and decreases to about 68^o for 25%Si. It then increases to about 82^o. For droplet size 6 µL the contact angle increases from 68^o to about 80^o. For 8 µL the

CA increases from about 72º to about 82º. For 10 µL the CA again varies from about 72º to about 82º.

4.2.2 Droplet size & CA

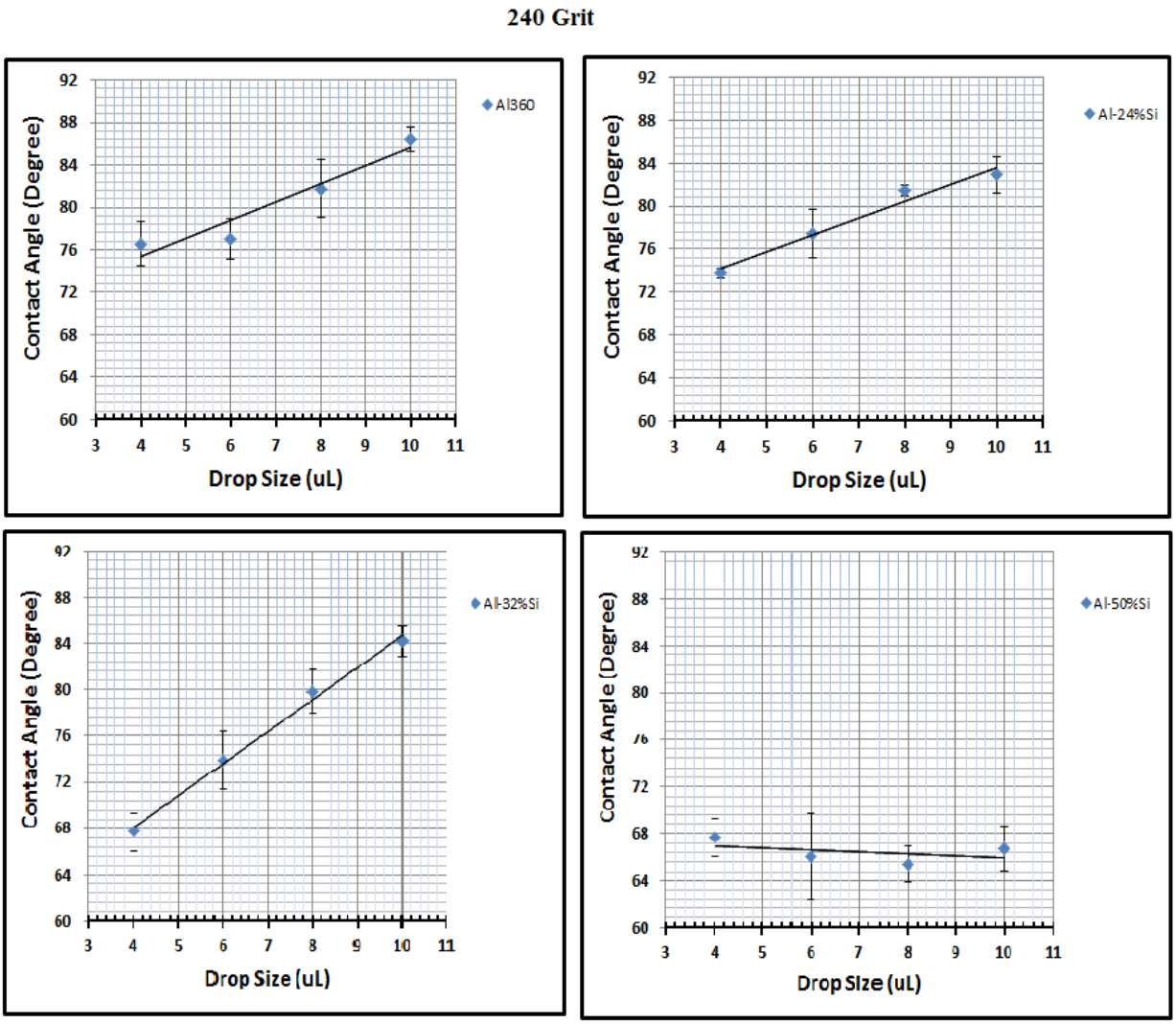

Figure 16: Contact angle v/s droplet size for samples polished with 240 grit size sand paper for Al-360, Al-24%Si, Al-32%Si and Al-50%Si

Figure 16 shows the effect of droplet size on contact angle. It can be seen that contact angle increases with increasing droplet size for Al-360, Al-24%Si and Al-32%Si. However, for Al-50%Si, the contact angle, either remains constant or decreases. When the droplet volume increases, influence of gravity becomes larger. Therefore, droplets larger than 10 microliter have not been used in this study. Influence of droplet size in microliter range has been studied in some

literature [21]. It has been studied that a larger contact angle hysteresis has greater impact of droplet volume on contact angle [21]. Contact angle hysteresis is caused by the substrate's deviation from the ideal surface such as chemical heterogeneity and surface roughness [21].

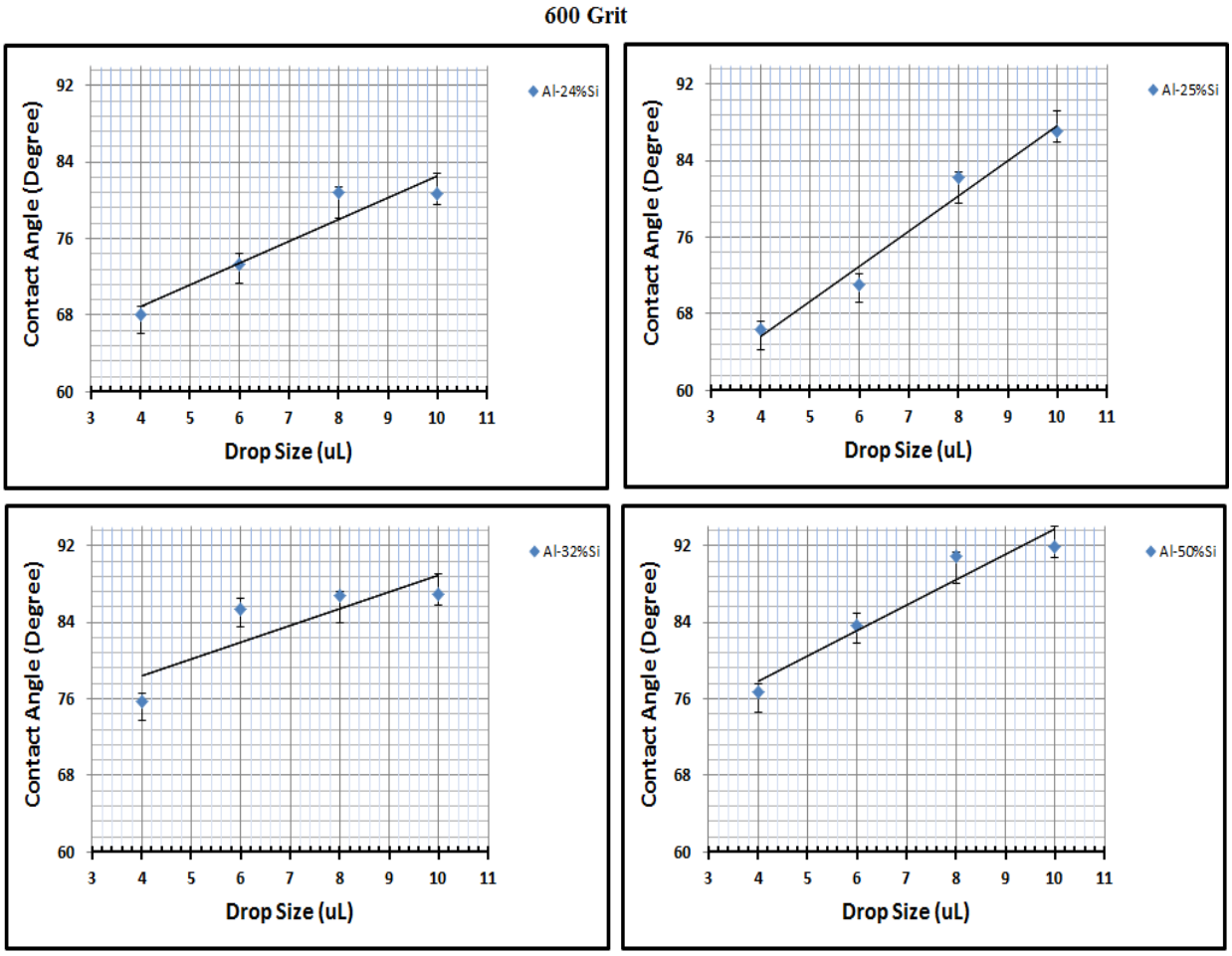

Figure 17: Contact angle v/s droplet size for samples polished with 600 grit size sand paper

Again, as shown in figure 17, for samples ground with 600 grit size sand paper as well, the contact angle increases almost linearly for most samples with different Silicon content.

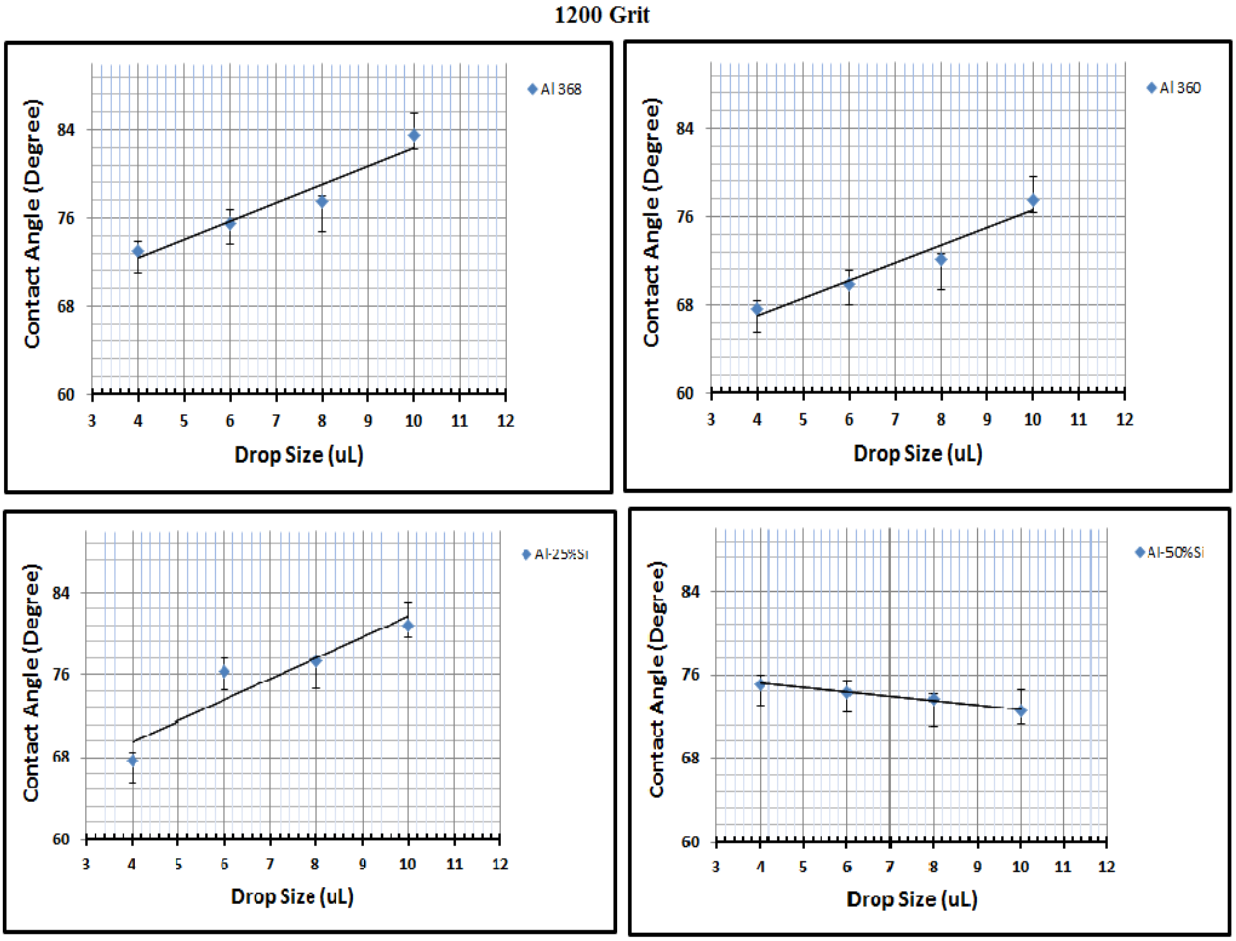

Figure 18: Variation of Contact angle with droplet size for samples ground with 1200 grit size sand paper

For samples polished with 240 grit size sand paper, it can be seen that contact angle increases nearly linearly with water droplet size. The only exception to this case is Al-356 which due to the presence of other elements interacts differently with water. For samples ground with 400 grit size sand paper as well, the contact angle increases almost linearly for most samples with different Silicon content.

4.2.3 CA & Sand Paper Grit Size

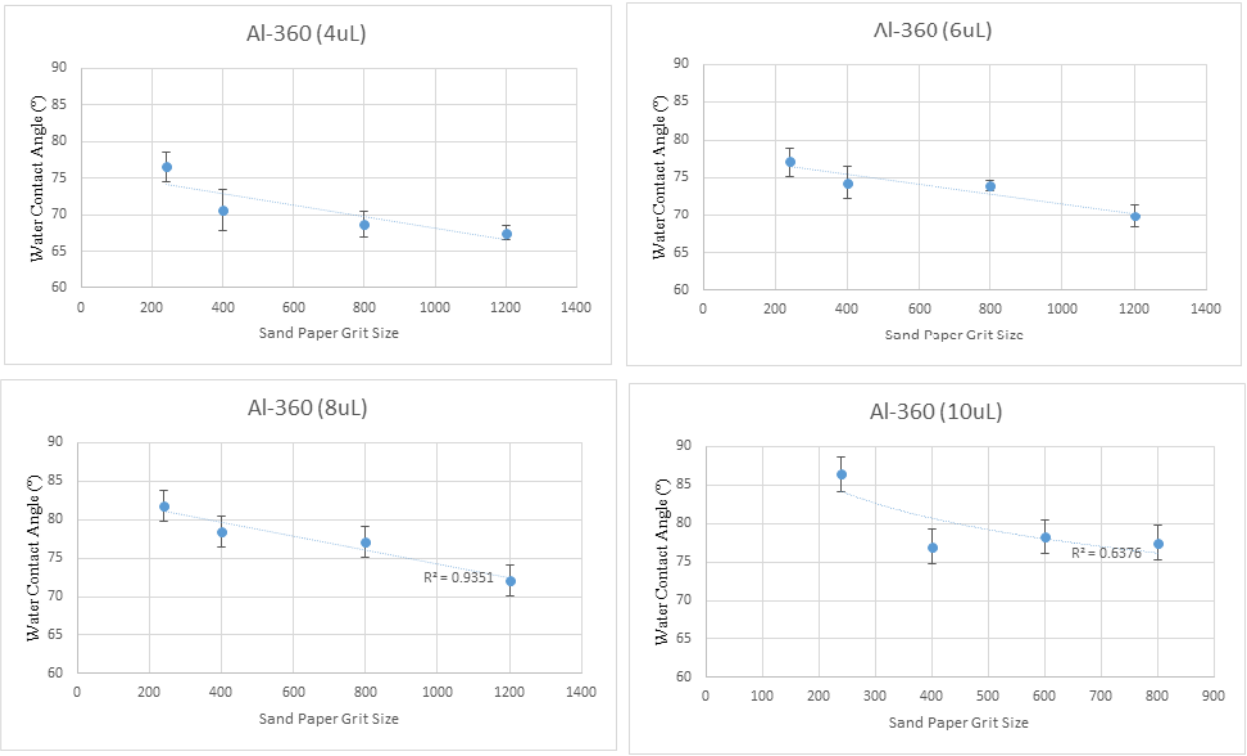

Figure 19: Variation of contact angle with sand paper grit size for Al-360

As shown in figure 19, contact angle constantly decreases with increasing sand paper grit number, as is expected, because with increasing grit number the roughness decreases and with decrease in roughness, the contact angle decreases. For Al-360 (4 μL) the contact angle decreases from 77^{o} to about 67^{o}. For Al-25%Si (4 μL) the contact angle decreases from about 73^{o} to about 64^{o}. For Al-360 (6 μL) the contact angle decreases from about 77^{o} to about 70^{o} for grit size varying from 240 to 1200.

For Al-368 (6 μL) the contact angle decreases from about 82^{o} to about 75^{o} for sand paper grit size varying from 240 to1200. For Al-22%Si (6 μL) the contact angle decreases from about 76^{o} to about 69^{o} for sand paper grit size varying from 240 to 1200. For Al-360 (8 μL) the contact angle decreases from about 82^{o} to about 72^{o} for sand paper grit size varying from 240 to 1200. For Al-360 (10 μL) the contact angle decreases from about 83^{o} to about 67^{o} for sand paper grit size varying from 240 to 1200.

Therefore, we see that contact angle decreases with increasing sand paper grit number as expected. This is because with increase in grit size the roughness of sand paper decreases. Therefore, for higher roughness the contact angle is higher and vice-versa

4.2.4 Contact angle & Roughness (R_a)

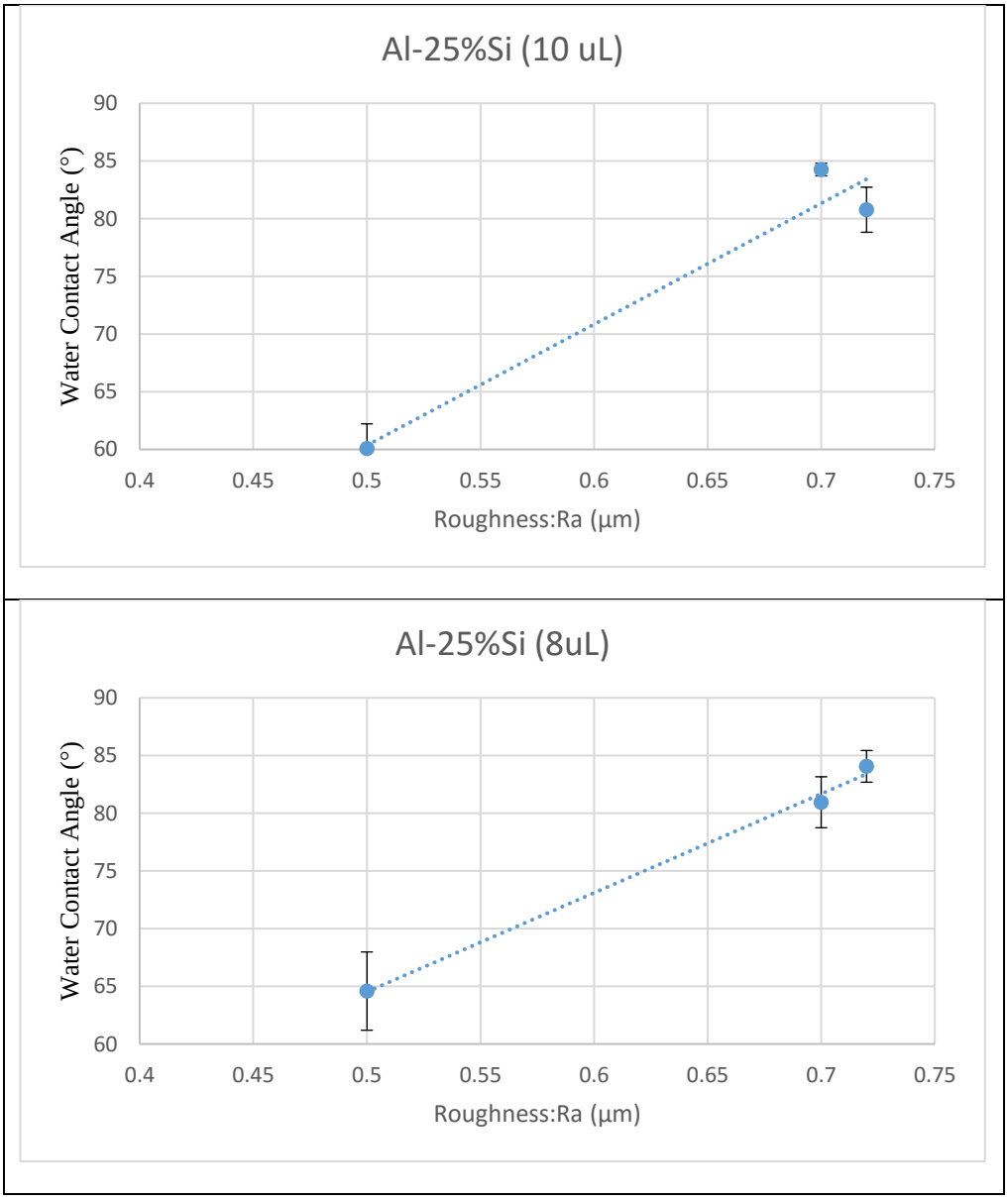

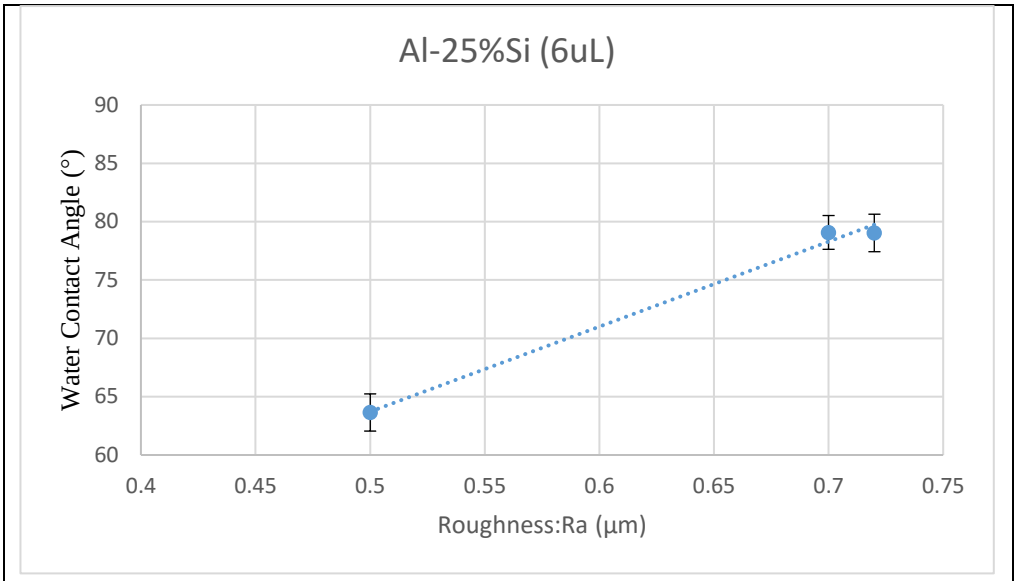
Al-25%Si (6uL)
Water Contact Angle (°)
90
85
80
75
70
65
60
0.4
0.45
0.5
0.55
0.6
0.65
0.7
0.75
Roughness:Ra (µm)

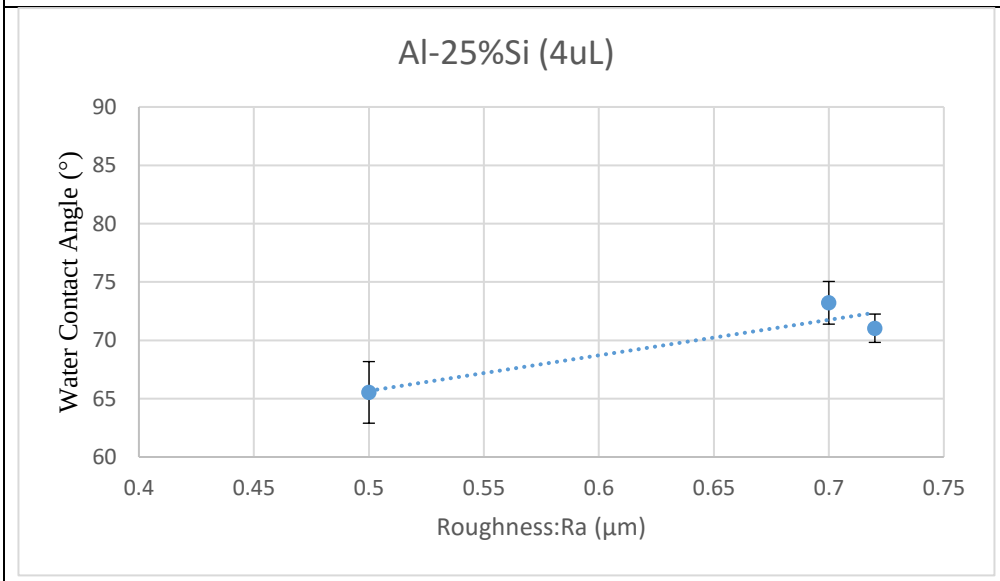
Al-25%Si (4uL)
Water Contact Angle (°)
90
85
80
75
70
65
60
0.4
0.45
0.5
0.55
0.6
0.65
0.7
0.75
Roughness:Ra (µm)

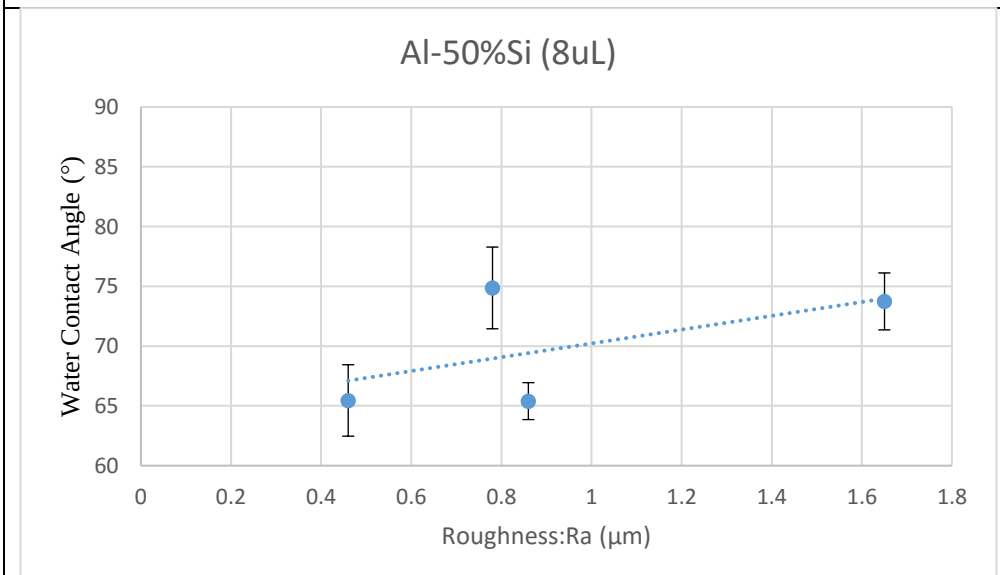
Al-50%Si (8uL)
Water Contact Angle (°)
90
85
80
75
70
65
60
0
0.2
0.4
0.6
0.8
1
1.2
1.4
1.6
1.8
Roughness:Ra (µm)

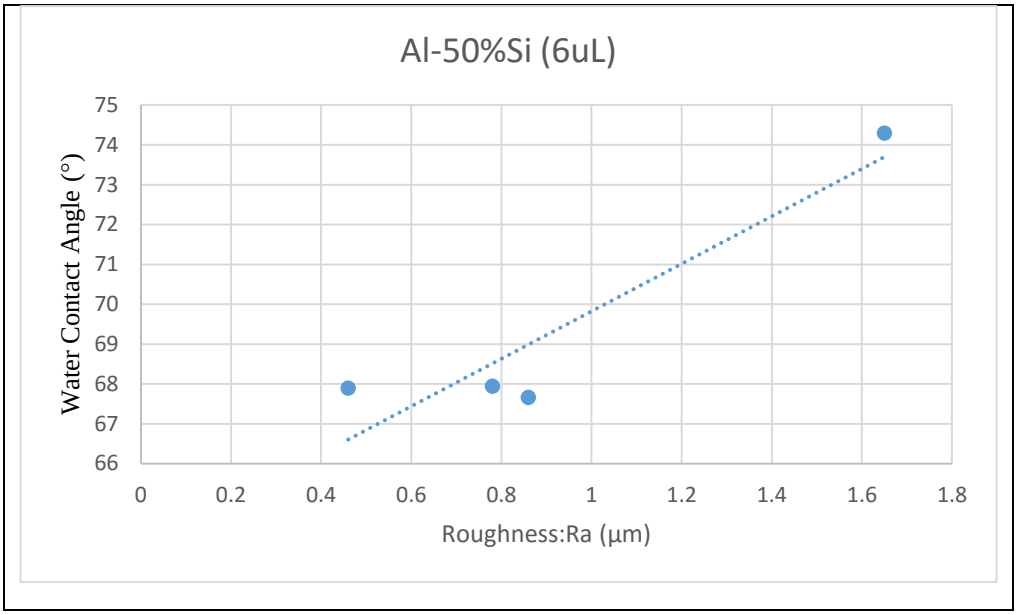

Figure 20: Variation of Contact angle with surface roughness value (R_a)

For the graphs shown in figure 20 on the previous pages, the contact angle increases with increasing value of R_a or surface roughness. For Al-360 the roughness value varies between about 0.33 μm to about 0.7 μm while the contact angle varies from about 73^o to about 86^o. For Al-25%Si sample the roughness value ranges from about 0.5 μm to about 0.72 μm whereas contact angle varies from 60^o to about 85^o for 10 μL, from 65^o to about 85^o for 8 μL, from about 62^o to about 80^o for 6 μL and from about 65^o to about 72^o for 4 μL droplet size. For Al-50%Si the contact angle varies from about 0.86 μm to about 2.5 μm. The contact angle varies from 65^o to about 75^o for 8 μL and from 65^o to about 80^o for 10 μL droplet size. It is worthwhile to note that roughness value does not only depend on sand paper grit size with which the sample is polished but also on composition or %Si content.

4.2.5 3-D Plots

Following section shows 3-dimensional plots plotted using Matlab to show the combined influence of two of the three parameters i.e. %Si content, sand paper grit number and water droplet size keeping the third parameter fixed.

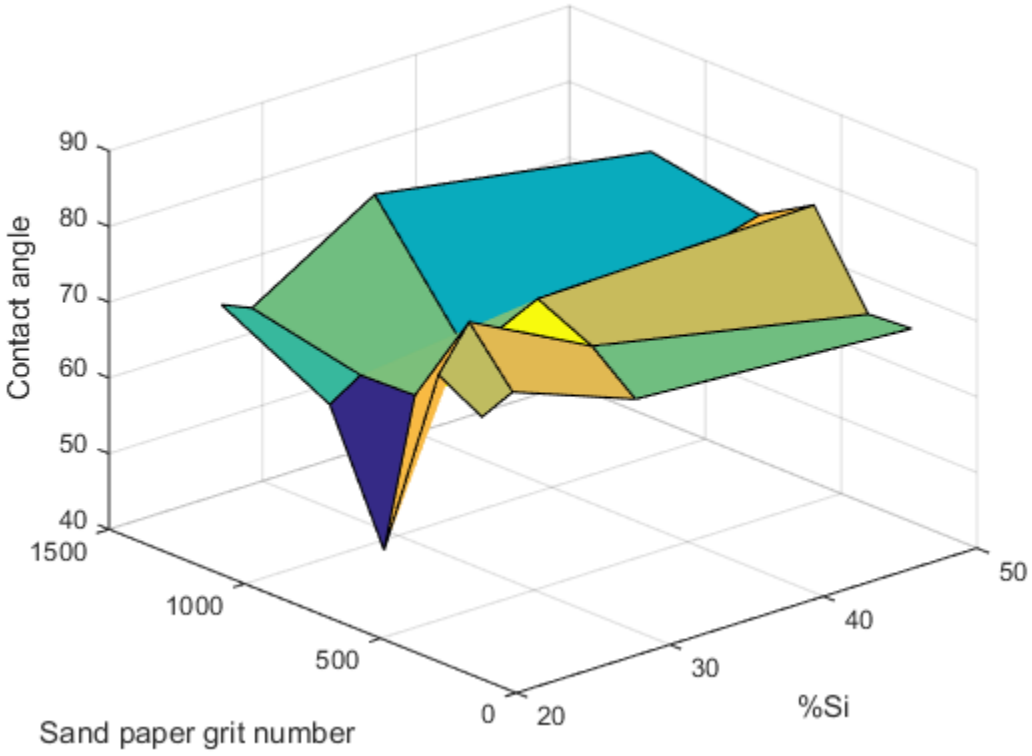

Figure 21: Contact angle versus sand paper grit number and %Si for droplet size 4 microliter

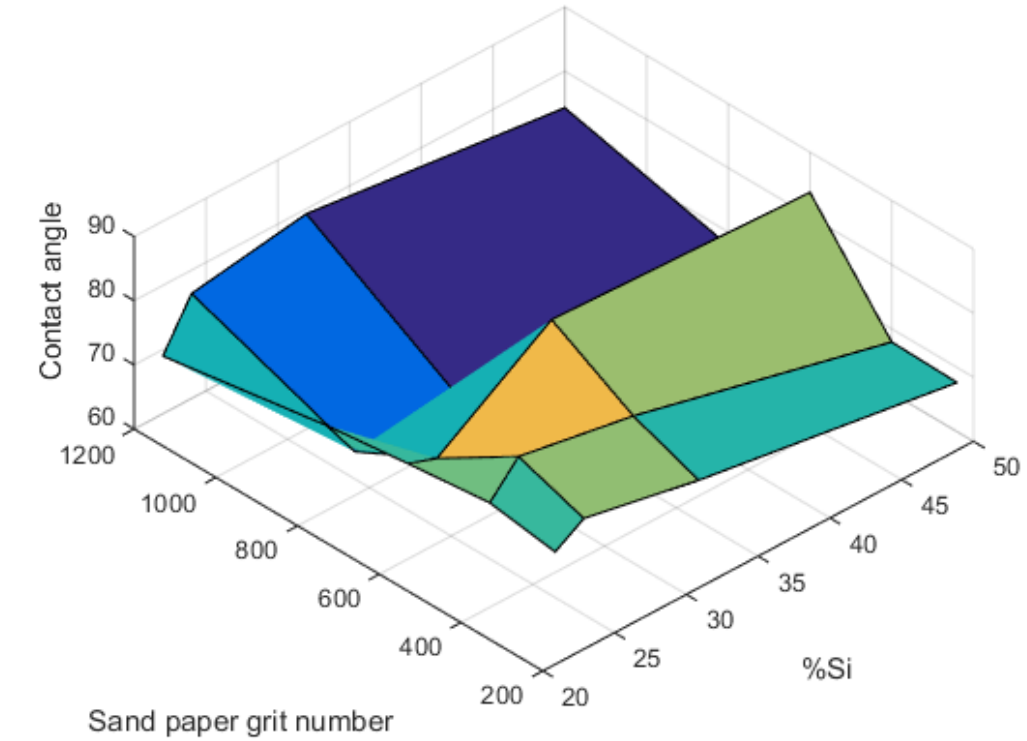

Figure 22: Contact angle versus sand paper grit number and %Si for droplet size 6 microliter

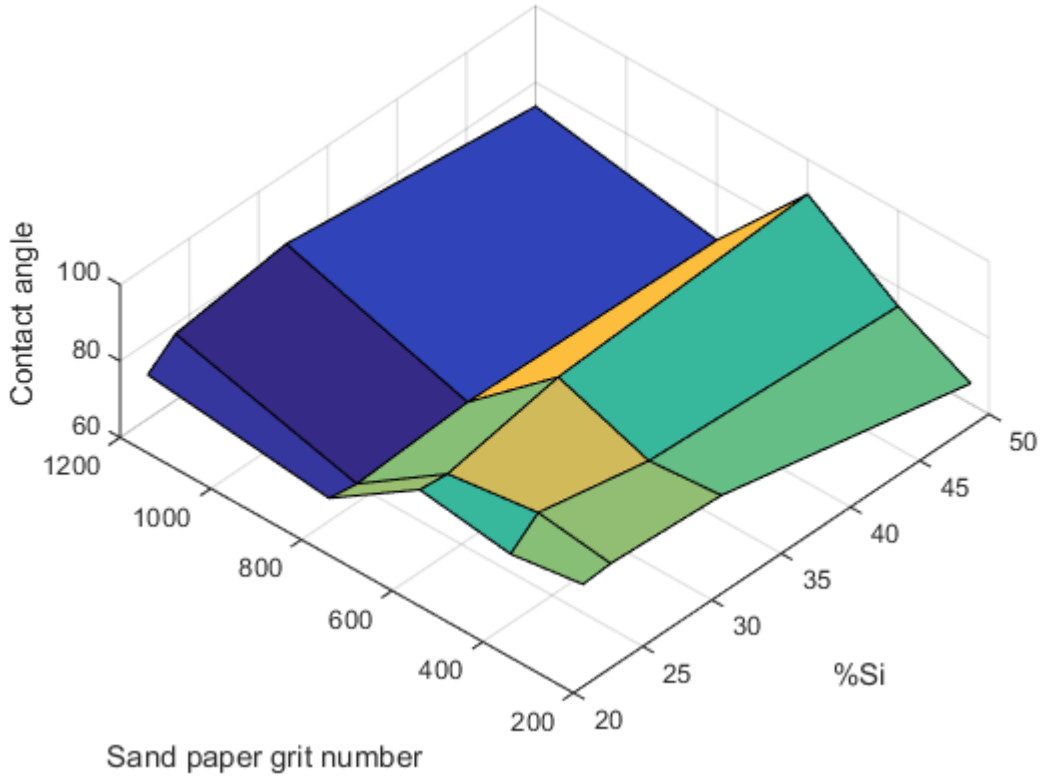

Figure 23: Contact angle versus sand paper grit number and %Si for droplet size 8 microliter

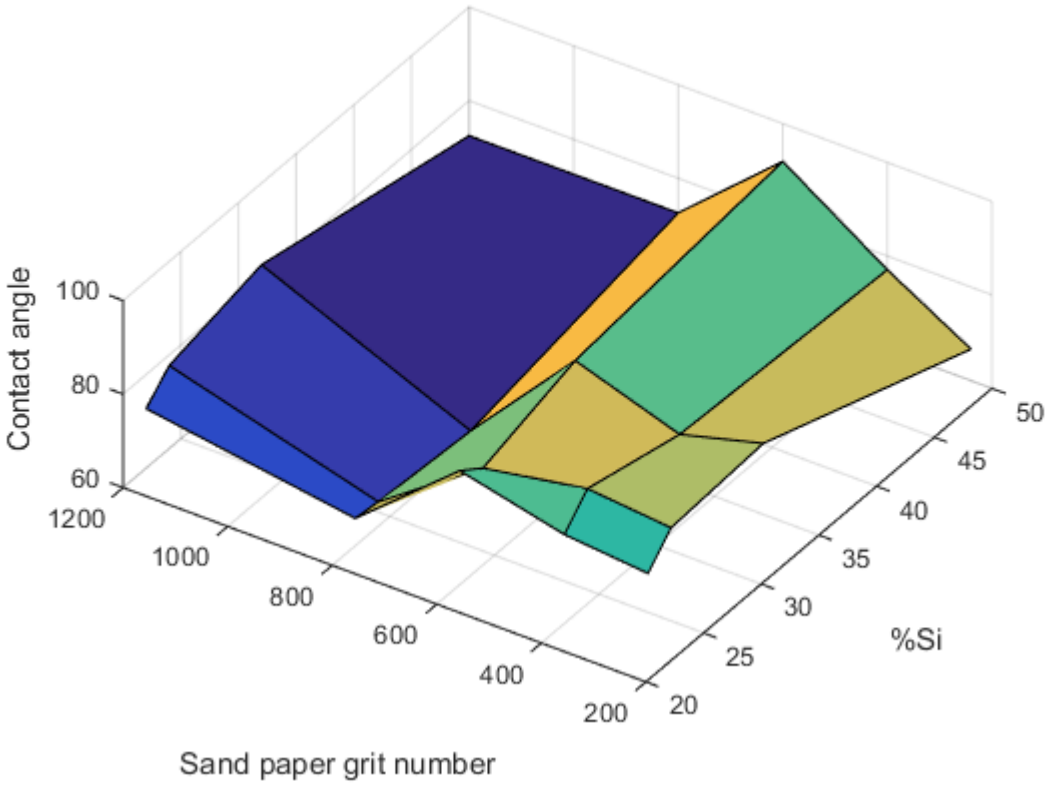

Figure 24: Contact angle versus sand paper grit number and %Si for droplet size 4 microliter

The 3-D plots showing the variation of contact angle with %Si and sand paper grit number shows that for droplet size 4 μL to 10 μL are shown in figures 21-24. The relationship of contact angle with sand paper grit number is not unique, however with %Si, it shows a well defined trend. The contact angle tends to decrease with increasing %Si content.

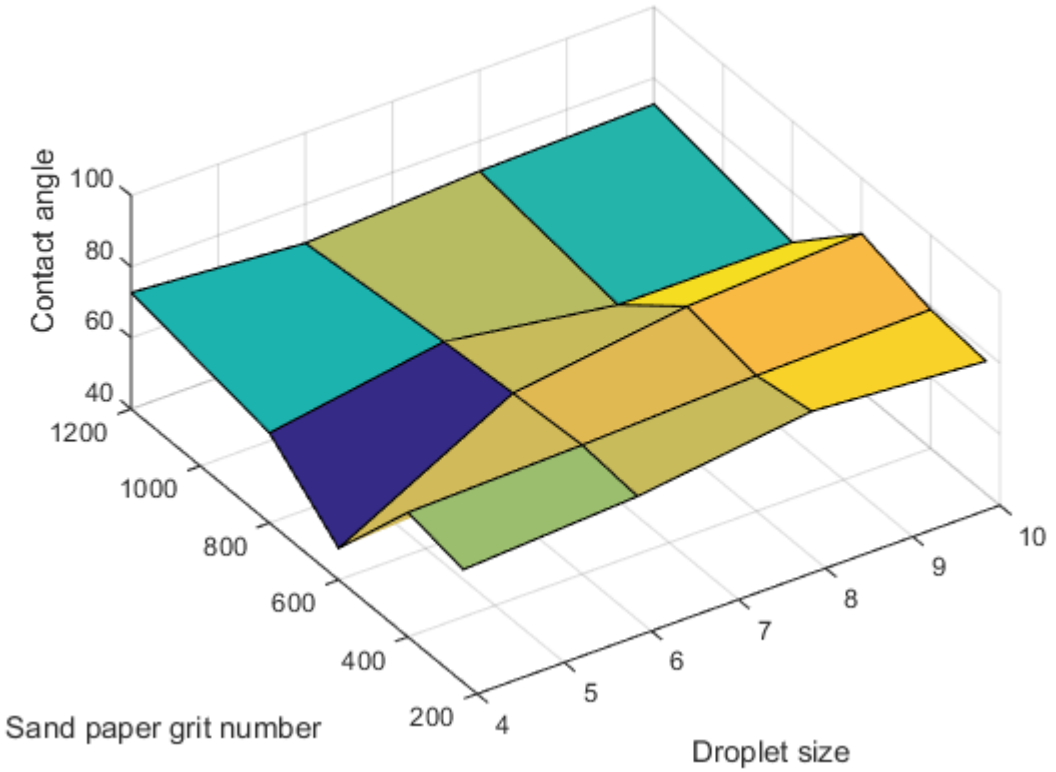

Figure 25: 3-D plot showing variation of contact angle with sand paper grit number and droplet size for Al-22%Si

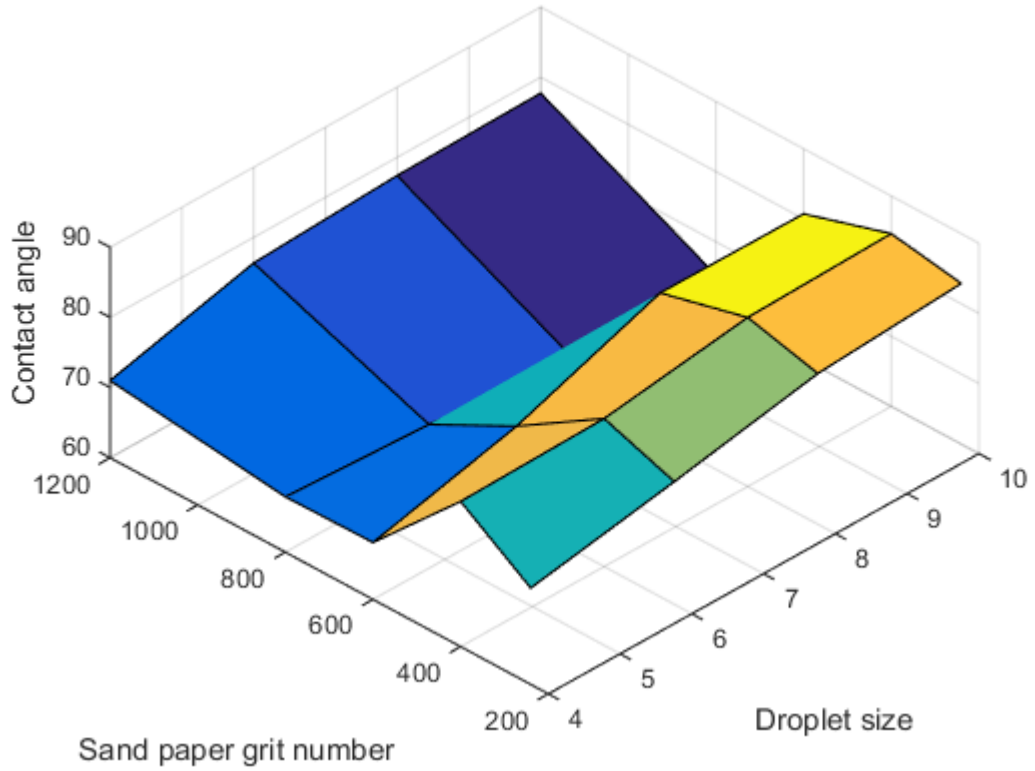

Figure 26: 3-D plot showing variation of contact angle with sand paper grit number and droplet size for Al-24%Si

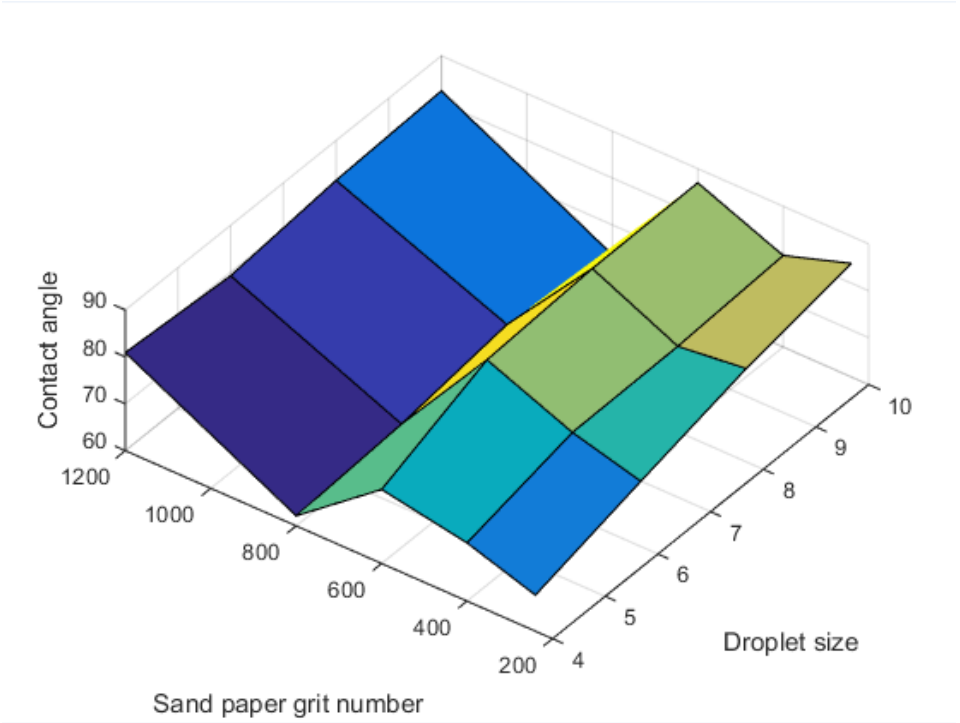

Figure 27: 3-D plot showing variation of contact angle with sand paper grit number and droplet size for Al-32%Si

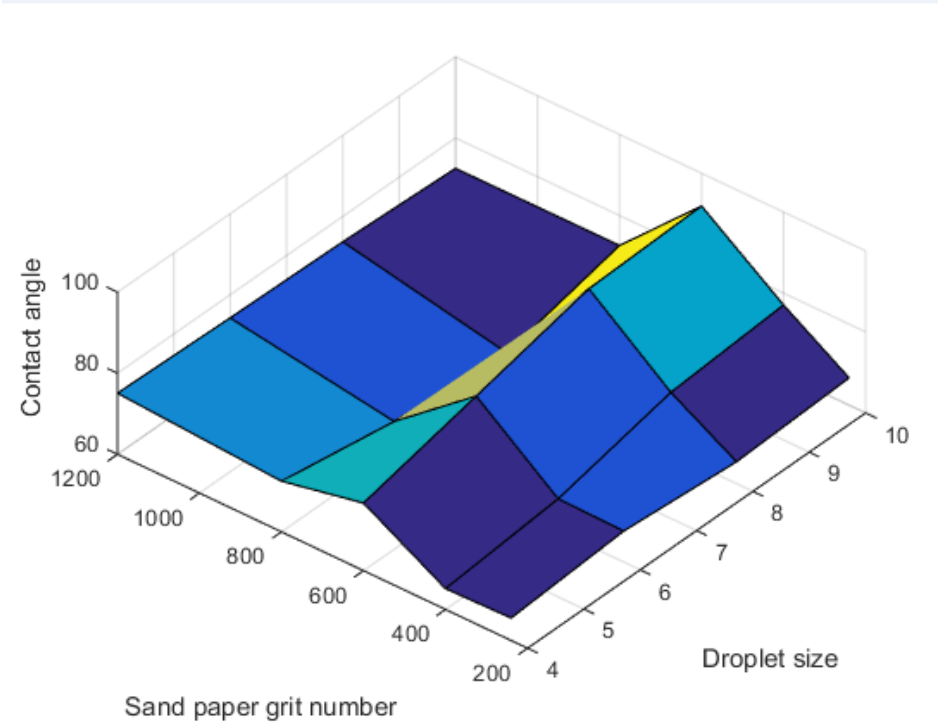

Figure 28: 3-D plot showing variation of contact angle with sand paper grit number and droplet size for Al-50%Si

The 3D plots of contact angle v/s sand paper grit number and droplet size for %Si varying from 22% to 50% are shown in figures 25-28. They also do not show a unique relationship between contact angle and sand paper grit number. However, the relationship between contact angle and droplet size seems to be well defined mostly and shows that CA increases with increasing droplet size.

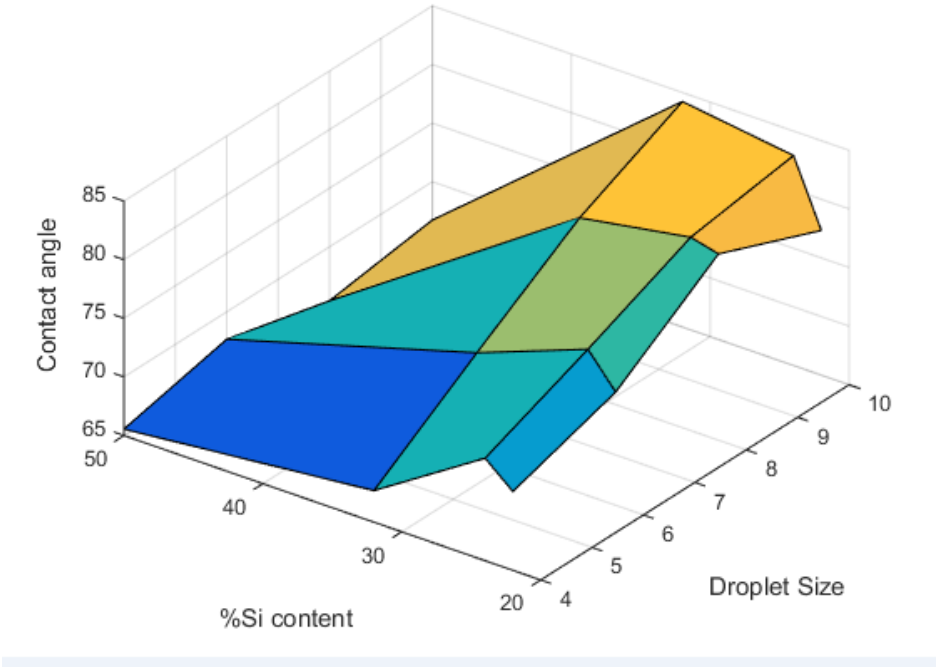

Figure 29: 3-D plot showing variation of contact angle with %Si content and droplet size for samples polished with 240 grit sand paper

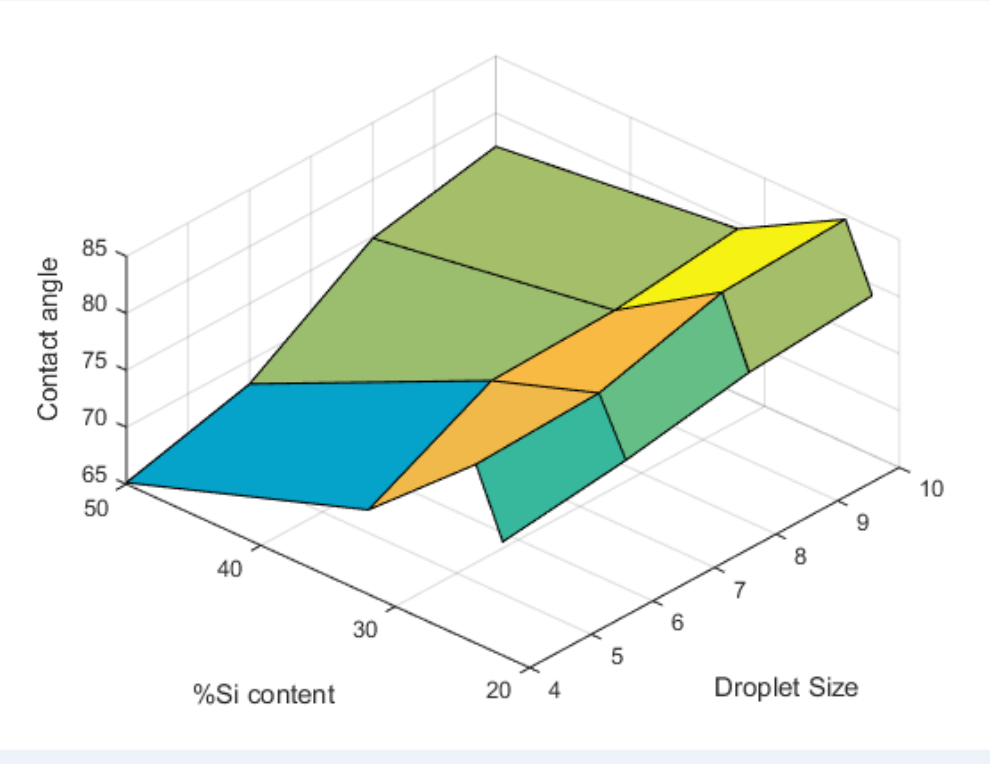

Figure 30: 3-D plot showing variation of contact angle with %Si content and droplet size for samples polished with 400 grit sand paper

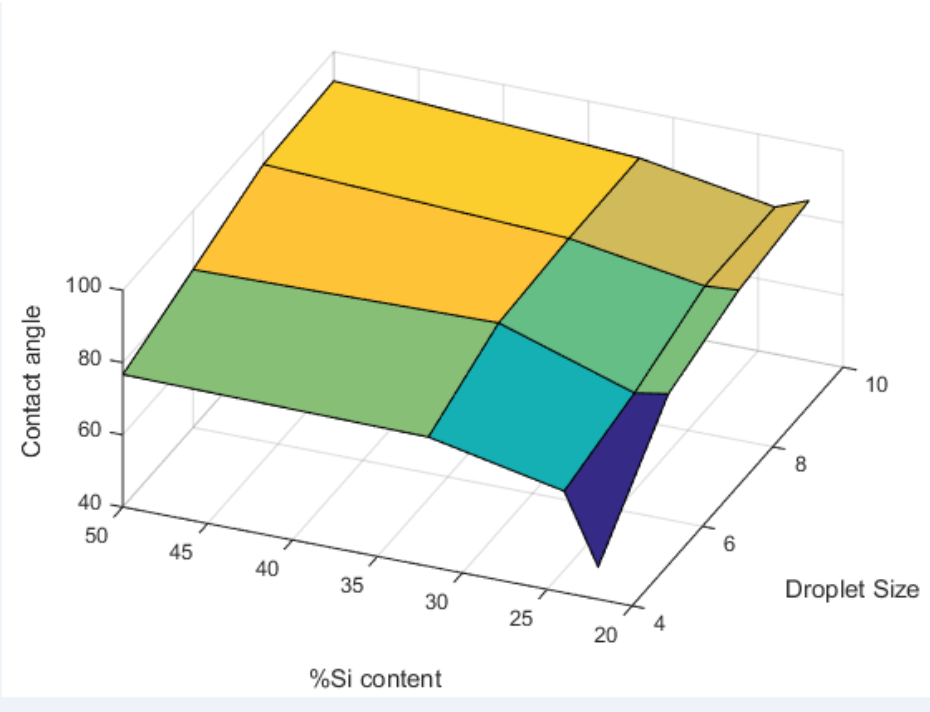

Figure 31: 3-D plot showing variation of contact angle with %Si content and droplet size for samples polished with 600 grit sand paper

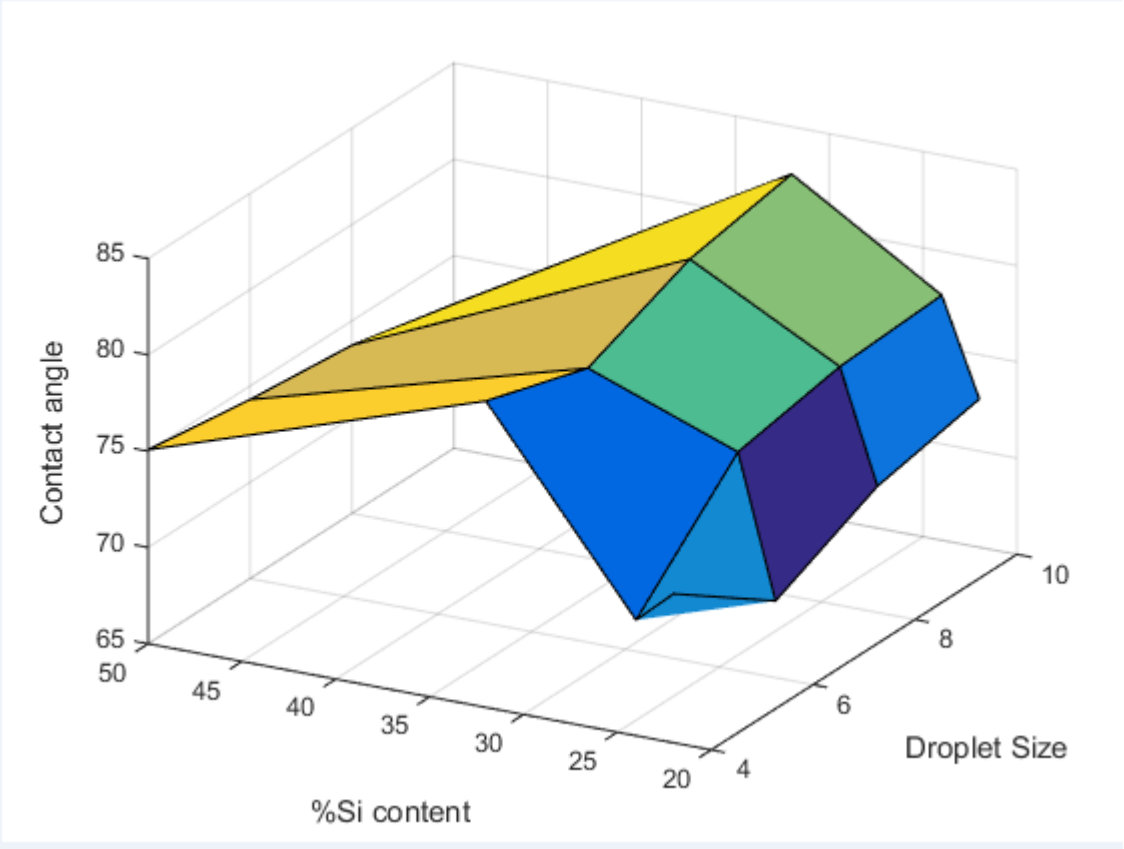

Figure 32: 3-D plot showing variation of contact angle with %Si content and droplet size for samples polished with 1200 grit sand paper

The 3D plots of contact angle v/s %Si content and droplet size are shown in figures 29-32 for sand paper grit sizes from 240 to 1200. These relations are pretty well defined, except for grit number 1200, such that with increasing %Si, the contact angle decreases, and increases with increasing droplet size.

4.3 Microstructure

The microstructure of all the Al-Si alloys used in this work has been studied. The microstructural constituents of the alloys such as size of primary silicon, size of interdendritic eutectic Al-Si and the spacing between eutectic Si have been observed and measured. A relationship between these quantities and the observed contact angle has been attempted to be studied. For referring to the different binary compositions and the phases present at that

composition for calculations by Lever rule, the binary phase diagram shown in figure 5 can be refered.

Table 6: Microstructural properties: Size of primary Si, spacing between eutectic, size of longest interdendritic observed for different alloy compositions for Al-Si (samples pre-polished with 800 grit sand paper)

Alloy	Size of Primary Si (μm)	Spacing between eutectic (μm)	Size of longest interdendritic eutectic (μm)
A356	NA	27.58	27.36
A360	NA	33.88	48.25
A368	NA	31.24	24.78
Al-22%Si	105.07	136.46	5.79
Al-25%Si	106.45	102.87	7.37
Al-32%Si	93.86	92.11	9.89
Al-50%Si	714.46	252.5	6.90

Typical resulting microstructures are shown from Fig.25-81 (appendix B). As shown in table 6 the size of primary Si in hypereutectic alloys increases with increasing weight % Si. Secondly the spacing between eutectic Al-Si also increases steeply going from hypoeutectic to hypereutectic. Lastly, the size of longest interdendritic Al-Si also decreases sharply going from hypoeutectic to hypereutectic. The size of longest interdendritic eutectic Al-Si also decreases with increasing weight % Si.

Table 7: Microstructural properties: Size of primary Si, spacing between eutectic, size of longest interdendritic observed for different alloy compositions for Al-Si (samples pre-polished with 240 grit sand paper)

Alloy	Size of Primary Si (μm)	Spacing between eutectic (μm)	Size of longest interdendritic eutectic (μm)
A356	NA	50.35	19.55
A368	NA	20.5	20.5
A360	NA	15.45	19.35
Al-22%Si	163.79	136.46	5.07
Al-25%Si	104.76	110.85	7.57
Al-32%Si	115	116.74	6.86
Al-50%Si	797.32	252.5	7.07

Table 7 also shows that the size of primary Si in hypereutectic alloys increases with increasing weight % Si. Secondly the spacing between eutectic Al-Si also increases steeply going from hypoeutectic to hypereutectic. Lastly, the size of longest interdendritic Al-Si also decreases sharply going from hypoeutectic to hypereutectic. The size of longest interdendritic eutectic Al-Si also decreases with increasing weight % Si.

4.4 Corrosion Properties

This section provides the results for variation of corrosion properties with alloy composition. All the Al-Si samples have been tested for corrosion to study the effect of composition on corrosion resistance. The procedure for corrosion test has been provided in section 3.5. Apart from the variation of corrosion properties with weight % Silicon, a study of the variation of properties with state of polish has also been done.

Table 8: Table of corrosion tests on selected abraded alloy samples

SAMPLE DESCRIPTION	SILICON %	STATE OF POLISH	E CORR	I CORR
Pure Aluminum	0%	Abraded	-923.483 mV	0.307 µA
Aluminum - Silicon (Al 356)	7 %	Abraded	-712.059 mV	0.126 µA
Aluminum - Silicon (Al 368)	9 %	Abraded	-835.193 mV	0.011 µA
Aluminum - 22% Silicon (Al-22 Si)	22 %	Abraded	-751.258 mV	0.015 µA
Aluminum - 24% Silicon (Al-24Si)	24 %	Abraded	-709.915 mV	0.106 µA
Aluminum - 25% Silicon (Al-25 Si)	25 %	Abraded	-703.011 mV	0.413 µA
Aluminum – 32% Silicon (Al-32 Si)	32 %	Abraded	-769.621 mV	0.041 µA
Aluminum – 32% Silicon (Al-32 Si)	32 %	Abraded	-710.959 mV	0.209 µA
Aluminum - 50% Silicon (Al-50 Si)	50 %	Abraded	-692.829 mV	0.493 µA

The table 9 shows that the I_{corr} does not show a systematic variation with weight % Si. However, it shows a relative minima in I_{corr} at Al-22%Si and thus a relative peak in corrosion resistance. The corresponding Tafel plots can be found in appendix C (figures 82-89).

It is known, from an electrochemical point of view, that Si possesses a nobler potential than Al, so that Al will be more susceptible to corrosion when immersed in some corrosive environment. Consequentially, as expected, the corrosion resistance should increase with increasing Si content as well as increasing secondary dendrite arm spacing would provide a better electrochemical corrosion behavior than a finer dendritic microstructure due to coarser micostructure. These trends, as recently reported, seem to be due to the different growth morphologies of the rough and faceted phases which make up the interdendritic eutectic mixture [23-26]. Figure 21 shows a relatively random variation of corrosion potential with weight fraction of silicon in abraded samples.

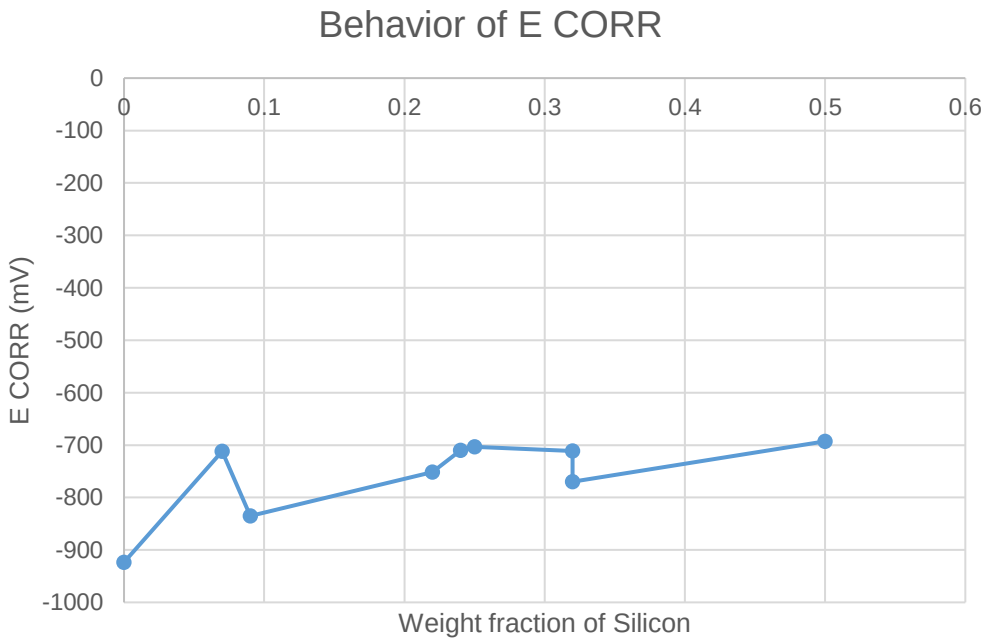

Figure 33: Variation of E_{corr} with weight fraction of Silicon for samples abraded with 400 grit sand paper

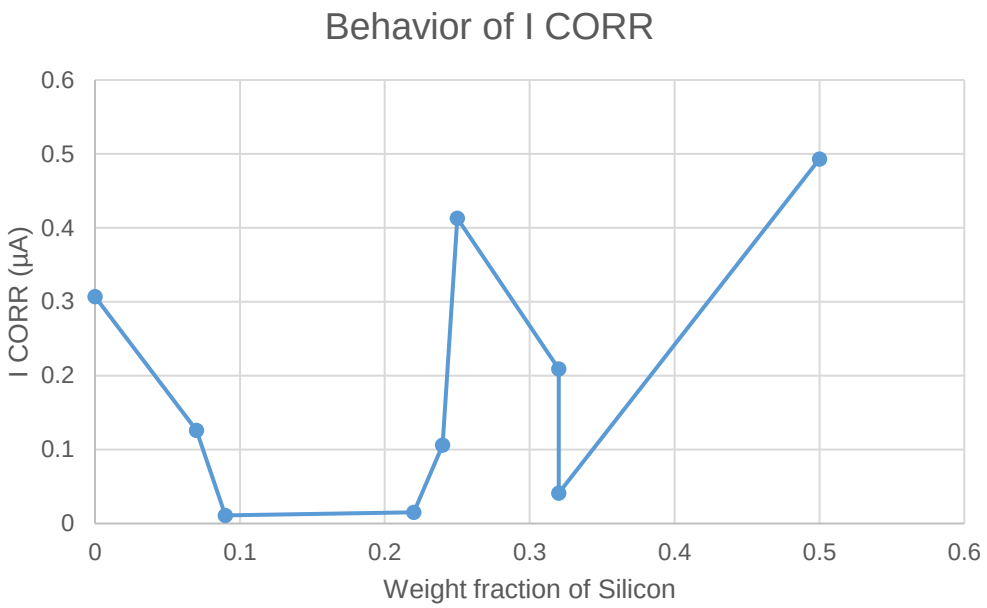

Figure 34: Variation of I_{corr} with weight fraction of Si for abraded samples

The increase in silicon content does not appear to have a systematic effect on the corrosion potential as shown in figure 33 and thus on the corrosion resistance. As shown in figure 34 the corrosion current I_{corr} also shows no systematic variation with weight fraction of silicon. However, a relative peak in corrosion resistance shown by a minima of I_{corr} is observed at 22% Si. It is observed in literature that the corrosion rate decreases with increasing distance from the metal/chill interface, thus microstructure affects the corrosion resistance as shown in a previous study [9].

Table 9: Table of corrosion tests on selected polished alloy samples

SAMPLE DESCRIPTION	SILICON %	STATE OF POLISH	E CORR	I CORR
Pure Aluminum	0%	Fully Polished	-722.123 mV	0.280 µA
Aluminum - Silicon (Al 356)	7 %	Fully Polished	-712.059 mV	0.126 µA
Aluminum - Silicon (Al 368)	9 %	Fully Polished	-711.576 mV	0.059 µA
Aluminum - 22% Silicon (Al-22 Si)	22 %	Fully Polished	-154.154 mV	0.005 µA
Aluminum - 24% Silicon (Al-24 Si)	24 %	Fully polished	-74.086 mV	1.111 µA
Aluminum - 25% Silicon (Al-25 Si)	25 %	Fully polished	-683.701 mV	0.946 µA
Aluminum - 25% Silicon (Al-25 Si)	25 %	Fully Polished	-710.469 mV	0.163 µA
Aluminum – 32% Silicon (Al-32 Si)	32 %	Fully Polished	-728.223 mV	0.110 µA

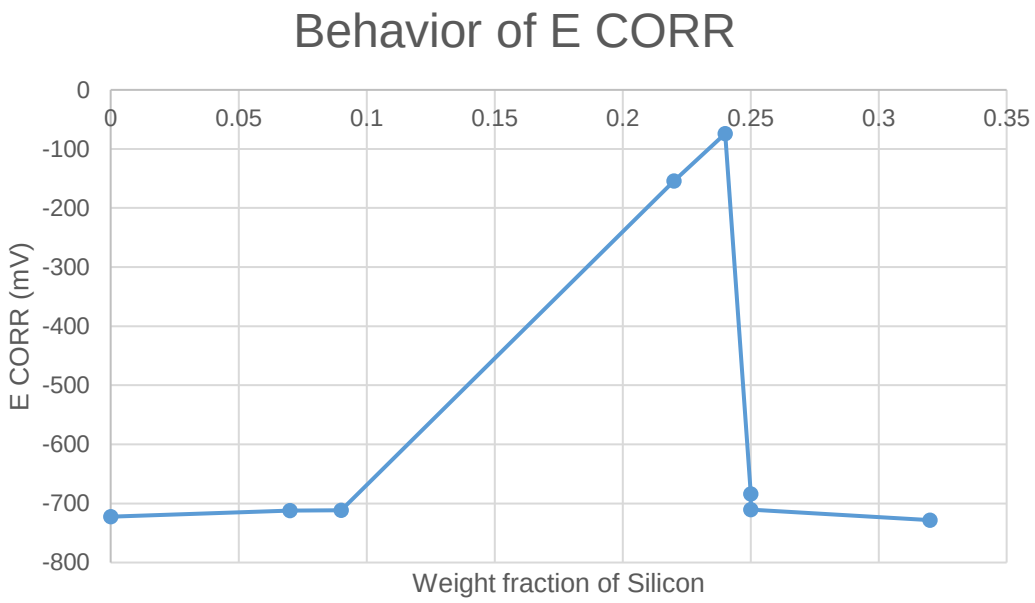

Figure 35: Variation of E_{corr} with weight fraction of Silicon for fully polished samples

Figure 23 shows a non-unique relationship between E_{corr} and weight fraction of silicon.

However, it shows a relative peak at Al-24% Si. The table 9 shows the results for fully polished

samples. It can been seen for most samples the corrosion resistance is higher for fully polished samples as compared to abraded samples as shown in table 11 below.

Table 10: Comparison of corrosion current for fully polished samples and abraded samples

SAMPLE DESCRIPTION	SILICON %	I CORR (Fully polished)	I CORR (Abraded)
Pure Aluminum	0%	0.280 µA	0.307 µA
Aluminum - Silicon (Al 356)	7%	0.126 µA	0.126 µA
Aluminum - 22% Silicon (Al-22 Si)	22%	0.005 µA	0.015 µA
Aluminum - 24% Silicon (Al-24 Si)	24%	0.106 µA	1.111 µA
Aluminum - 25% Silicon (Al-25 Si)	25%	0.163 µA	0.413 µA
Aluminum – 32% Silicon (Al-32 Si)	32%	0.110 µA	0.209 µA

The corresponding Tafel plots can be found in appendix C (figures 90-93). Figure 24 shows the variation of Icorr with weight fraction of Silicon. It shows a relative minimum, and therefore a maximum in corrosion resistance, at Al-22%Si.

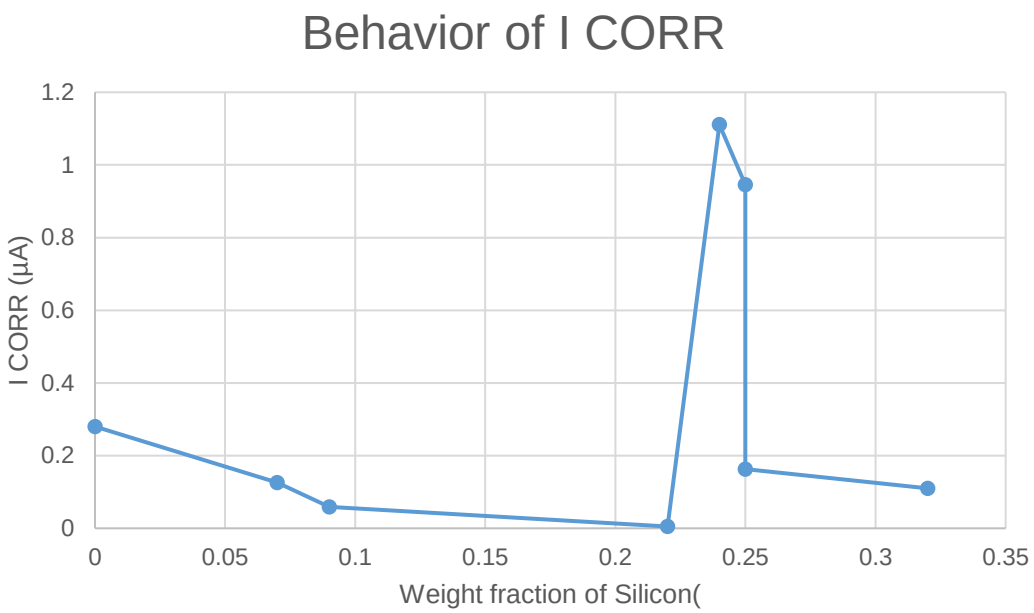

Figure 36: Variation of I_{corr} with weight fraction of Silicon for fully polished samples

5. Conclusions

The following conclusions discuss the trends observed in the variation of contact angle of Al-Si alloys with composition, surface roughness and water droplet size. The results of microstructural analysis have also been reported and the relationship between microstructural features and wettability have been reported. Lastly, the corrosion properties of different Al-Si alloys been measured as a function of the composition and state of polish.

1. As the volume percentage of primary Si increase the contact angle decreases. The water contact angle decreases from 90^o to 60^o as the weight % Silicon increases from 22% to 50% for a given degree of roughness and droplet size for samples roughened with 240 or 800 grit sand paper.
2. The water contact angle of all Al-Si alloys studied increases with increasing surface roughness.
3. In general, the contact angle increases with droplet size except for Al-50%Si.
4. No systematic variation in corrosion resistance was observed by increasing Si content from 0 to 50 % in abraded samples. A similar trend was observed for fully polished samples when %Si was varied between 0 to 32%. A peak in corrosion resistance was observed at 22%Si for abraded samples and 24%Si for fully polished samples. Lastly, the corrosion current is lower on polished samples in comparison to the abraded samples.

6. Future Work

For future work to be built on this work, the effect of droplet size on contact angle could be studied in more detail. The explanation regarding the increase in contact angle with droplet size needs to be investigated. Secondly, an explanation should be sought for the reason for Al-50%Si showing an opposite trend as compared to other compositions for the effect of droplet size on contact angle. Thirdly, the contact angle can be measured by changing the wait time between polishing and measurement of contact angle as well as changing the method used for removing droplets in between measurement of contact angle for different droplets. Further work needs to be done on study of effect of composition on corrosion behavior. More defined relation needs to be established between corrosion behavior and state of polish and silicon content.

References

1. J.R. Davies, Aluminium and aluminium alloys, ASM international, 1993.
2. F. Stadler, H. Antrekowitsch, W. Fragner, H. Kaufmann, E. Pinatel, P. Uggowitzer, Materials Science and Engineering: A, (2012).
3. J. Olofsson, I.L. Svensson, P. Lava, D. Debruyne, Materials & Design, 56 (2014) 755-762.
4. Simin Nickelsen, Afsaneh Dorri Moghadam, J.B. Ferguson, Pradeep Rohatgi, "Modeling and experimental study of oil/water contact angle on biomimetic micro-parallel-patterned self-cleaning surfaces of selected alloys used in water industry." Elsevier, Applied Surface Science 353 (2015) 781–787
5. R.N. Wenzel, Resistance of solid surfaces to wetting by water, Ind. Eng. Chem. 28 (1936) 988–994.
6. A.B. Cassie, S. Baxter, Wettability of porous surfaces, Trans. Faraday Soc. 40 (1944) 546–551.
7. L. Cao, T.P. Price, M. Weiss, D. Gao, Super water- and oil-repellent surfaces on intrinsically hydrophilic and oleophilic porous silicon films, Langmuir 24 (2008) 1640–1643.
8. R.T. Kumar, K.B. Mogensen, P. Bøggild, Simple approach to superamphiphobic overhanging silicon nanostructures, J. Phys. Chem. 114 (2010) 2936–2940.
9. H. Meng, S. Wang, J. Xi, Z. Tang, L. Jiang, Facile means of preparing superamphiphobic surfaces on common engineering metals, J. Phys. Chem. 112 (2008) 11454–11458.
10. A. Steele, I. Bayer, E. Loth, Inherently superoleophobic nanocomposite coatings by spray atomization, Nano Lett. 9 (2009) 501–505.
11. D. Han, A.J. Steckl, Superhydrophobic and oleophobic fibers by coaxial electrospinning, Langmui 25 (16) (2009) 9454–9462.
12. J.Y.Shiu,C.W.Kuo,P.Chen,C.Y.Mou, Fabrication of tunable superhydrophobic surfaces by nanosphere lithography, Chem. Mater. 16 (2004) 561–564.
13. Hejazi V., (2012). Wetting and Superhydrophobicity in Biomimetic Composite Materials, (Unpublished doctoral dissertation) University of Wisconsin, Milwaukee, USA
14. Nosonovsky, M.; Bhushan, B. Philos, Biomimetics inspired surfaces for drag reduction and oleophobicity/philicity. Trans. R. Soc. A 2009, 367, 1511–1539.
15. R. Fürstner, W. Barthlott, C. Neinhuis, P. Walzel, Wetting and self-cleaning properties of artificial superhydrophobic surfaces, Langmuir 21 (2005) 956–961.
16. S.R. Coulson, I.S. Woodward, J.P. Badyal, Ultralow surface energy plasma polymer films, Chem. Mater. 12 (2000) 2031–2038.
17. Y. Liu, Y. Xiu, D.W. Hess, C.P. Wong, Silicon surface structure-controlled oleophobicity, Langmuir 26 (2010) 8908–8913.
18. Qian, B.; Shen, Z., Fabrication of superhydrophobic surfaces by dislocation-selective chemical etching on aluminum, copper, and zinc substrates. Langmuir 21 (2005), 9007–9009.
19. Shirtcliffe, N. J.; McHale, G.; Newton, M. I.; Perry, C. C, Wetting and wetting transitions on copper-based super-hydrophobic surfaces, Langmuir 21(3). (2005); 937-43.
20. Sommers, A. D.; Jacobi, A. M. J. Micromech. Microeng. 2006, 16, 1571–1578

21. J. Drelich, "The Effect of Drop (Bubble) Size on Contact Angle at Solid Surfaces", J. Adhesion, 63, 31 (1997).

22. Mohammedreza Zamni, Al-Si Cast Alloys-Microstructure and Mechanical Properties at Ambient and Elevated Temperature, School of Engineering, Jonkoping University, Dissertation Series No.7, 2015.

23. R. Campos, A.J. Guenthner, A.J. Meuler, A. Tuteja, R.E. Cohen, G.H. McKinley, T.S. Haddad, J.M. Mabry, Superoleophobic surfaces through control of sprayed-on stochastic topography, Langmuir 28 (2012) 9834–9841.

24. L. Gao, J. McCarthy, How wenzel and cassie were wrong, Langmuir 23 (2007) 3762–3765.

25. C. Herring, Some theorems on the free energies of crystal surfaces, Phys. Rev. 82 (1951) 87–93.

26. T. Lu, Z. Guo, W. Li, Optimal design of superhydrophobic surfaces using a semicircular protrusion microtexture, RSC Adv. 5 (2015) 8446–8454.

27. W. Li, A. Amirfazli, A thermodynamic approach for determining the contact angle hysteresis for superhydrophobic surfaces, J. Colloid Interf. Sci. 292 (2005) 195–201.

28. G. McHale, Cassie and Wenzel:Were they really sp wrong? Langmuir 23 (2007) 8200–8205.

29. Wislei R. Osório, Pedro R. Goulart, Amauri Garcia, "Effect of silicon content on microstructure and electrochemical behavior of hypoeutectic Al–Si alloys" Materials Letters 62 (2008) 365–369.

30. Michael Nosonovsky, Vahid Hejazi, Aniedi E. Nyong, and Pradeep K. Rohatgi, "Metal Matrix Composites for Sustainable Lotus-Effect Surfaces" Langmuir 2011, 27, 14419–14424

31. Kietzig,A.M.;Hatzikiriakos,S.G.;Englezos,P.Langmuir2009, 25, 4821–4827.

32. Bormashenko, E.; Bormashenko, Y; Whyman, G.; Pogreb, R.; Stanevsky, O. J. Colloid Interface Sci. 2006, 302, 308–311.

33. Shirtcliffe, N. J.; McHale, G.; Newton, M. I.; Perry, C. C**,**Wetting and wetting transitions on copper-based super-hydrophobic surfaces Langmuir 2005, 21, 937–943.

34. Petrie, R. J.; Bailey, T.; Gorman, C. B.; Genzer, J. Langmuir 2004, 20, 9893–9896.

35. Vahid Hejazi, Afsaneh Dorri Moghadam, Pradeep Rohatgi, and Michael Nosonovsky**,** Beyond Wenzel and Cassie−Baxter: Second-Order Effects on the Wetting of Rough Surfaces, Langmui*r*, 2014, 30 (31), pp 9423–9429

36. Vahid Hejazi, Wetting and Superhydrophobicity in Biomimetic Composite Materials, Dissertation, University of Wisconsin-Milwaukee, February 2012.

37. X. Zhang, F. Shi, J. Niu, Y. Jiang, W. Zhiqiang, "Superhydrophobic surfaces: from structural control to functional application", *Journal of Material Chemistry*, vol. 18, pp 621-633, 2008.

38. Rame-hart. (2015). *Rame-hart Model 250, Standard Contact Angle Goniometer/ Tensiometer with DROPimage Advanced Software.* Succasunna, New Jersey: Rame-hart instruments co.

39. Robert J Good, M.N. Koo, “The effect of drop size on contact angle”, *Journal of Colloid and Interface Science,* vol.71, issue 2, pp 283-292, 1979.
40. Clemex Vision PE (2015). *The most complete image analysis solution Clemex Vision PE.* Longueuil, QC, Canada: Clemex Tenchologies Inc.
41. Bio-Logic SAS (2015). *SP-2xx/SP-300 Fast, sensitive, stable and modular, EC-LAB Products.* Knoxville, TN – USA: Bio-Logic USA, LLC.
42. Enke G. Christie, (2015, Deember 2). *The Analog Revolution and Its On-Going Role in Modern Analytical Measurements.* Retrieved from http://pubs.acs.org/doi/abs/10.1021/acs.analchem.5b02405?journalCode=ancham

Appendix A

Alloy: Al-22%Si Sand Paper Grit size: 240 Droplet Size: 4µL

Test 2	Test 3	Test 4
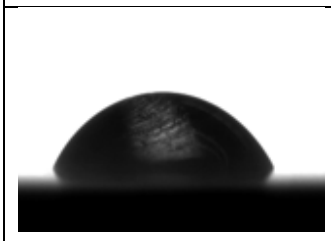		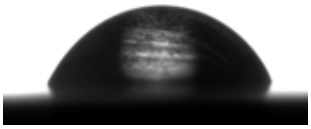
72.36	68.44	74.38

Alloy: Al-22%Si Sand Paper Grit size: 400 Droplet Size: 4µL

Test 1	Test 2	Test 4
		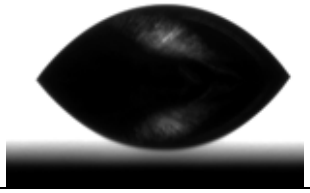
63.92	57.88	63.27

Alloy: Al-22%Si Sand Paper Grit size: 800 Droplet Size: 4µL

Test 1	Test 2	Test 3
		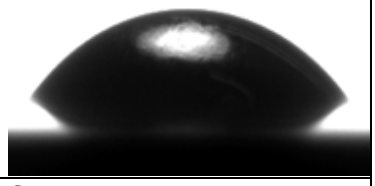
66.82	64.92	64.14

Alloy: Al-22%Si Sand Paper Grit size: 240 Droplet Size: 6µL

Test 1	Test 2	Test 3
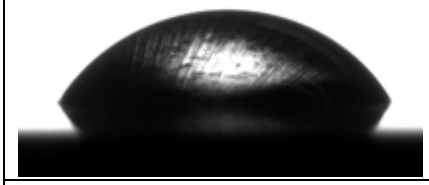	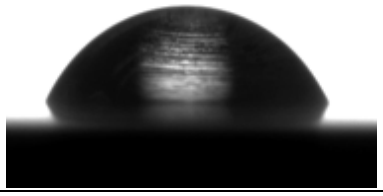	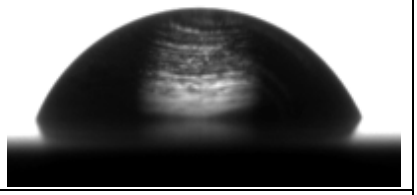
72.47	75.89	75.62

Alloy: Al-22%Si Sand Paper Grit size: 400 Droplet Size: 6µL

Test 1	Test 2	Test 3
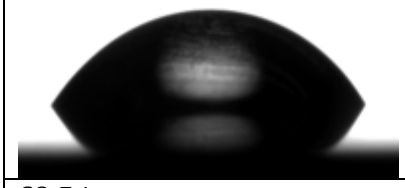	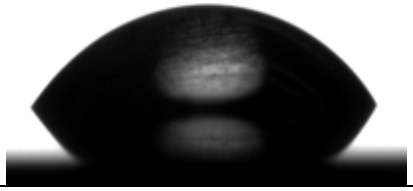	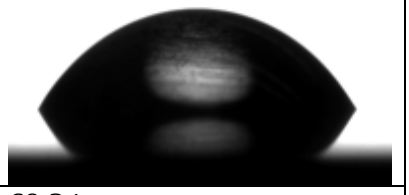
68.54	69.57	69.34

Alloy: Al-22%Si Sand Paper Grit size: 800 Droplet Size: 6µL

Test 2	Test 3	Test 4
	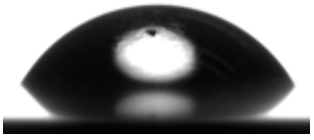	
66.98	72.79	72.65

Alloy: Al-22%Si Sand Paper Grit size: 240 Droplet Size: 8µL

Test 2	Test 3	Test 4
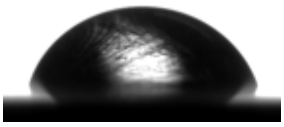	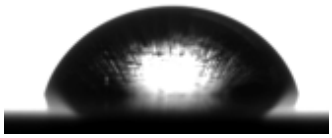	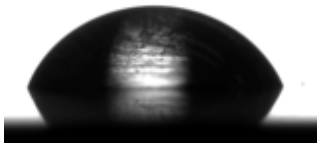
80.47	82.94	79.26

Alloy: Al-22%Si Sand Paper Grit size: 400 Droplet Size: 8μL

Test 1	Test 2	Test 3	Test 4
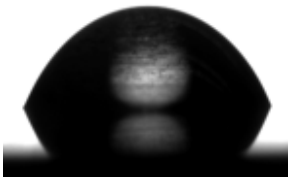	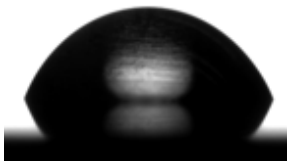	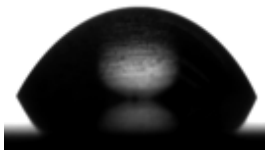	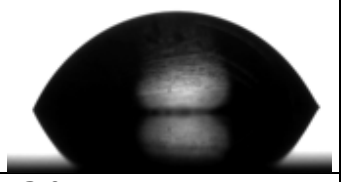
73.12	74.64	69.10	73.05

Alloy: Al-22%Si Sand Paper Grit size: 800 Droplet Size: 8μL

Test 2	Test 3	Test 4
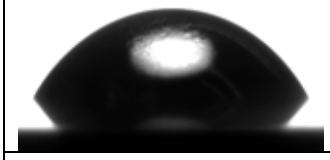	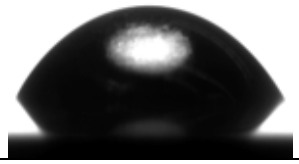	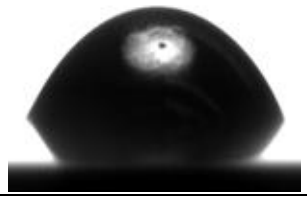
68.02	66.75	68.20

Alloy: Al-22%Si Sand Paper Grit size: 240 Droplet Size: 10μL

Test 1	Test 2	Test 3
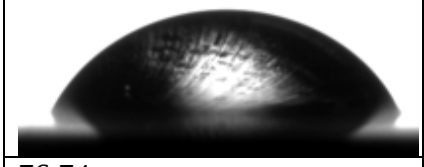	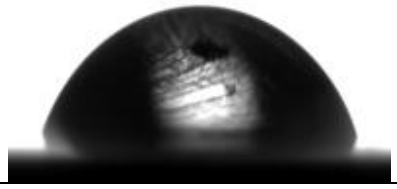	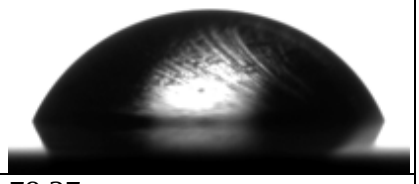
76.74	76.92	78.37

Alloy: Al-22%Si Sand Paper Grit size: 400 Droplet Size: 10μL

Test 1	Test 2	Test 3
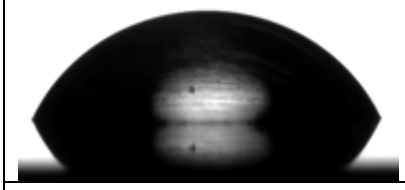	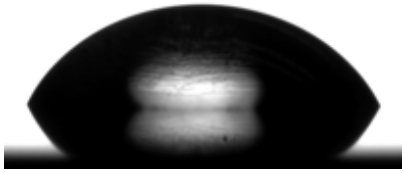	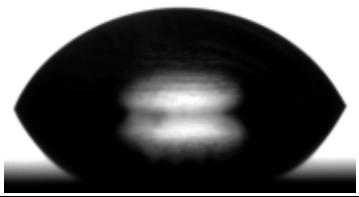
75.75	75.98	77.13

Alloy: Al-22%Si Sand Paper Grit size: 800 Droplet Size: 10μL

Test 1	Test 2	Test 3	Test 4
		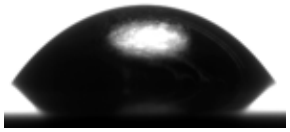	
67.45	66.36	62.70	66.94

Alloy: Al-24%Si Sand Paper Grit size: 240 Droplet Size: 4μL

Test 1	Test 2	Test 3
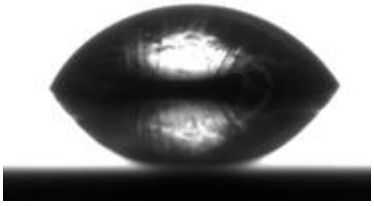	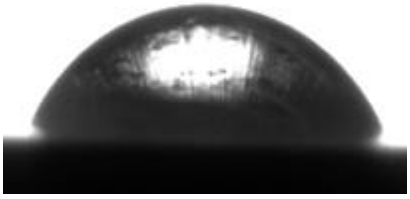	
73.98	74.05	73.20

Alloy: Al-24%Si Sand Paper Grit size: 400 Droplet Size: 4μL

Test 1	Test 2	Test 3
		
72.34	73.73	68.85

Alloy: Al-24%Si Sand Paper Grit size: 800 Droplet Size: 4μL

Test 1	Test 2	Test 4
		
67.04	67.66	69.00

Alloy: Al-24%Si Sand Paper Grit size: 240 Droplet Size: 6µL

Test 1	Test 2	Test 3
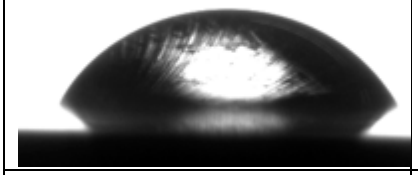	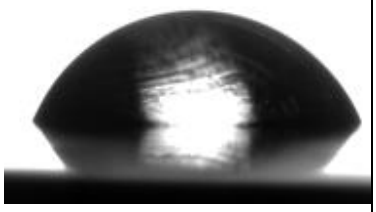	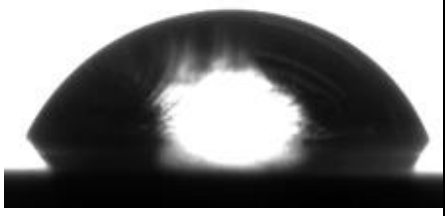
75.12	76.86	77.41

Alloy: Al-24%Si Sand Paper Grit size: 400 Droplet Size: 6µL

Test 1	Test 2	Test 3
		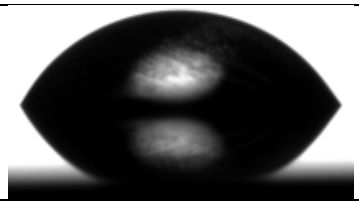
72.26	76.38	74.35

Alloy: Al-24%Si Sand Paper Grit size: 800 Droplet Size: 6µL

Test 1	Test 2	Test 3
		
66.08	64.94	66.97

Alloy: Al-24%Si Sand Paper Grit size: 240 Droplet Size: 8µL

Test 1	Test 2	Test 3
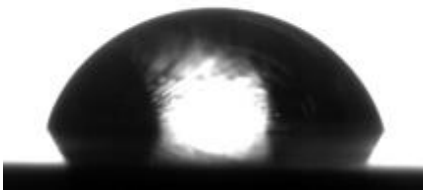	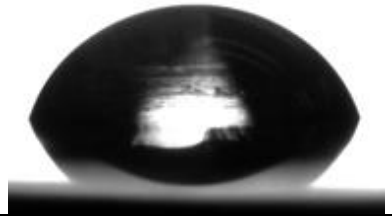	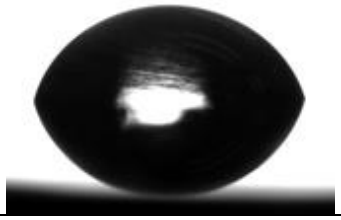
81.84	80.89	81.74

Alloy: Al-24%Si Sand Paper Grit size: 400 Droplet Size: 8µL

Test 1	Test 2	Test 3
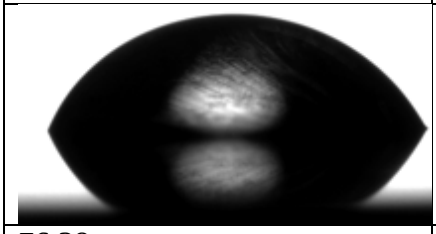	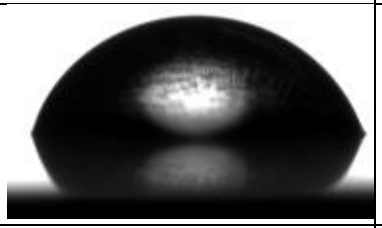	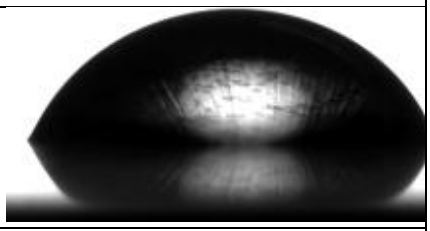
76.38	80.19	78.73

Alloy: Al-24%Si Sand Paper Grit size: 800 Droplet Size: 8µL

Test 1	Test 2	Test 3
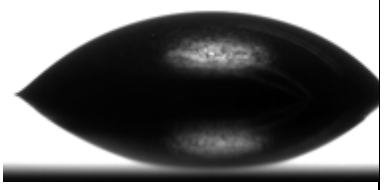		
64.94	65.15	64.56

Alloy: Al-24%Si Sand Paper Grit size: 240 Droplet Size: 10µL

Test 1	Test 2	Test 3
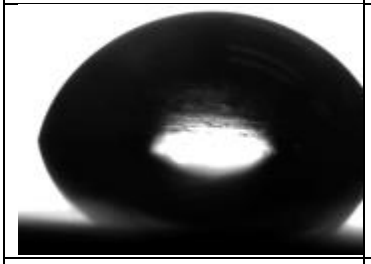	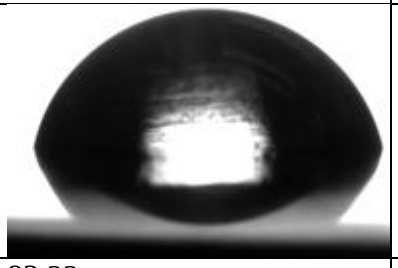	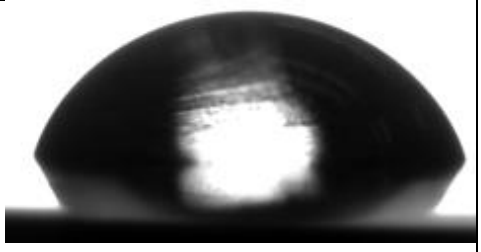
84.45	83.22	81.06

Alloy: Al-24%Si Sand Paper Grit size: 400 Droplet Size: 10µL

Test 1	Test 2	Test 3
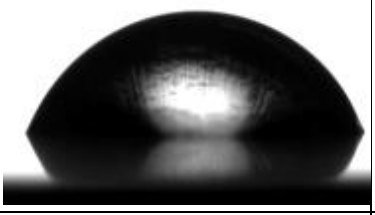	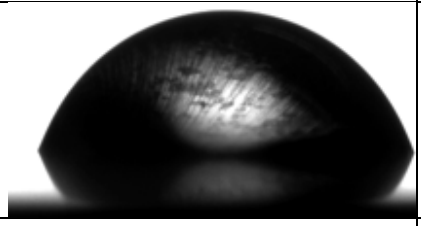	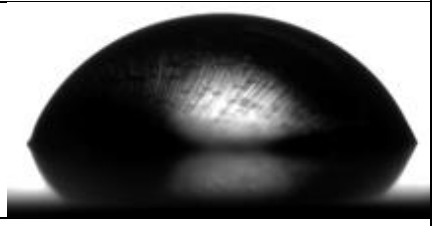
77.19	78.10	79.75

Alloy: Al-24%Si Sand Paper Grit size: 800 Droplet Size: 10μL

Test 1	Test 2	Test 3
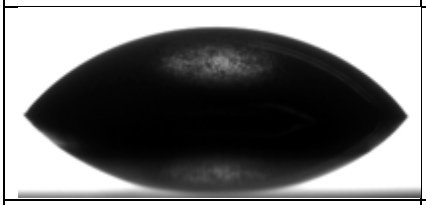		
66.22	65.62	66.21

Alloy: Al-25%Si Sand Paper Grit size: 240 Droplet Size: 4μL

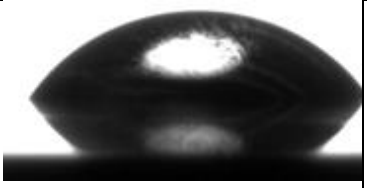	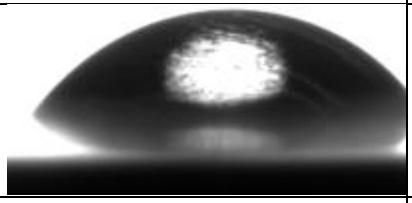	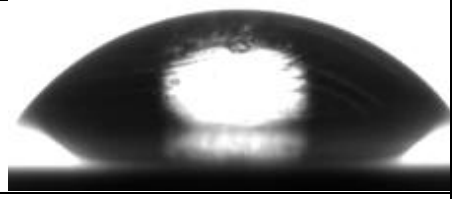
70.98	69.85	72.28

Alloy: Al-25%Si Sand Paper Grit size: 400 Droplet Size: 4μL

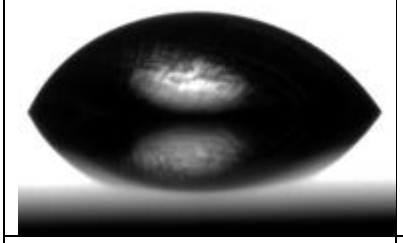	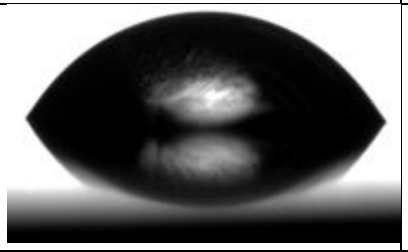	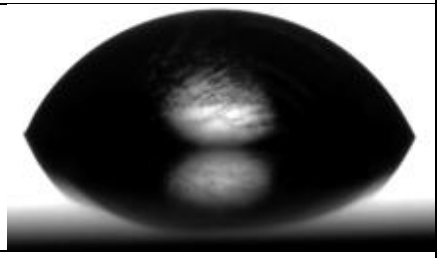
74.22	72.27	77.57

Alloy: Al-25%Si Sand Paper Grit size: 800 Droplet Size: 4μL

Test 1	Test 2	Test 3	Test 4
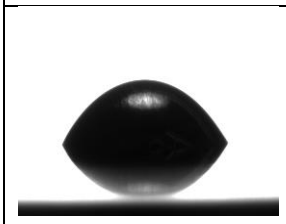	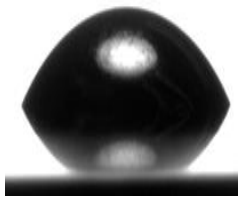	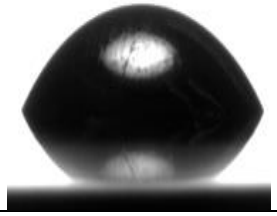	
61.58	66.76	66.86	66.95

Alloy: Al-25%Si Sand Paper Grit size: 240 Droplet Size: 6μL

Test1	Test 2	Test 3	Test 4
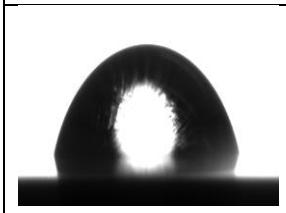	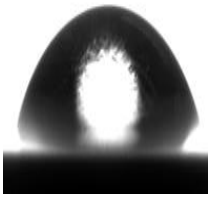	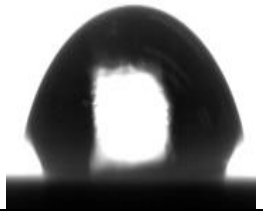	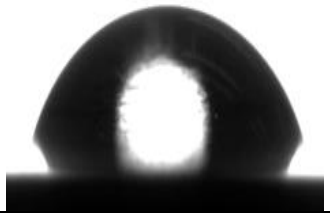
79.58	77.32	81.00	78.22

Alloy: Al-25%Si Sand Paper Grit size: 400 Droplet Size: 6μL

Test 1	Test 2	Test 3
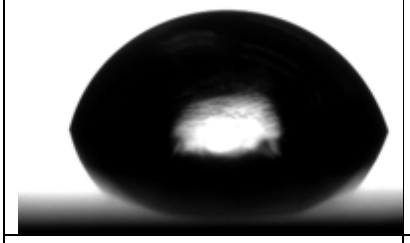	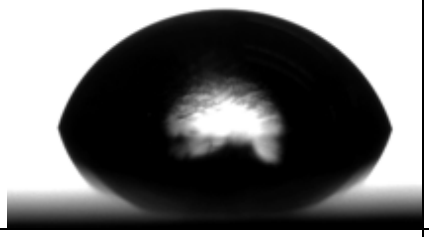	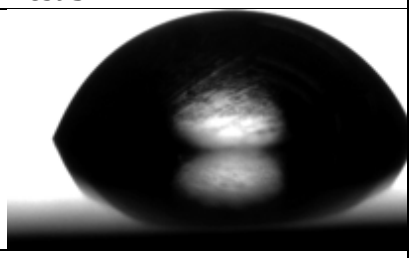
82.15	81.93	79.69

Alloy: Al-25%Si Sand Paper Grit size: 800 Droplet Size: 6μL

Test 1	Test 2	Test 3	Test 4
			
62.26	64.99	62.27	65.05

Alloy: Al-25%Si Sand Paper Grit size: 240 Droplet Size: 8μL

Test 1	Test 2	Test 3
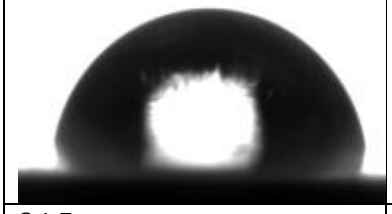	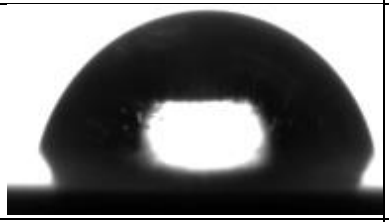	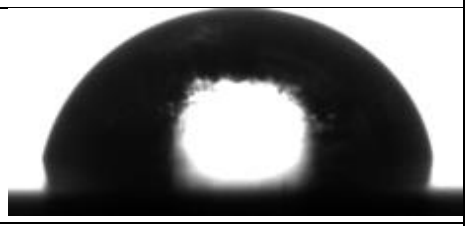
84.5	82.52	85.16

Alloy: Al-25%Si Sand Paper Grit size: 400 Droplet Size: 8μL

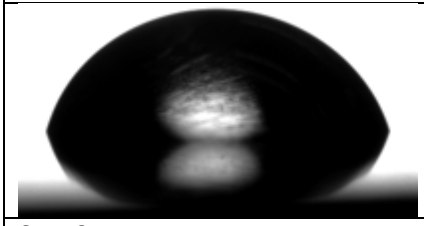	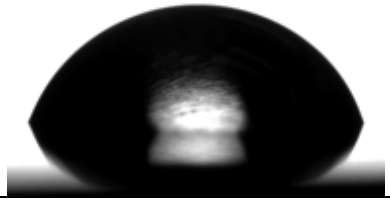	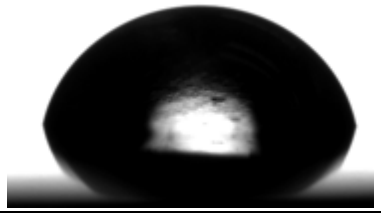
81.79	80.34	83.71

Alloy: Al-25%Si Sand Paper Grit size: 800 Droplet Size: 8μL

		
64.92	64.13	68.78

Alloy: Al-25%Si Sand Paper Grit size: 240 Droplet Size: 10μL

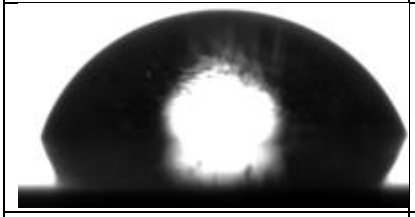	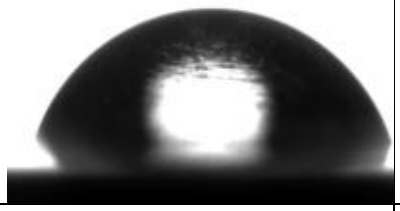	
80.69	78.86	82.26

Alloy: Al-25%Si Sand Paper Grit size: 400 Droplet Size: 10μL

Test 1	Test 2	Test 3
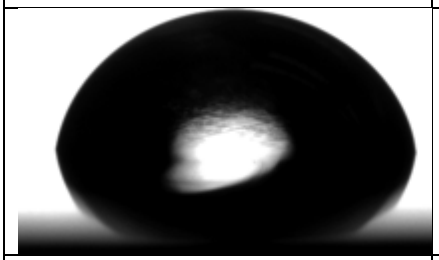	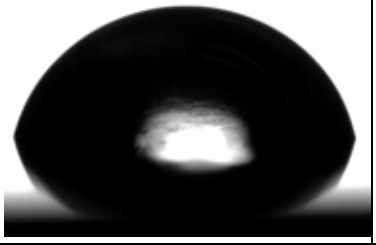	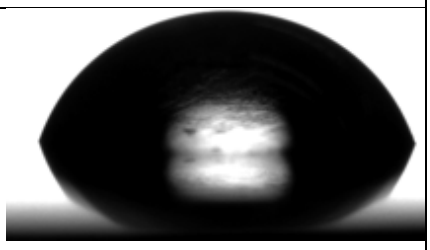
85.71	83.48	80.27

Alloy: Al-25%Si Sand Paper Grit size: 800 Droplet Size: 10μL

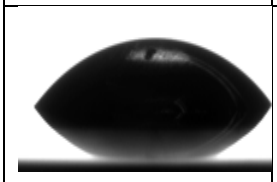		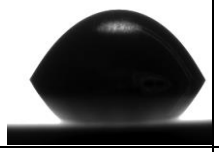	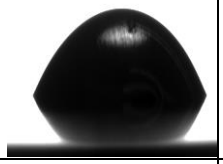	
59.69	59.55	57.01	62.35	61.85

Alloy: Al-32%Si Sand Paper Grit size: 240 Droplet Size: 4μL

	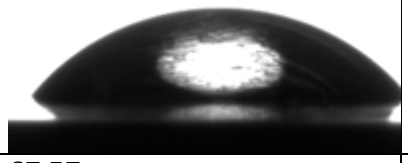	
66.11	67.57	69.41

Alloy: Al-32%Si Sand Paper Grit size: 400 Droplet Size: 4μL

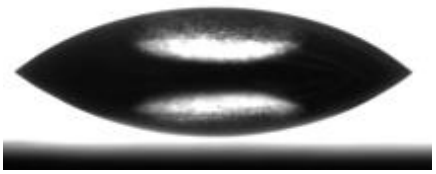		
58.66	61.50	66.11

Alloy: Al-32%Si Sand Paper Grit size: 800 Droplet Size: 4μL

			
64.97	61.26	60.43	61.90

Alloy: Al-32%Si Sand Paper Grit size: 240 Droplet Size: 6μL

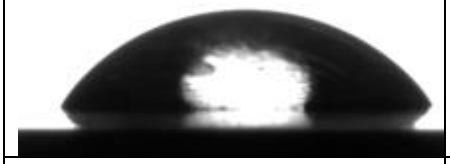	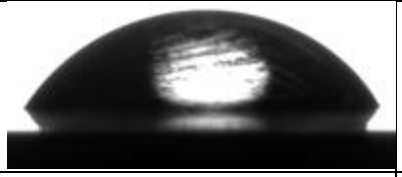	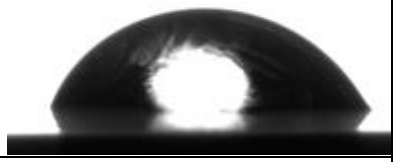
71.78	73.20	76.72

Alloy: Al-32%Si Sand Paper Grit size: 400 Droplet Size: 6μL

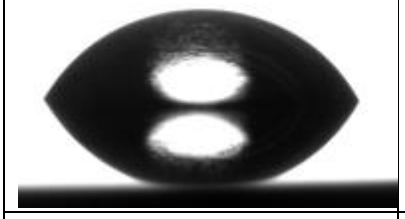	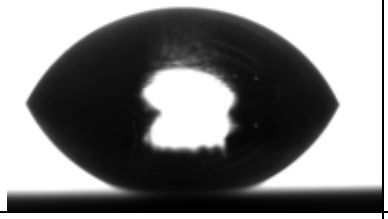	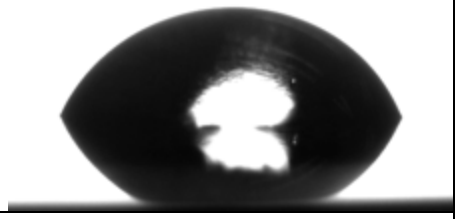
74.26	76.50	78.08

Alloy: Al-32%Si Sand Paper Grit size: 800 Droplet Size: 6μL

		
61.61	64.68	64.69

Alloy: Al-32%Si Sand Paper Grit size: 240 Droplet Size: 8μL

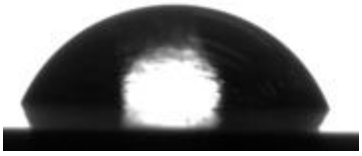	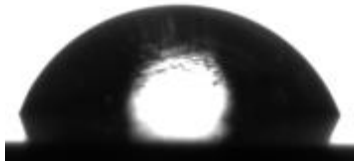	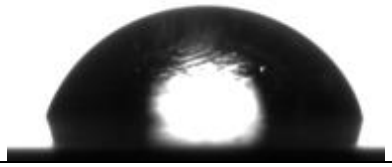
78.16	79.48	81.94

Alloy: Al-32%Si Sand Paper Grit size: 400 Droplet Size: 8μL

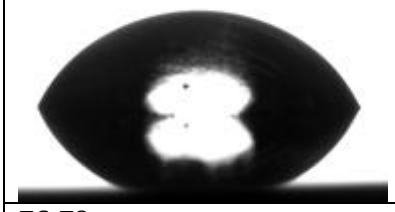	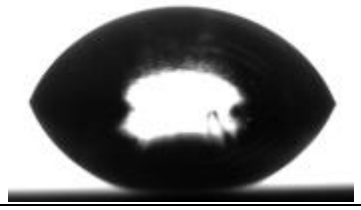	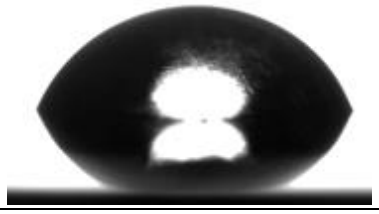
76.79	78.62	78.97

Alloy: Al-32%Si Sand Paper Grit size: 800 Droplet Size: 8μL

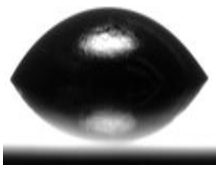	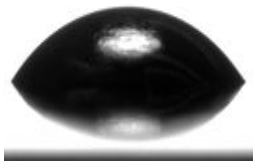	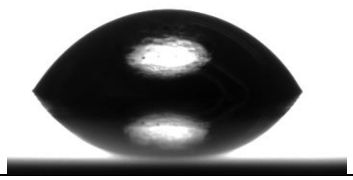	
63.85	65.70	68.98	68.74

Alloy: Al-32%Si Sand Paper Grit size: 240 Droplet Size: 10μL

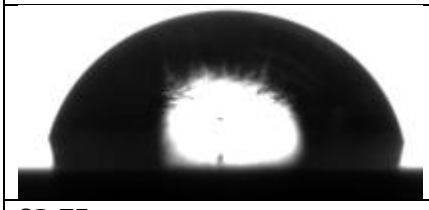	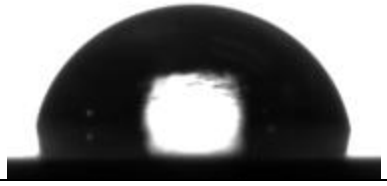	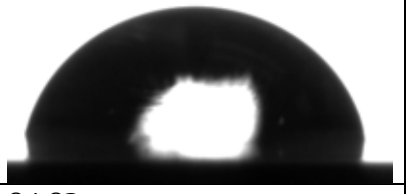
82.75	85.12	84.82

Alloy: Al-32%Si Sand Paper Grit size: 400 Droplet Size: 10μL

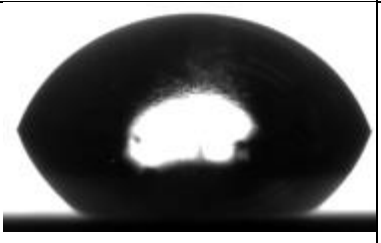	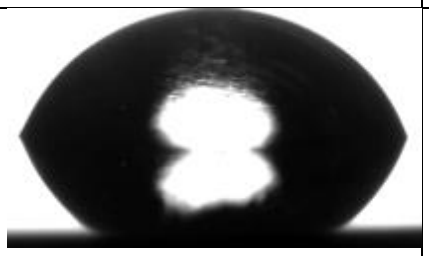	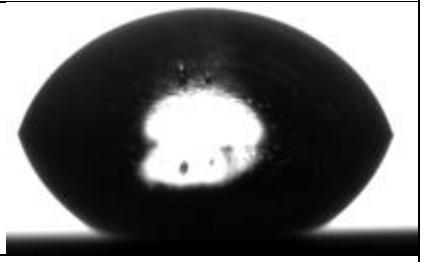
79.85	78.89	80.98

Alloy: Al-32%Si Sand Paper Grit size: 800 Droplet Size: 10μL

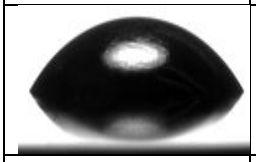	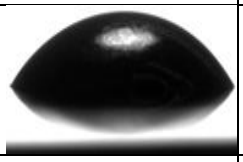	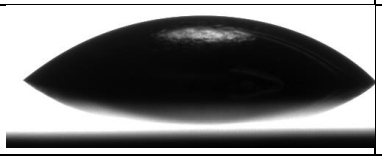	
66.15	65.31	60.54	62.61

Alloy: Al-50%Si Sand Paper Grit size: 240 Droplet Size: 4μL

		
66.89	66.65	63.11

Alloy: Al-50%Si Sand Paper Grit size: 400 Droplet Size: 4μL

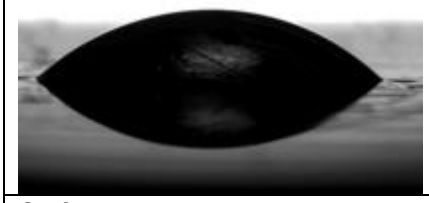	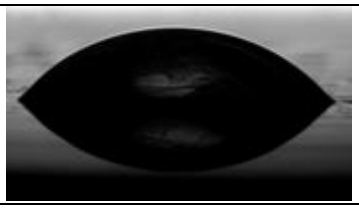	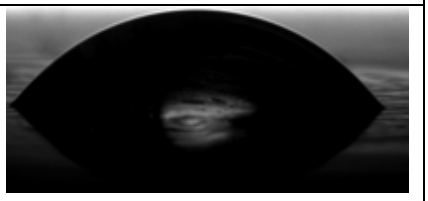
61.07	66.34	67.99

Alloy: Al-50%Si Sand Paper Grit size: 800 Droplet Size: 4μL

	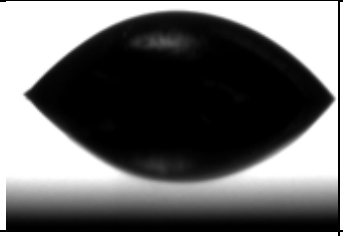	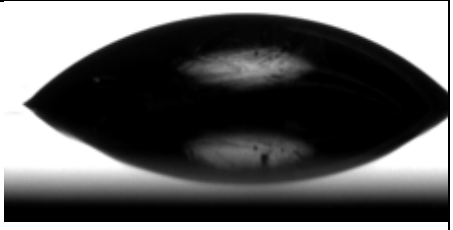
51.94	58.46	62.96

Alloy: Al-50%Si Sand Paper Grit size: 240 Droplet Size: 6µL

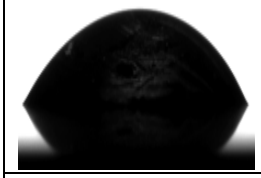		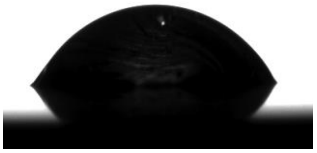	
67.57	67.43	69.19	66.46

Alloy: Al-50%Si Sand Paper Grit size: 400 Droplet Size: 6µL

	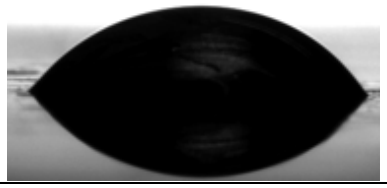	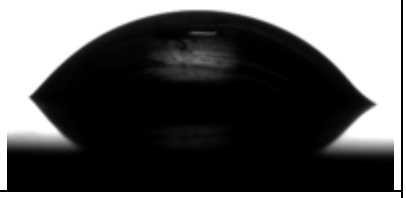
65.47	69.76	68.60

Alloy: Al-50%Si Sand Paper Grit size: 800 Droplet Size: 6µL

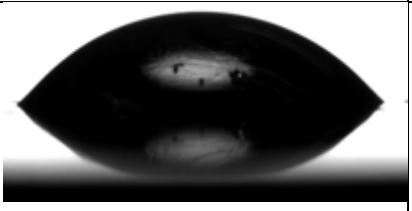	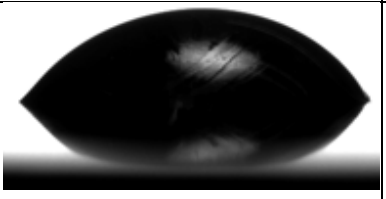	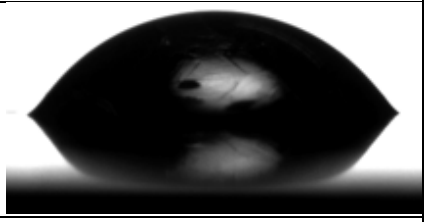
63.84	69.55	70.31

Alloy: Al-50%Si Sand Paper Grit size: 240 Droplet Size: 8µL

		
63.98	67.04	65.17

Alloy: Al-50%Si Sand Paper Grit size: 400 Droplet Size: 8μL

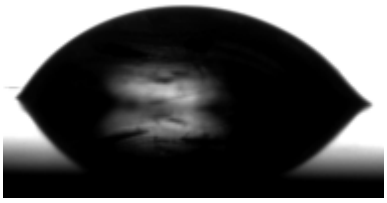	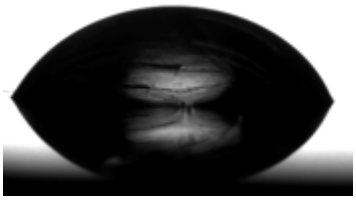	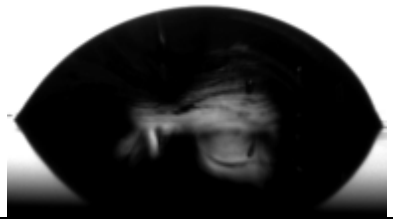
70.92	76.71	76.97

Alloy: Al-50%Si Sand Paper Grit size: 800 Droplet Size: 8μL

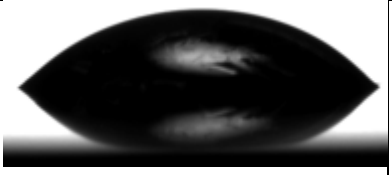	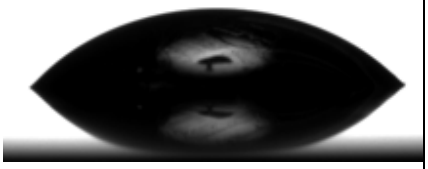	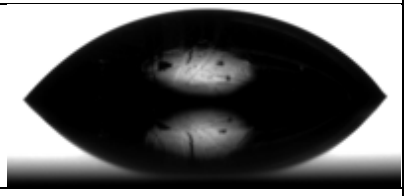
63.25	64.26	68.85

Alloy: Al-50%Si Sand Paper Grit size: 240 Droplet Size: 10μL

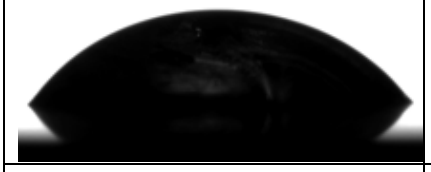		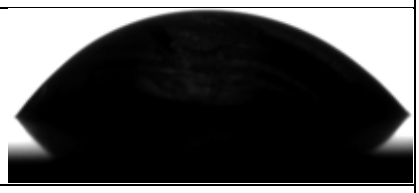
68.71	66.49	65.00

Alloy: Al-50%Si Sand Paper Grit size: 400 Droplet Size: 10μL

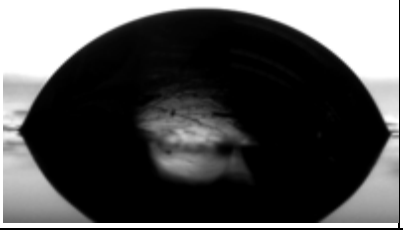	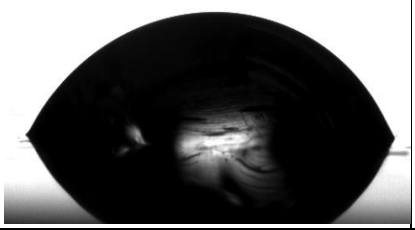	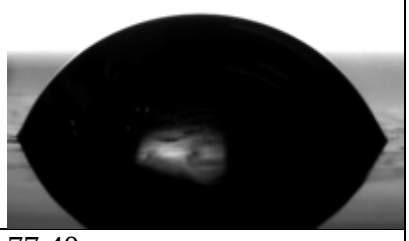
78.86	74.94	77.40

Alloy: Al-50%Si Sand Paper Grit size: 800 Droplet Size: 10μL

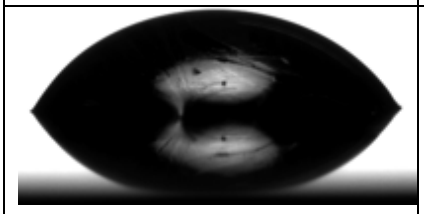	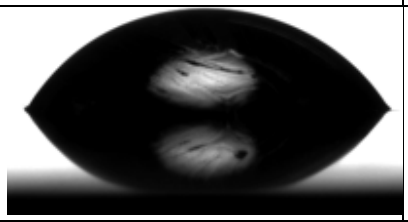	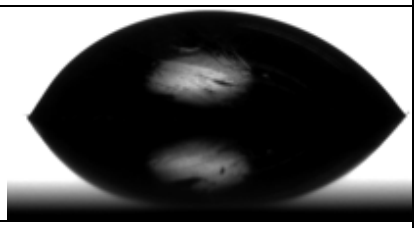
73.43	71.37	73.01

Appendix B

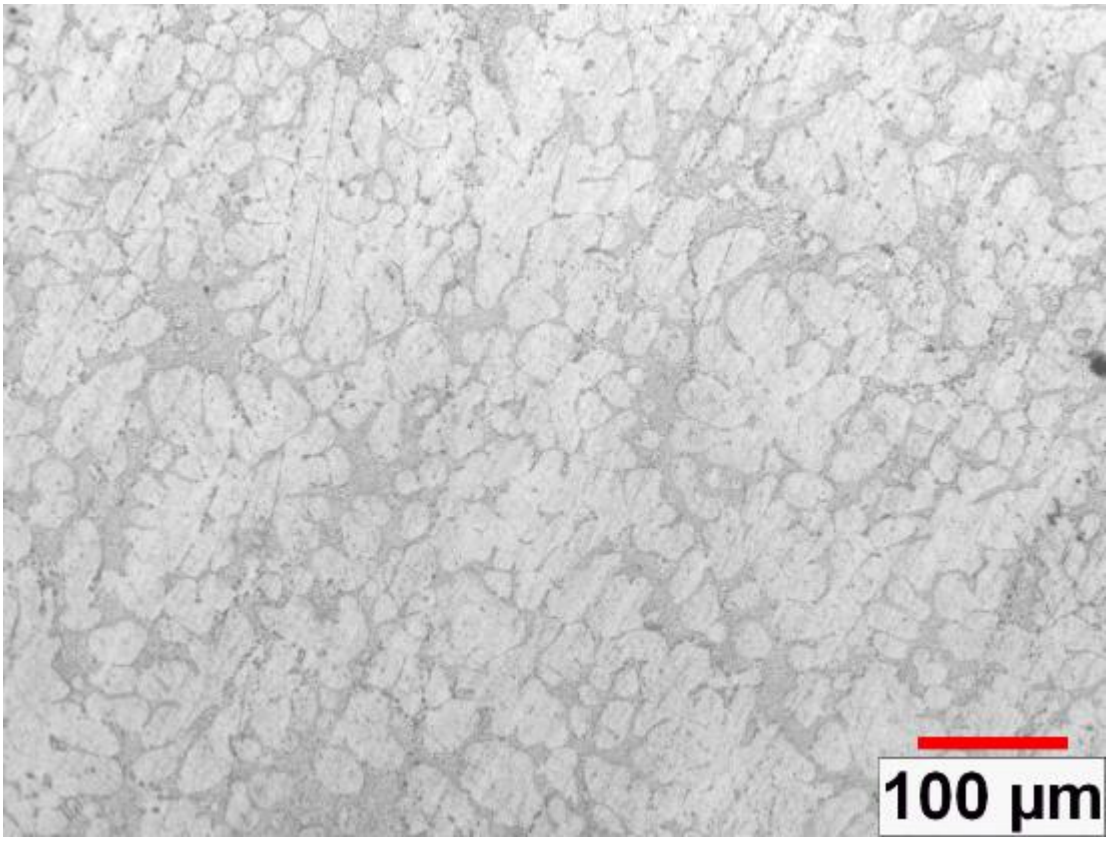

Figure 37: Microstructure for A356 by Optical Microscope showing α aluminum dendrites and Al-Si eutectic

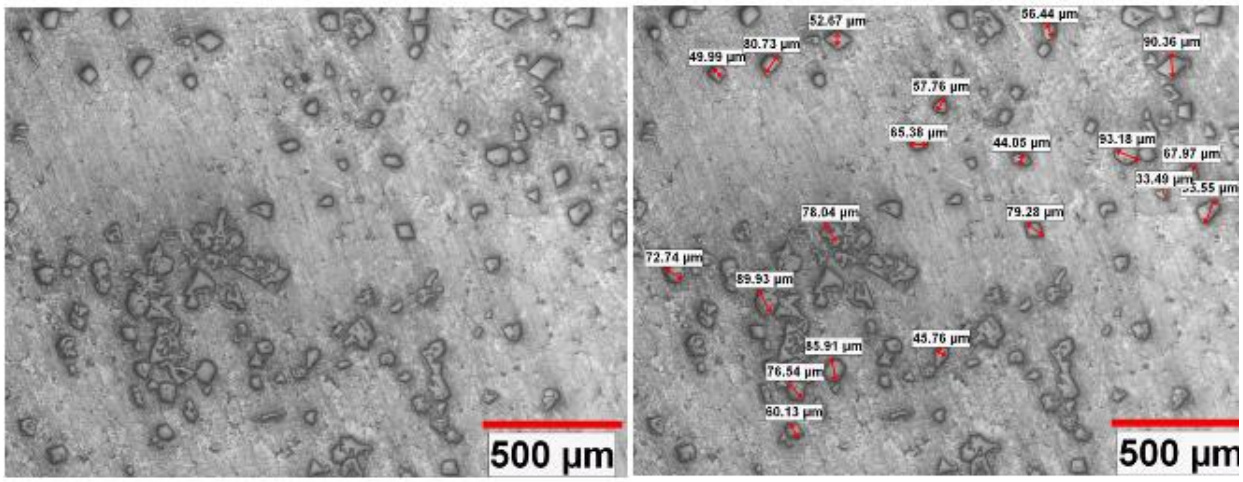

Figure 38: Microstructure for Al-22%Si by Optical Microscope (Primary Si size in right picture), showing primary Silicon of size 33.49µm to 93.16µm

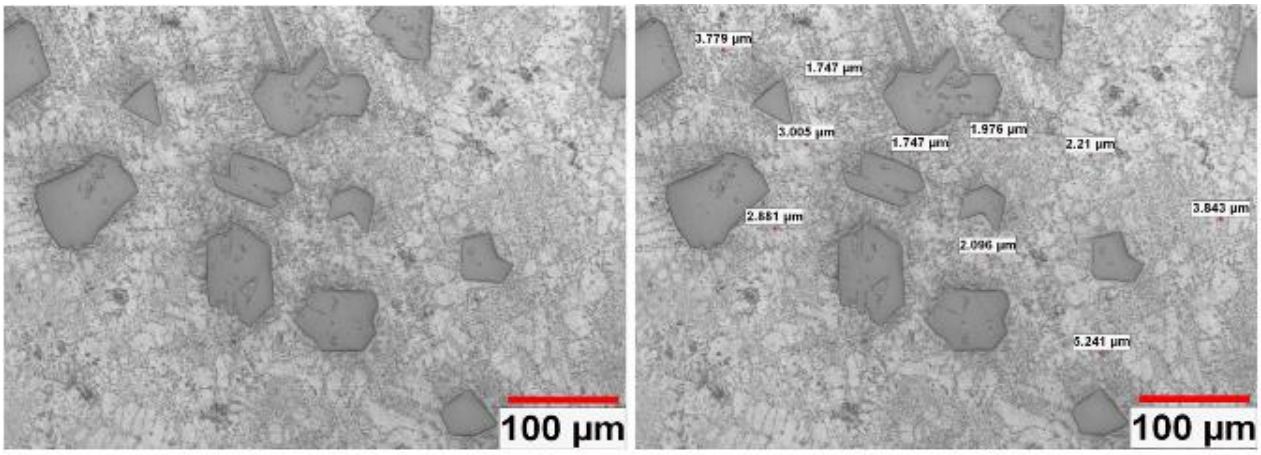

Figure 39: Microstructure for Al-22%Si by Optical Microscope (Eutectic Si size in right picture) showing primary Silicon particles, aluminum dendrites and Al-Si eutectic

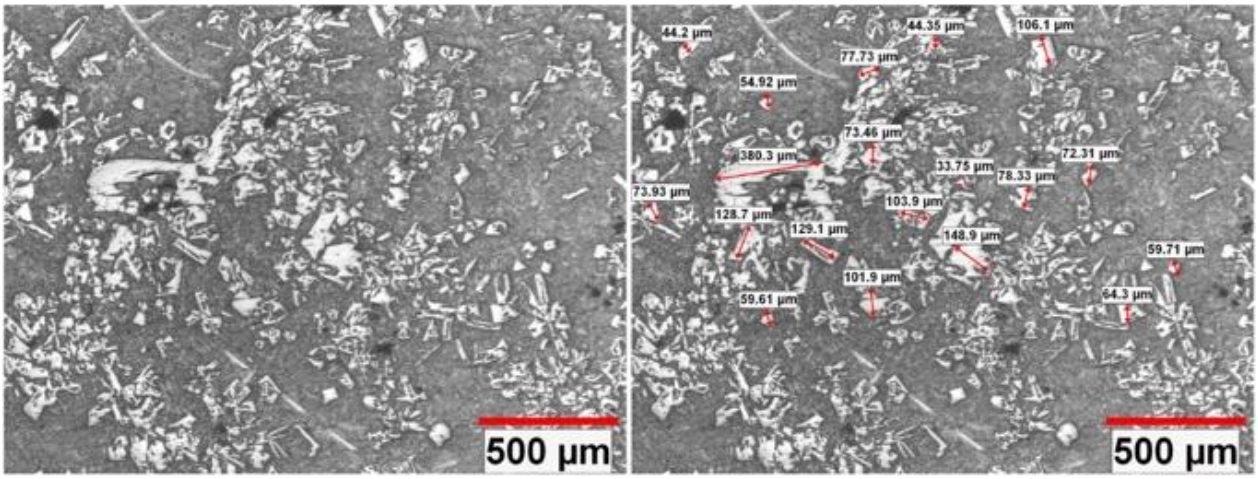

Figure 40: Microstructure for Al-25%Si by Optical Microscope (Primary Si size in right picture)

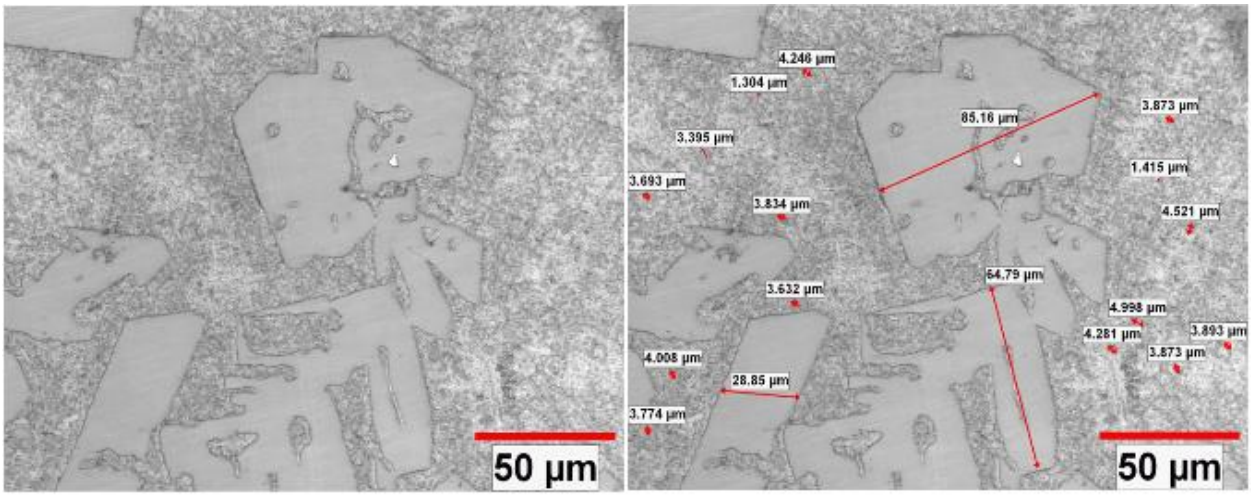

Figure 41: Microstructure for Al-25%Si by Optical Microscope (Eutectic Si size in right picture) showing primary Silicon particles of average size 18.79µm

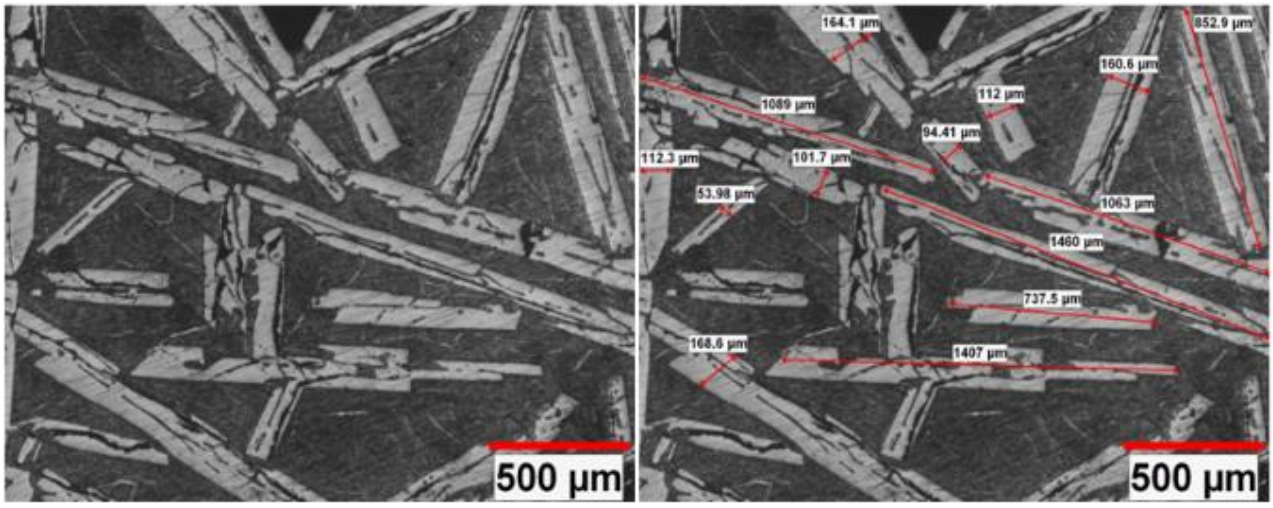

Figure 42: Microstructure for Al-50%Si by Optical Microscope (Primary Si size in right picture)

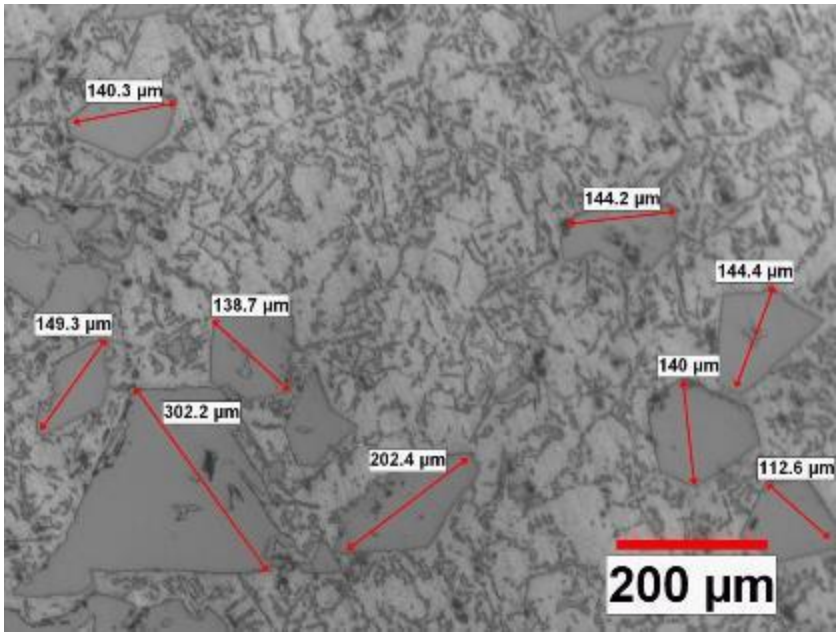

Figure 43: Size of Primary Silicon for Al-22%Si polished with 240 grit sand paper (average size 163.79µm)

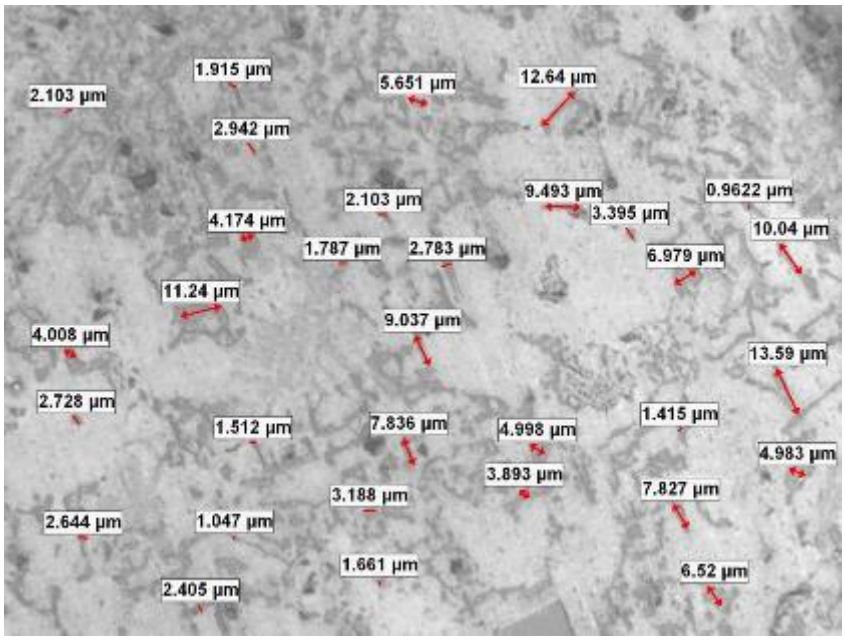

Figure 44: Size of eutectic Si for Al-22%Si polished with 240 grit size sand paper (average size 5.07µm)

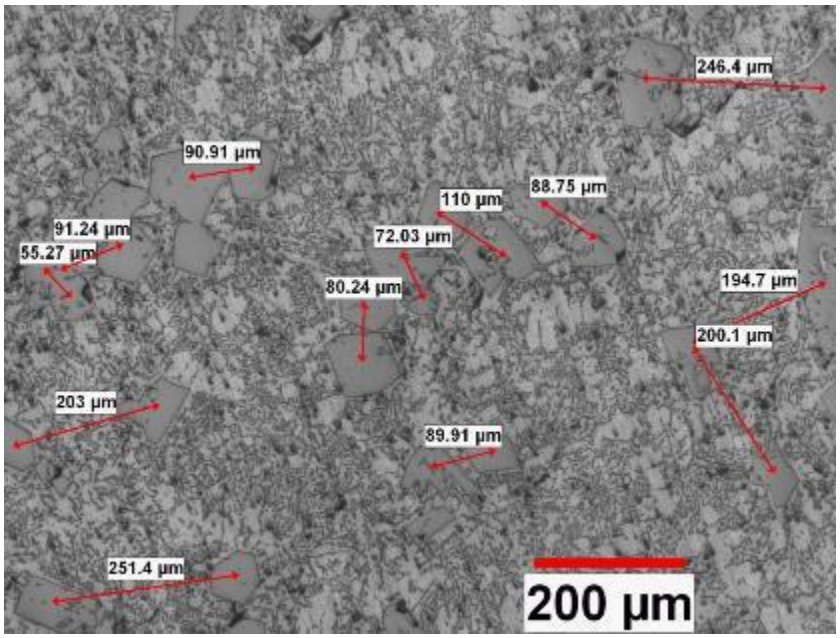

Figure 45: Interparticle distance between primary Si particles for Al-22% Si roughened with 240 grit size sand paper (average distance 136.46µm)

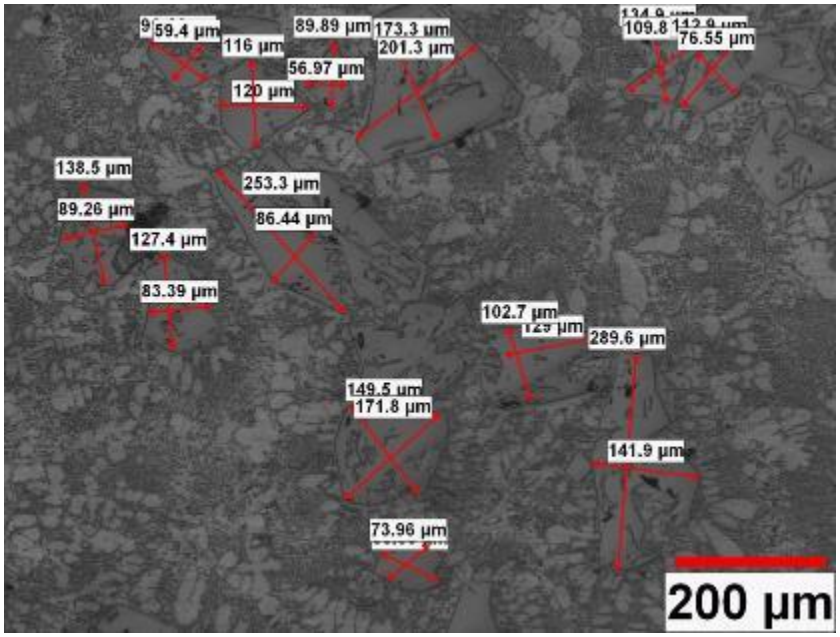

Figure 46: Particle size for primary silicon for Al-24%SI polished with 240 grit size sand paper

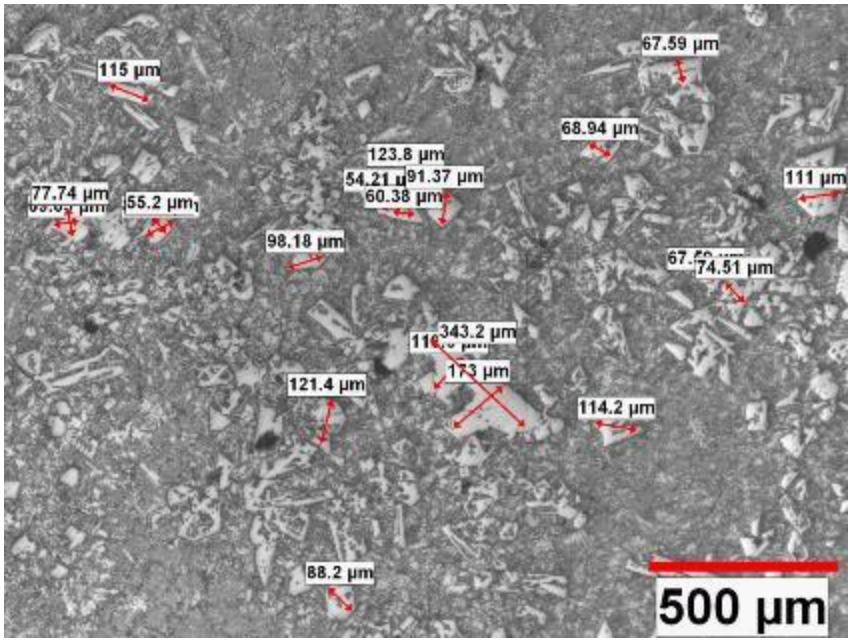

Figure 47: Size of primary Si for Al-25% Si polished with 240 grit size sand paper (average size 104.76µm)

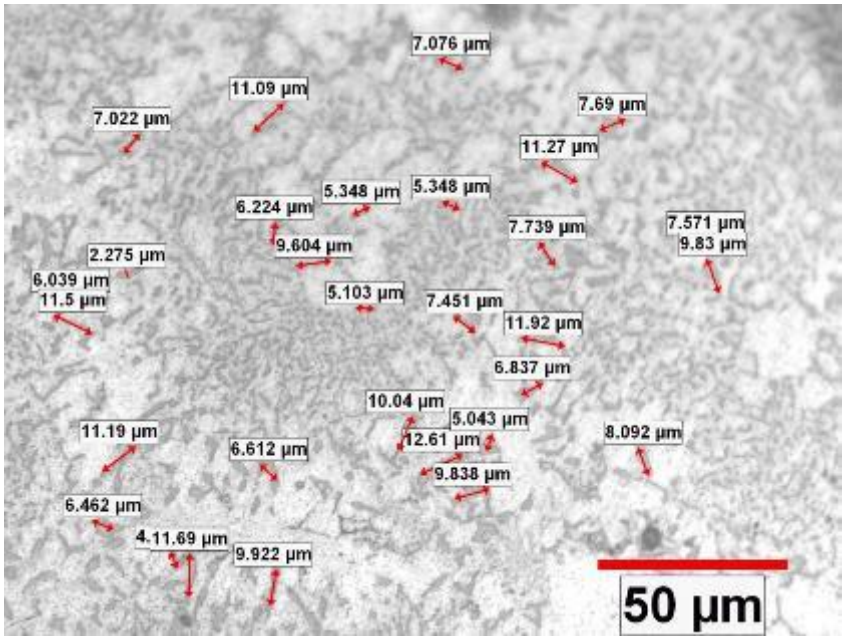

Figure 48: Size of Eutectic Silicon for Al-25%Si polished with 240 grit size (average size 7.57µm)

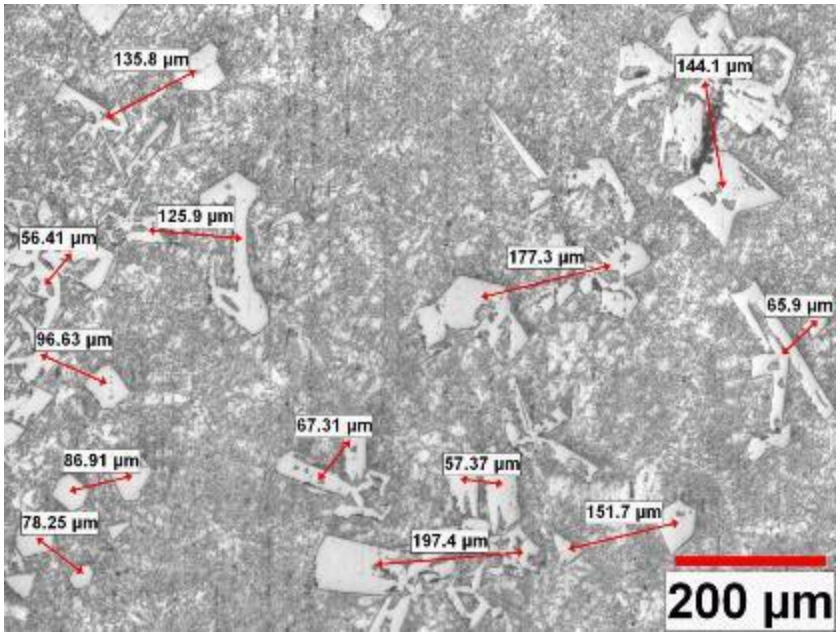

Figure 49: Interparticle distance between primary Si particles for Al-25% Si polished with 240 grit size (average distance 110.85µm)

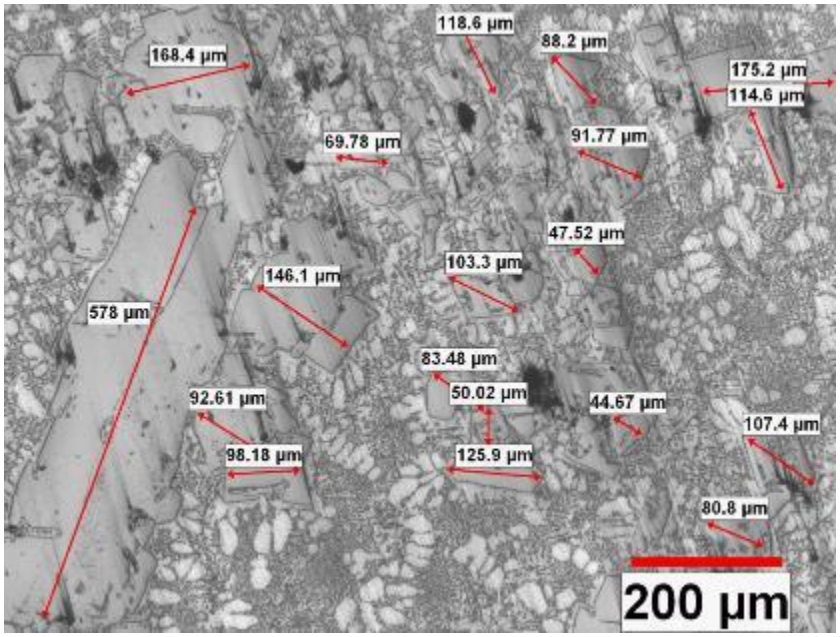

Figure 50: Primary Si particle size for Al-32%Si polished with 240 grit size sand paper (average size 115µm)

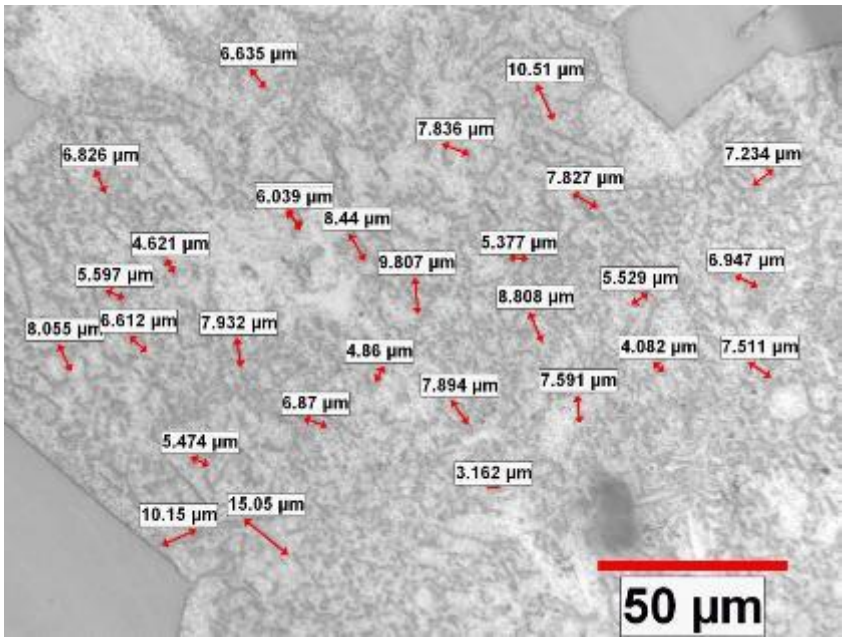

Figure 51: Size of eutectic Silicon for Al-32%Si polished with 240 grit size sand paper (average size 6.865µm)

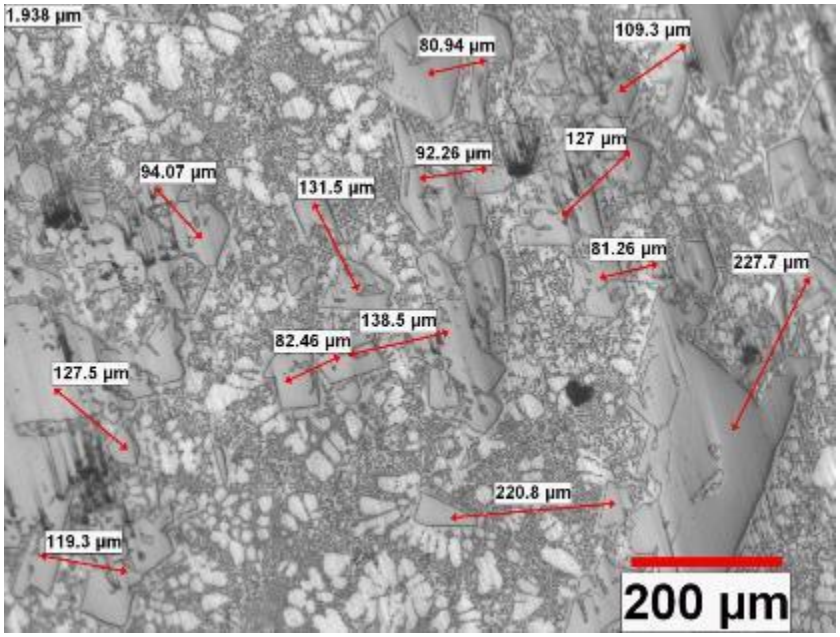

Figure 52: Interparticle distance between primary Si particles for Al-32%Si with 240 grit size sand paper(average spacing 116.74µm)

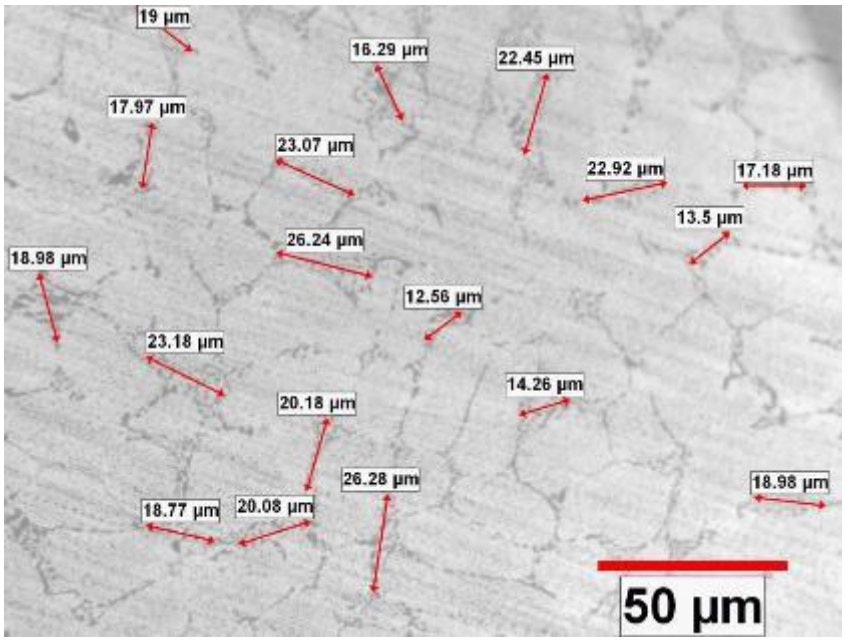

Figure 53: Size of eutectic Si in Al-356 polished with 240 grit size (average size 19.55µm)

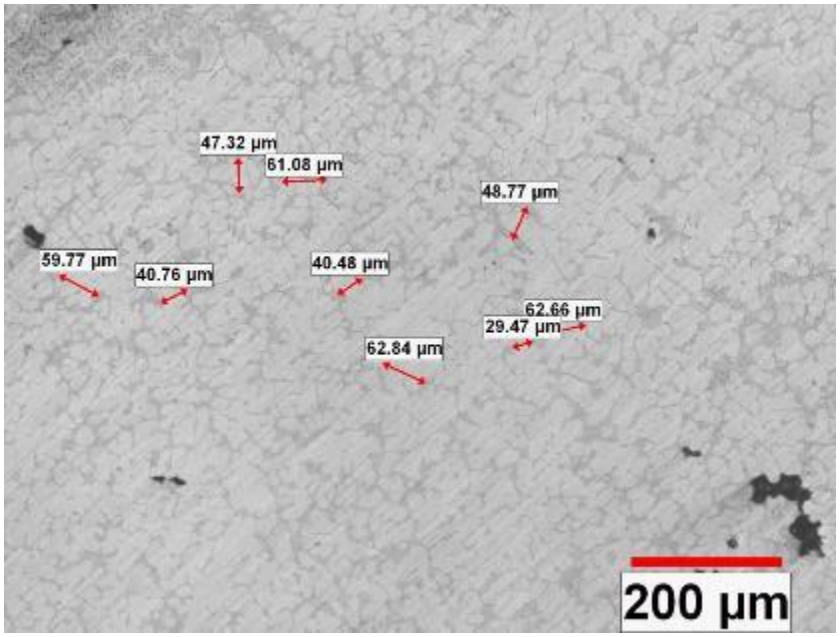

Figure 54: Interparticle spacing for eutectic Si in Al-356 polished with 240 grit size (average distance 50.35µm)

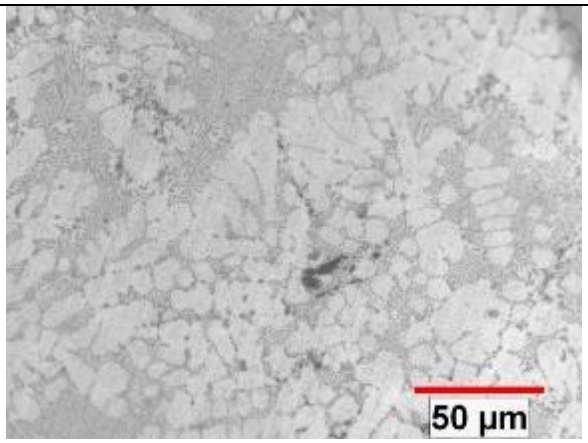

Figure 55: Microstructure of Al-360 polished with 240 grit size

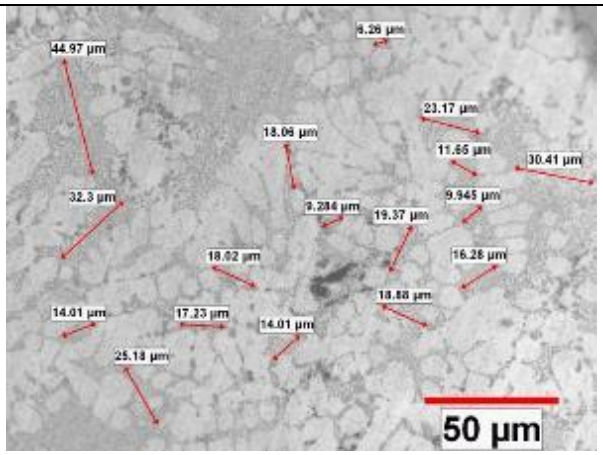

Figure 56: Size of eutectic Si for Al-360 polished with 240 grit size (average size 19.35µm)

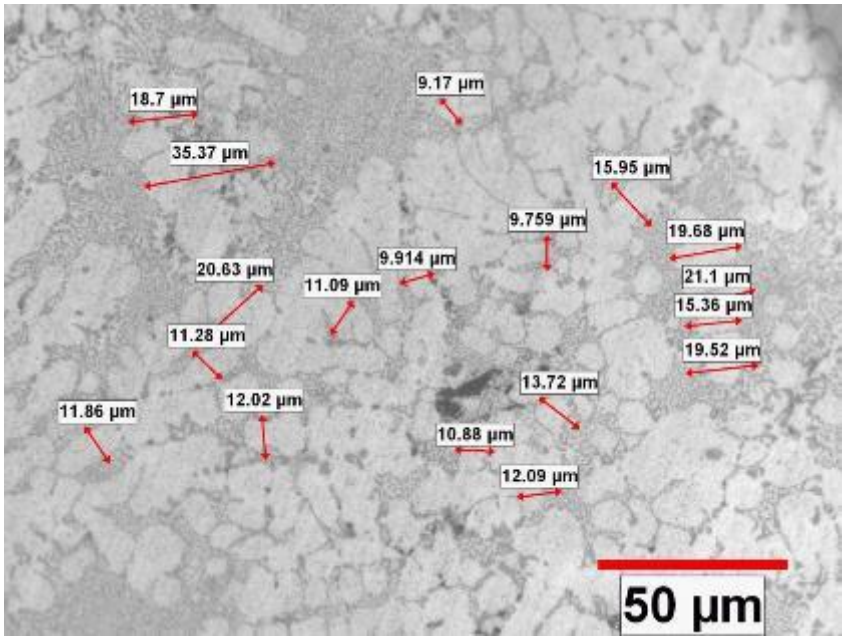

Figure 57: Interparticle distance between eutectic Si for Al-360 polished with 240 grit size sand paper (average spacing 15.45µm)

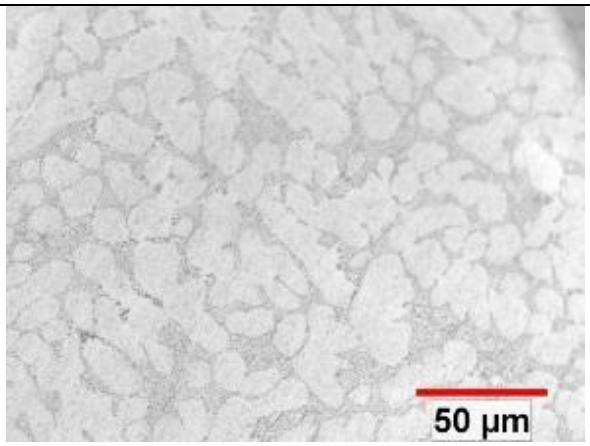

Figure 58: Microstructure for Al-368 240 grit size sand paper

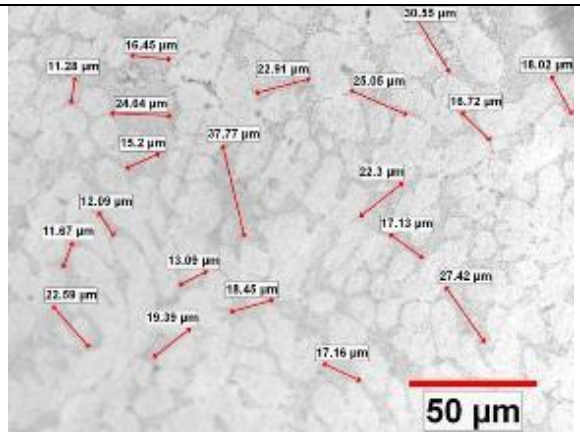

Figure 59: Size of eutectic Si for Al-368 240 grit size sand paper (average size 20.50µm)

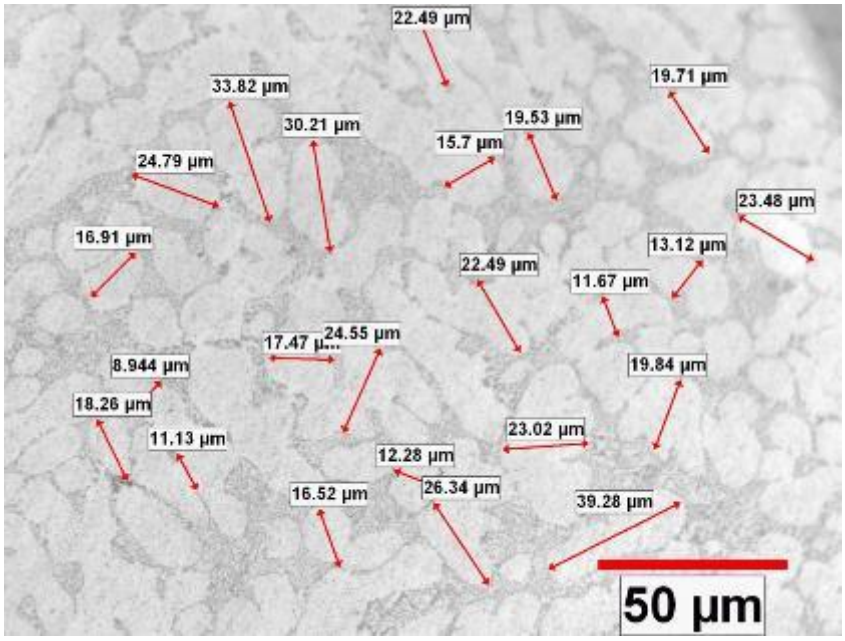

Figure 60: Interparticle spacing between eutectic Si particles for Al-368 (Average size 20.50µm)

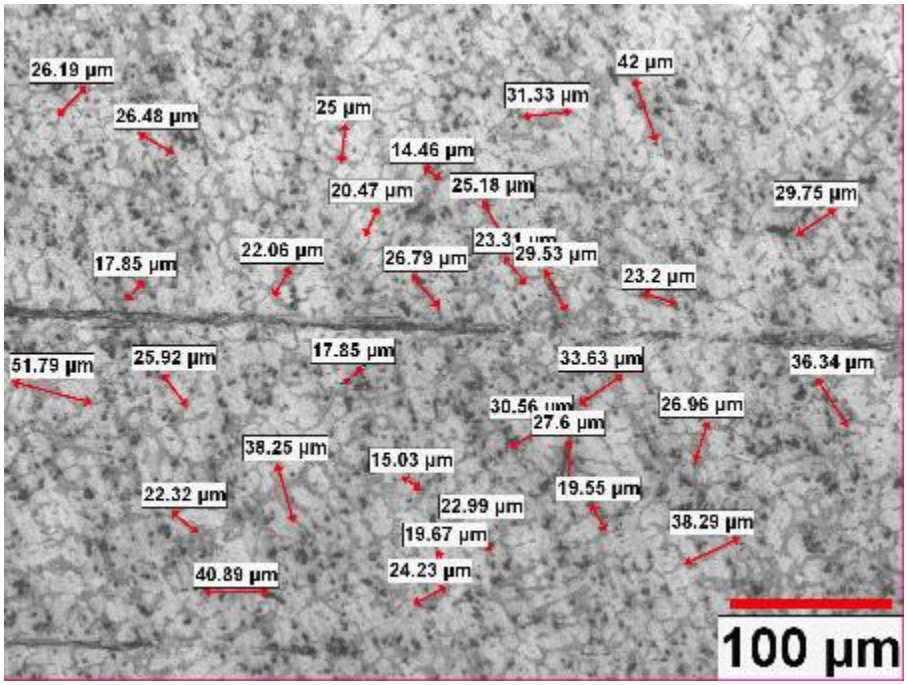

Figure 61: Microstructure of Al-356 polished with 800 grit size sand paper showing size of eutectic Si (Average size 27.36µm)

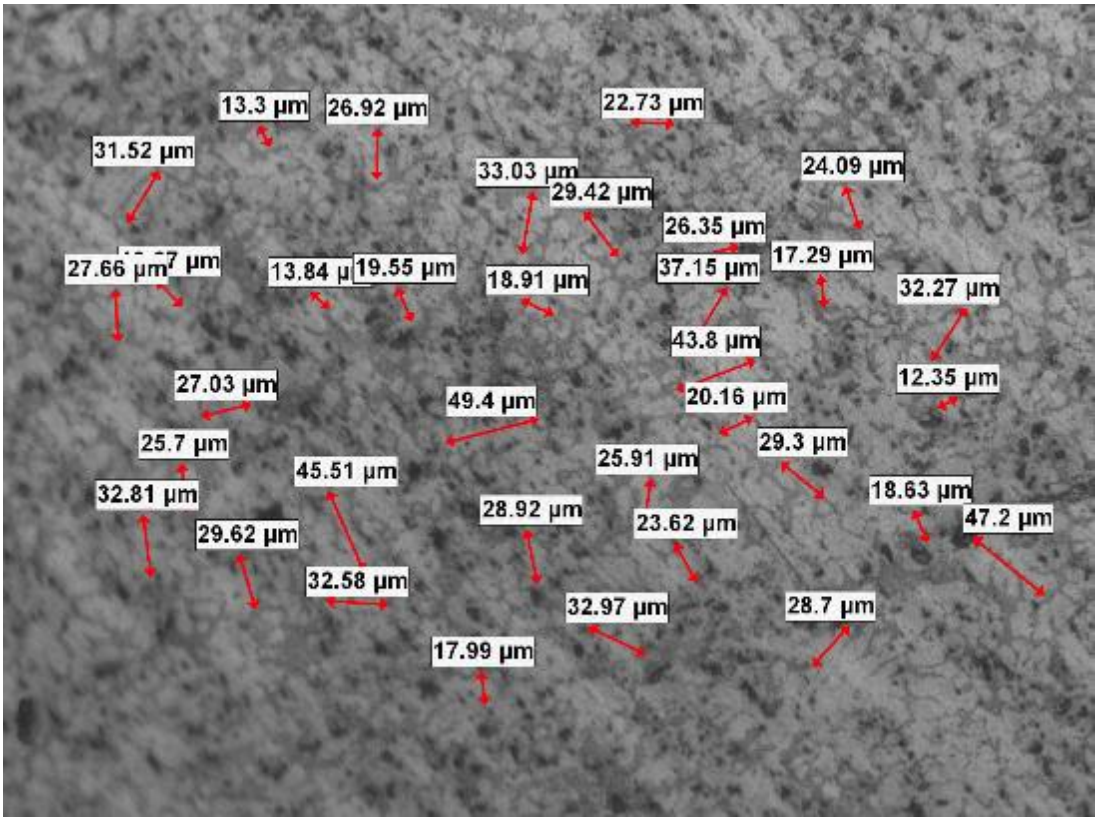

Figure 62: Microstructure of Al-356 polished with 800 grit size sand paper showing interdendritic spacing in eutectic Silicon at 500x (Average size 27.58µm)

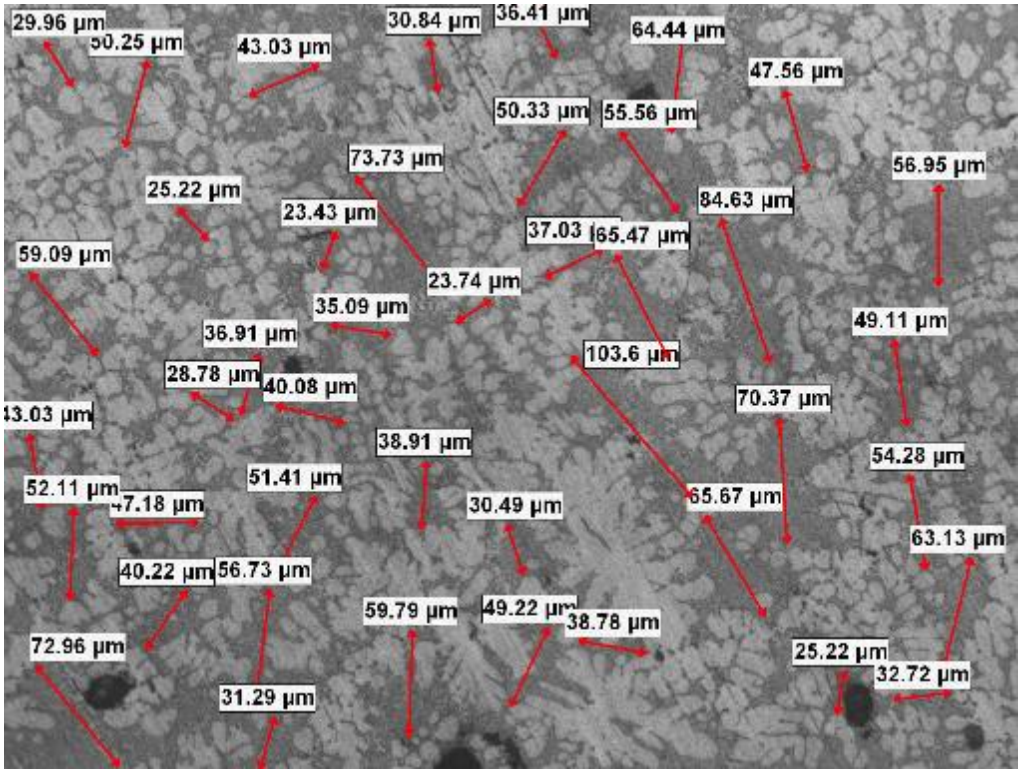

Figure 63: Size of eutectic Si for Al-360 sample polished with 800 grit size sand paper at 500x. (Average size 48.25µm)

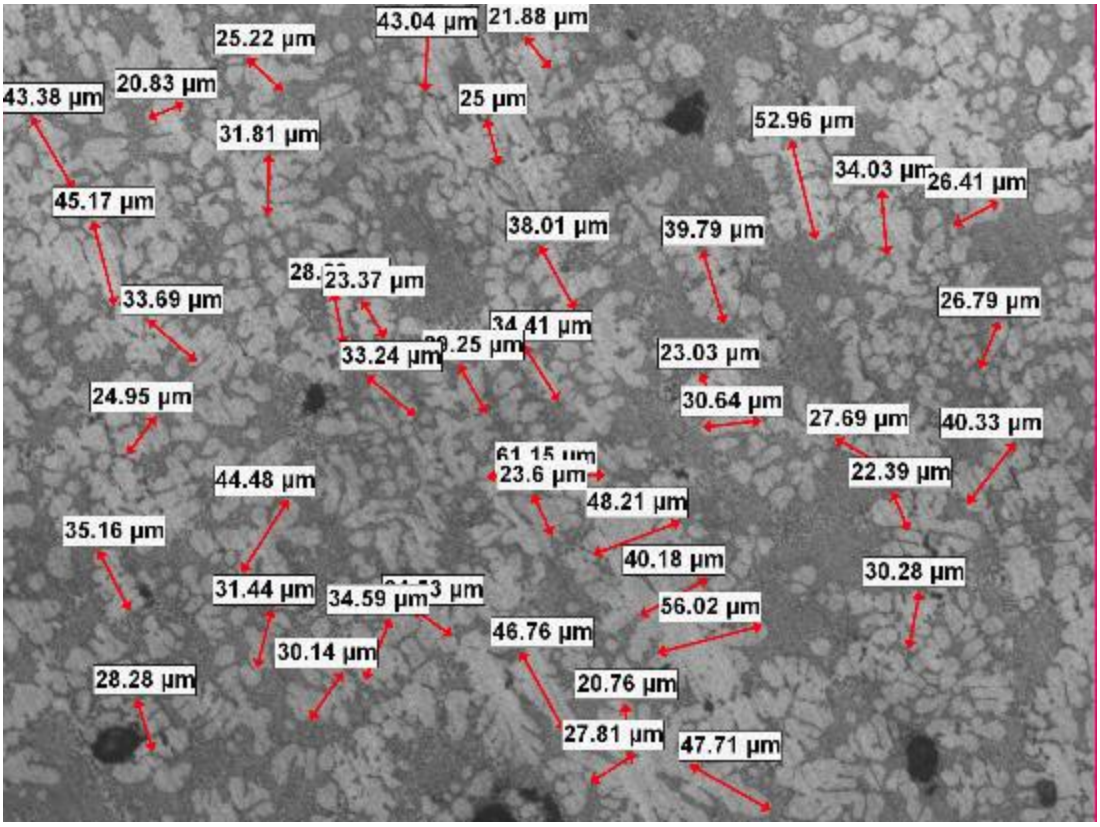

Figure 64: Interdendritic spacing for Al-360 sample polished with 800 grit size sand paper at 500x (Average spacing 33.88µm)

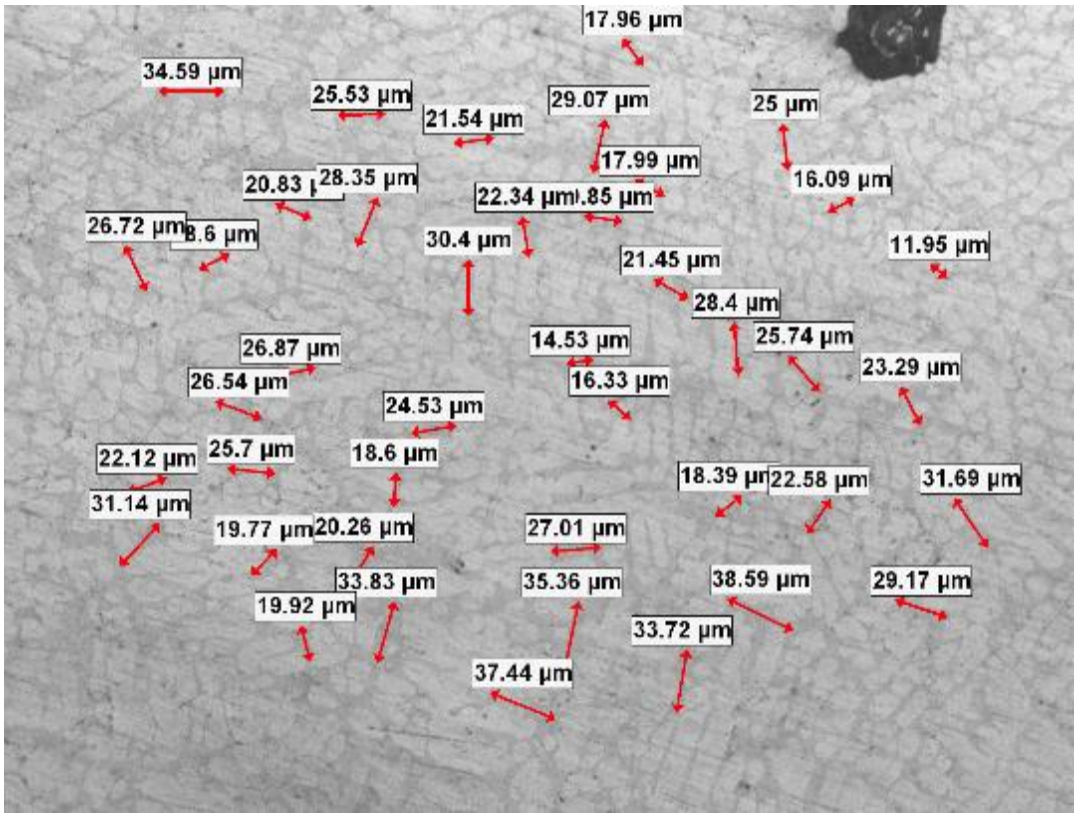

Figure 65: Size of eutectic Si in Al-368 sample polished with 800 grit size sand paper at 500x (Average size 24.78µm)

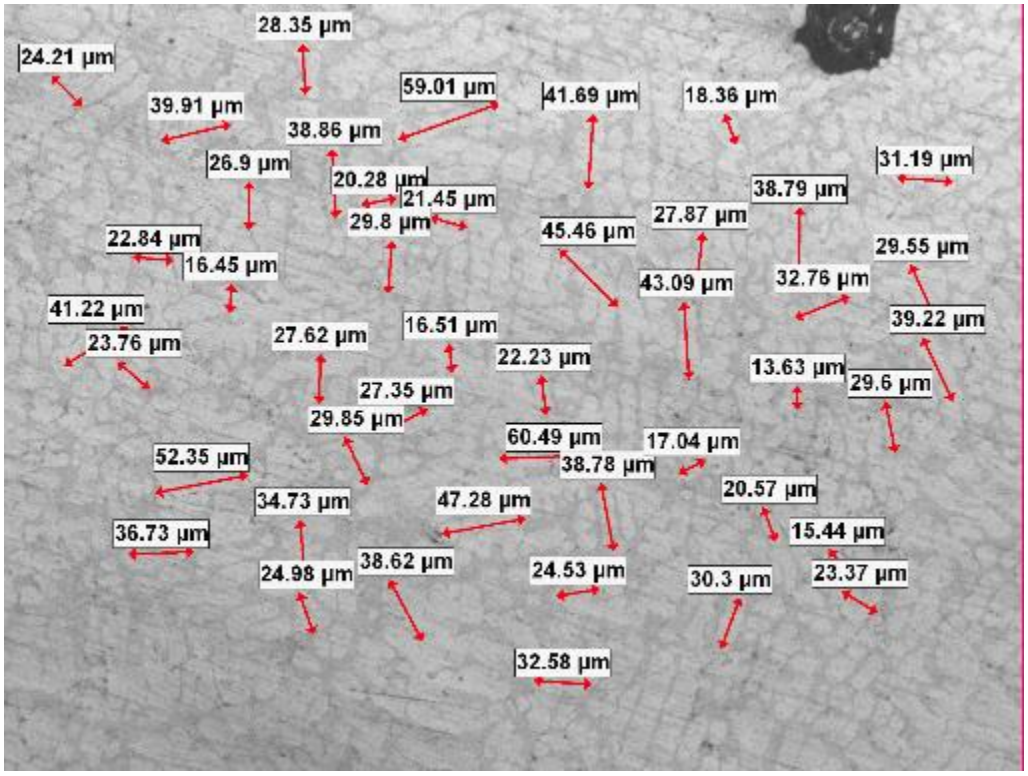

Figure 66: Interparticle spacing in Al-368 sample polished with 800 grit size sand paper at 500x (Average spacing 31.24µm)

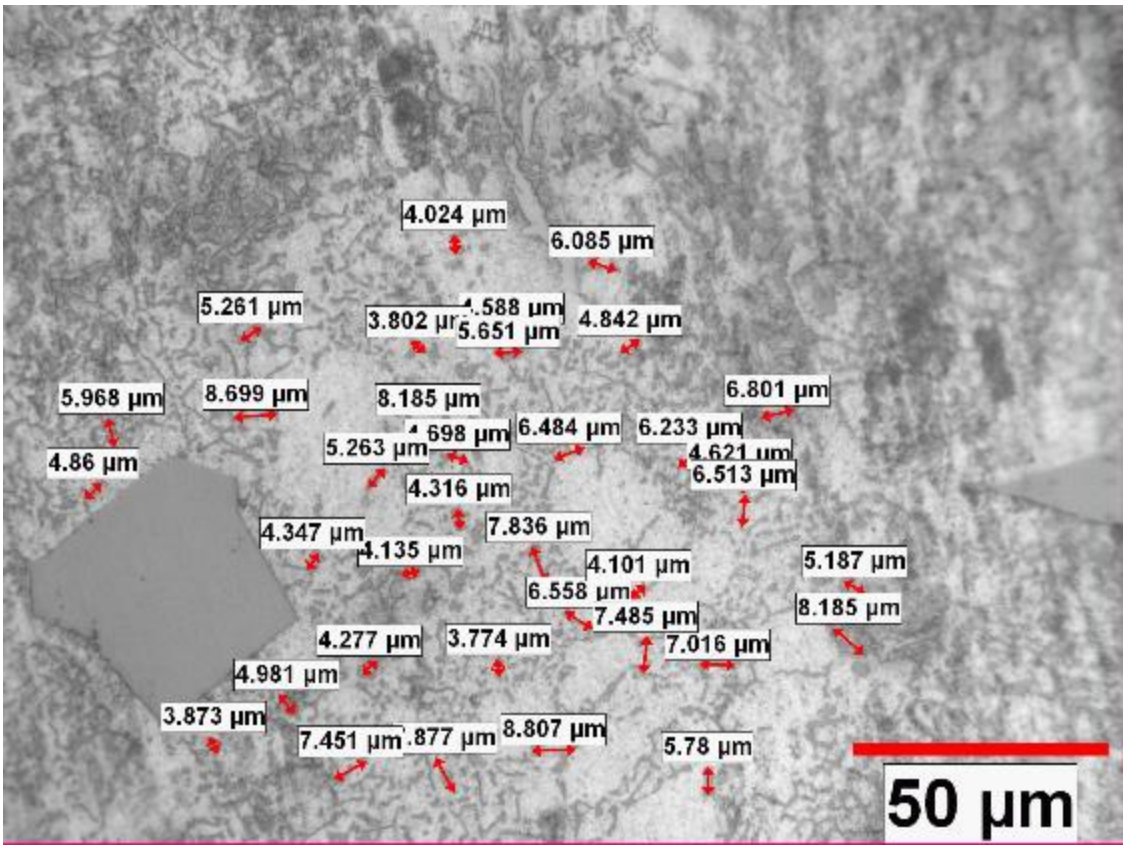

Figure 67: Size of eutectic Silicon in Al-22%Si sample pre-polished with 800 grit size sand paper at 500x. (Average size 5.79µm)

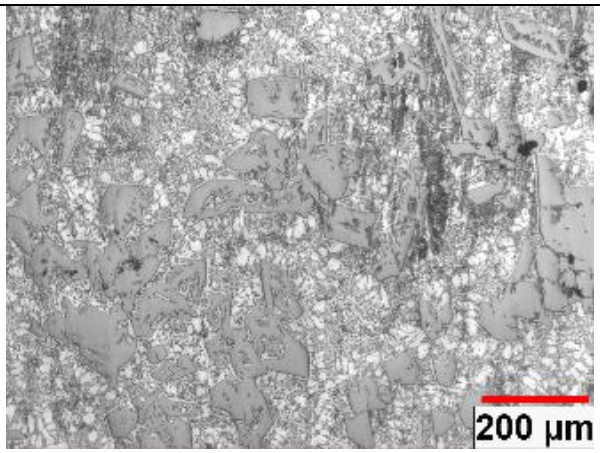

Figure 68: Microstructure of Al-22%Si sample pre-polished with 800 grit size sand paper

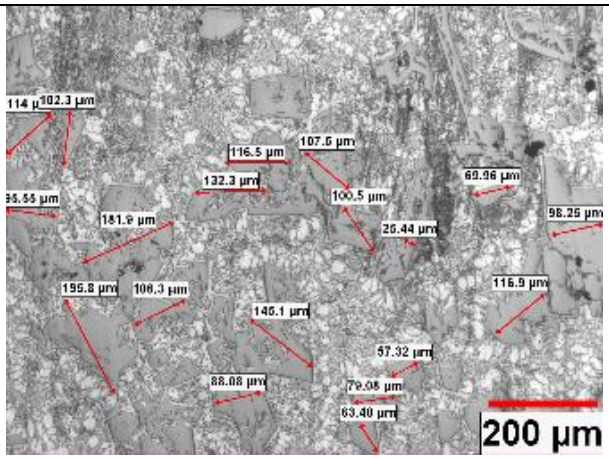

Figure 69: Size of primary Silicon in Al-22%Si sample pre-polished with 800 grit sand paper (Average size 105.07µm)

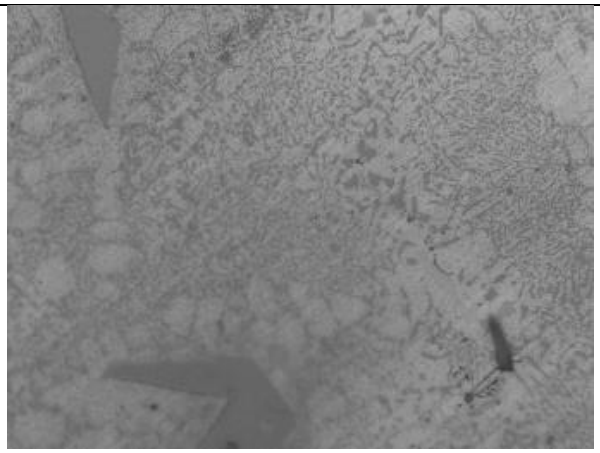

Figure 70: Microstructure of Al-24%Si at 1000x

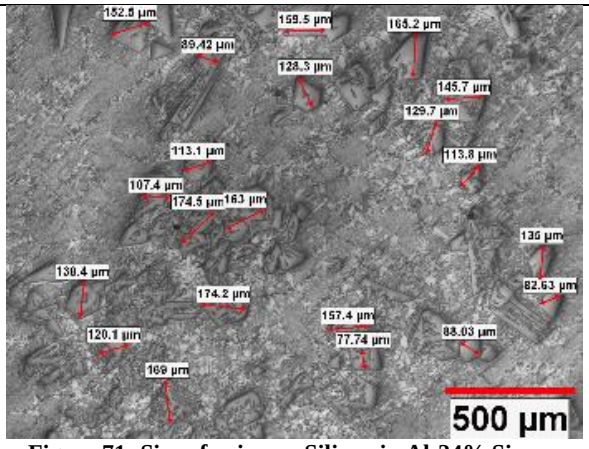

Figure 71: Size of primary Silicon in Al-24% Si pre-polished with 800 grit size sand paper (Average size 132.61µm)

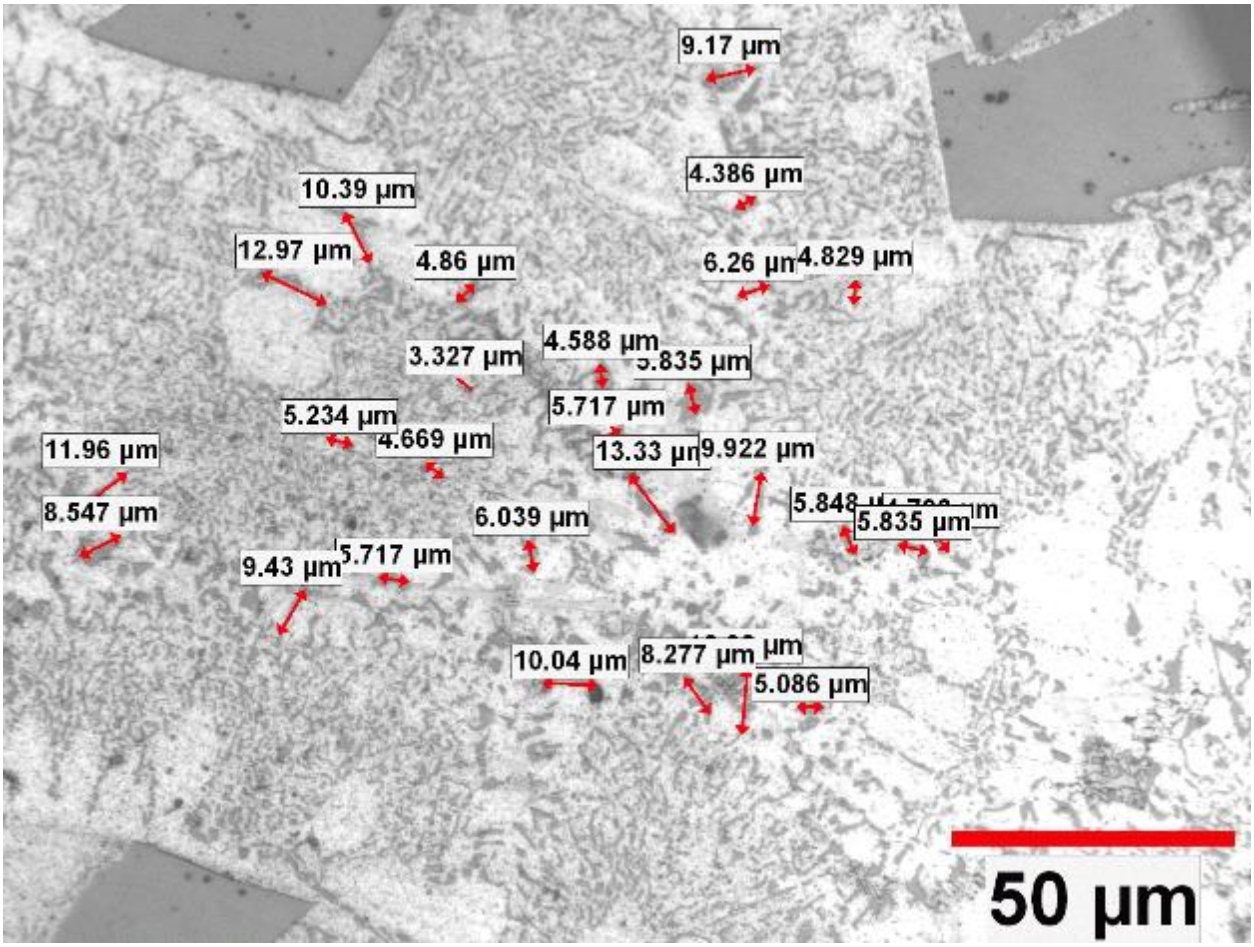

Figure 72: Al-25%Si microstructure pre-polished with 800 grit size sand paper at 500x showing eutectic Silicon size (Average size 7.37µm)

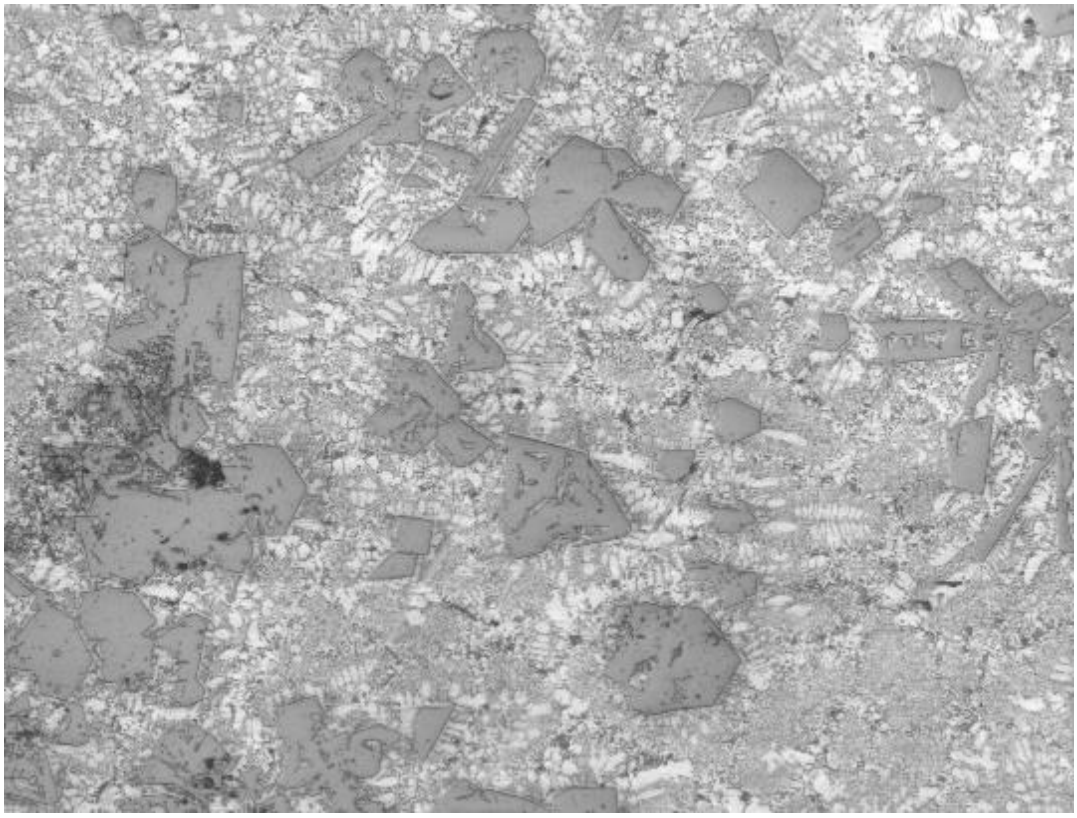

Figure 73: Microstructure of Al-25%Si pre-polished with 800 grit sand paper at 200x

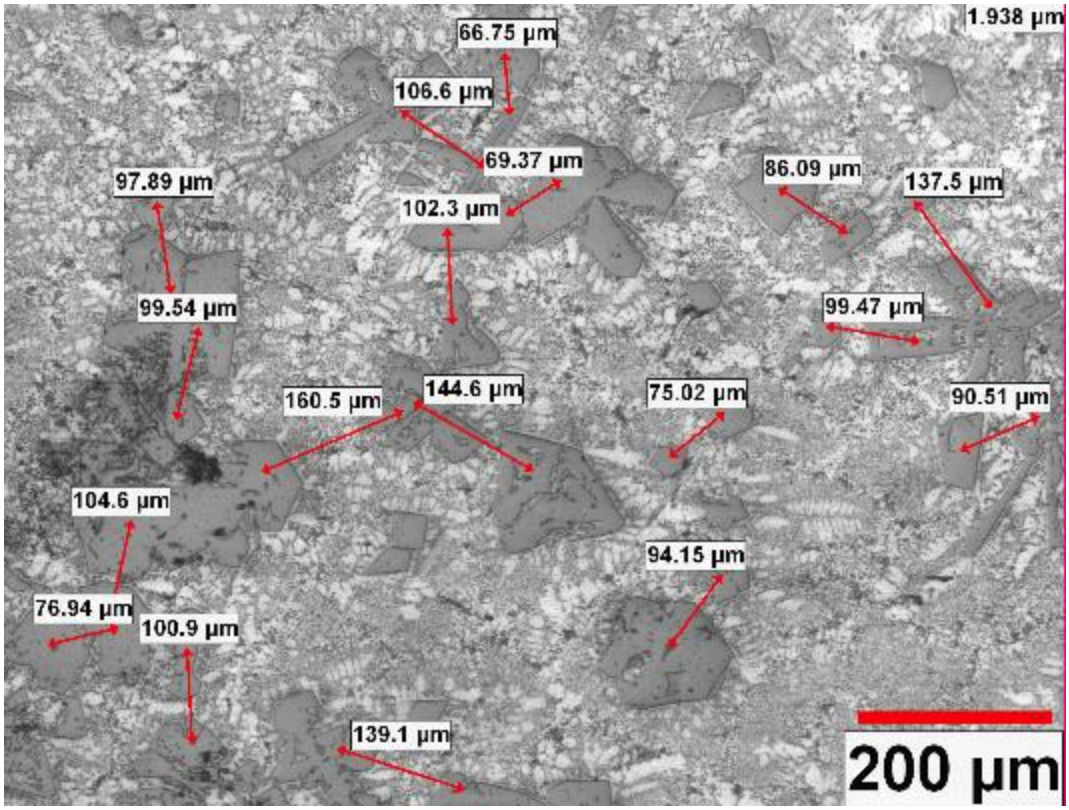

Figure 74: Interspacing between primary Silicon particles for Al-25%Si polished with 800 grit size sand paper (Average spacing 102.87µm)

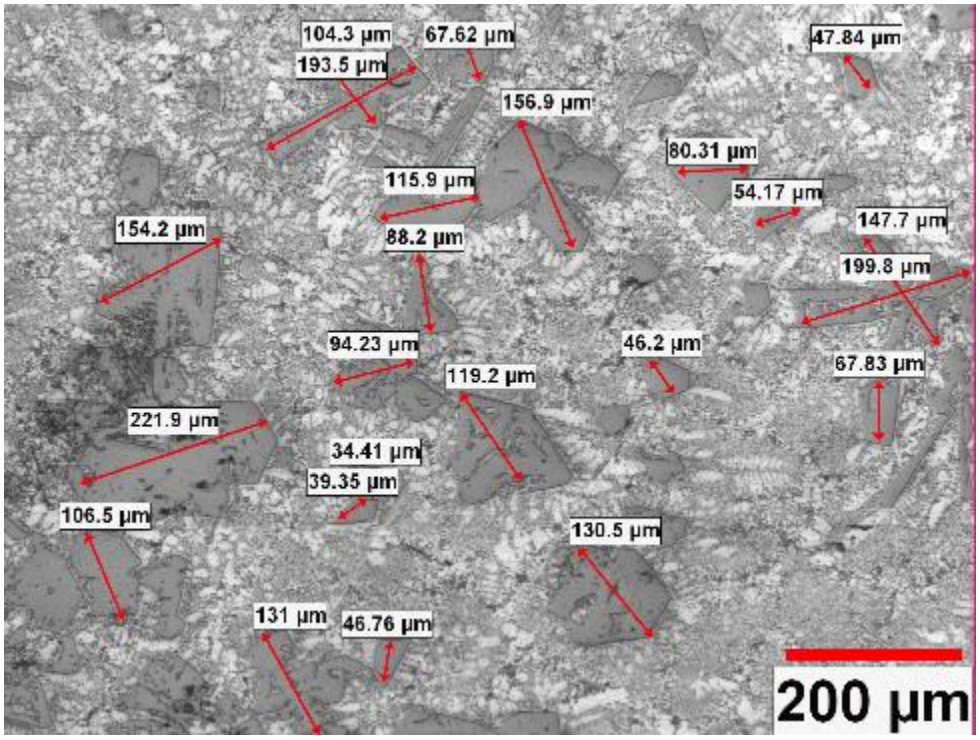

Figure 75: Size of primary Si in Al-25%Si sample polished with 800 grit sand paper (Average size 106.45µm)

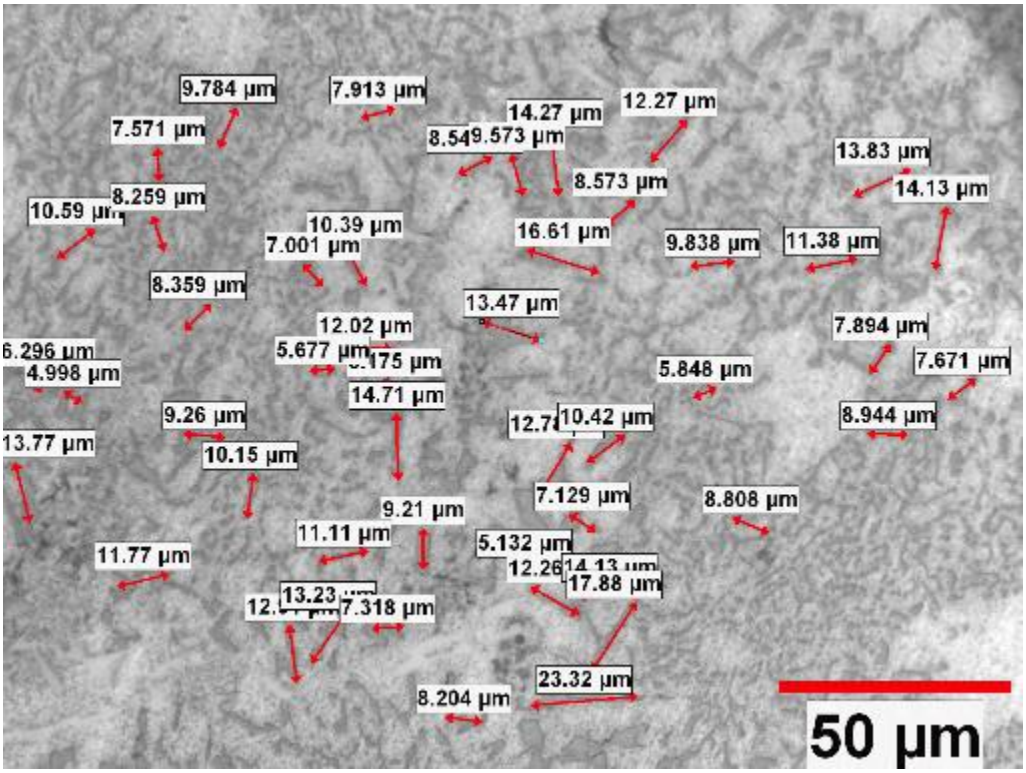

Figure 76: Al-32%Si sample showing size of eutectic Silicon at 500x (Average size 9.89µm)

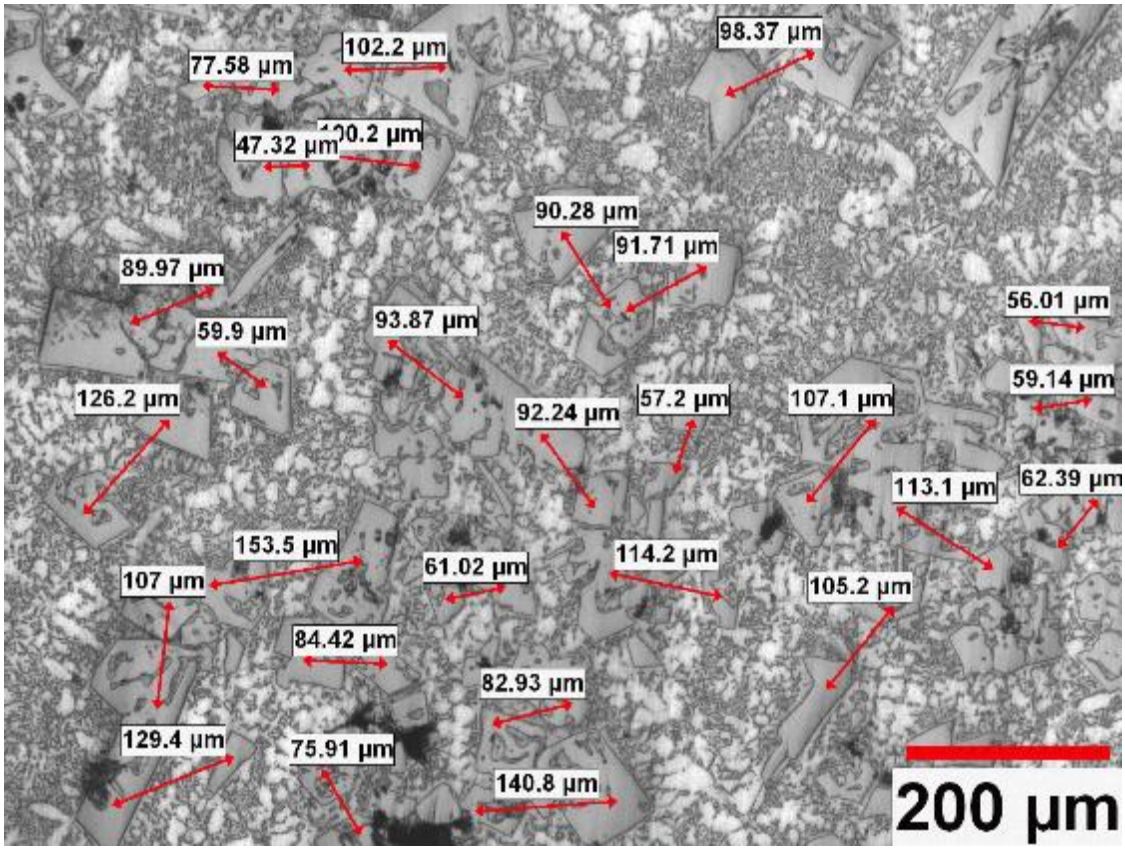

Figure 77: Interparticle spacing between primary Si particles in Al-32%Si sample polished with 800 grit size sand paper (Average spacing 92.11µm)

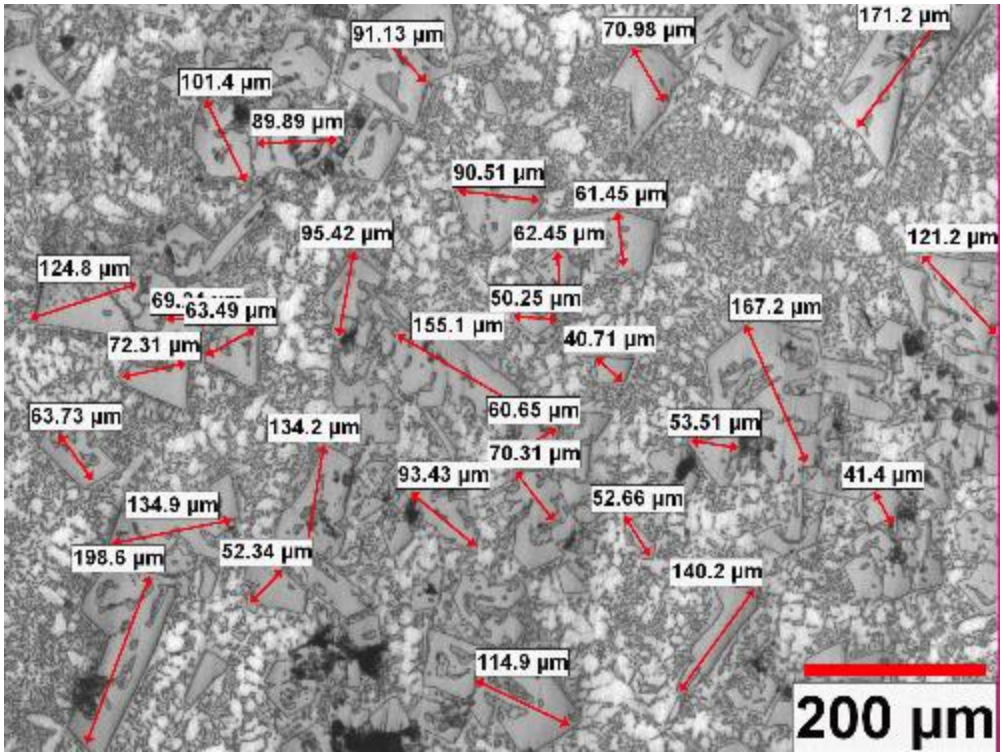

Figure 78: Size of Primary Si particles in Al-32%Si sample polished with 800 grit size sand paper (Average size 93.86µm)

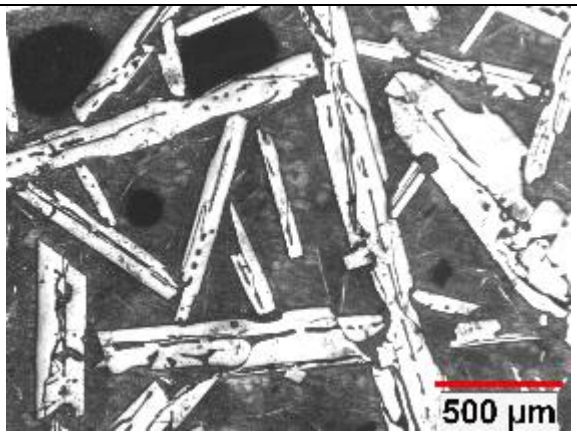

Figure 79: Microstructure of Al-50%Si polished with 240 grit sand paper showing porosity

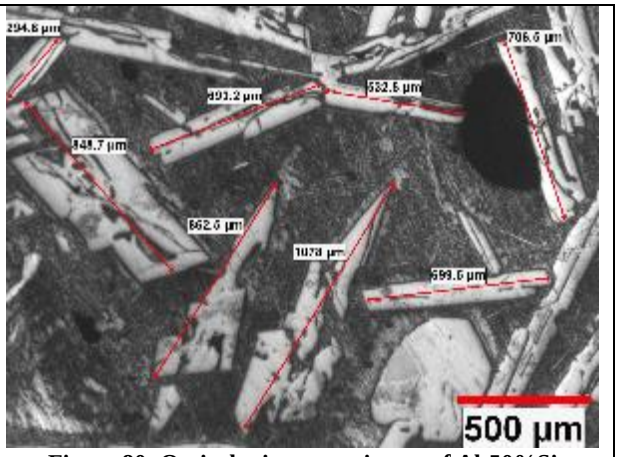

Figure 80: Optical microscope image of Al-50%Si showing size of primary Si

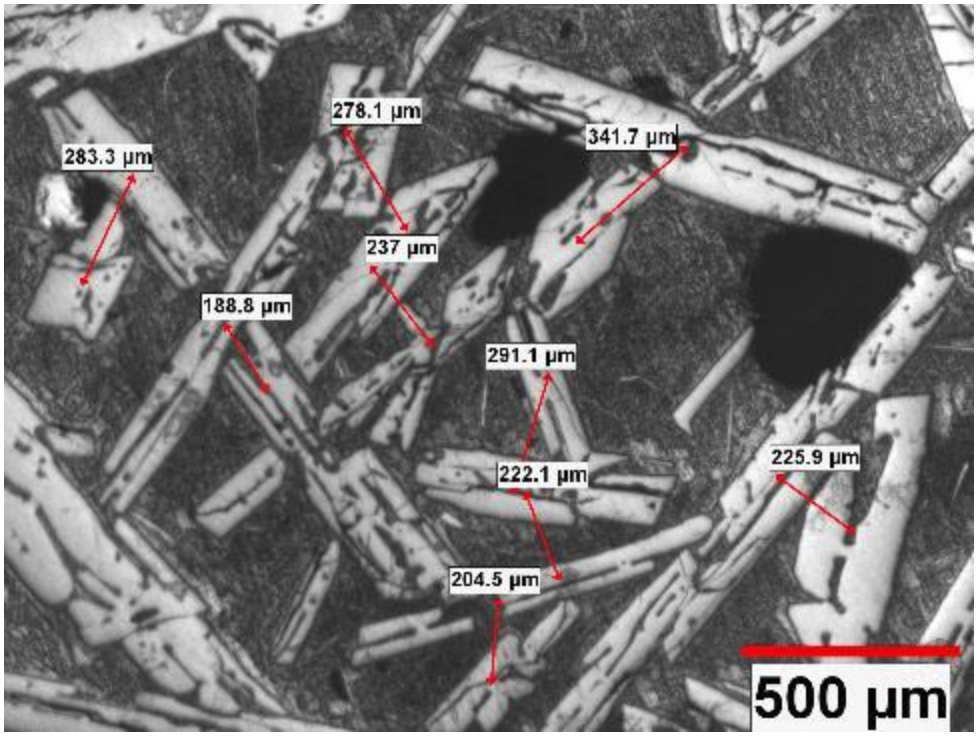

Figure 81: Interparticle separation in Al-50%Si polished by 240 grit size sand paper

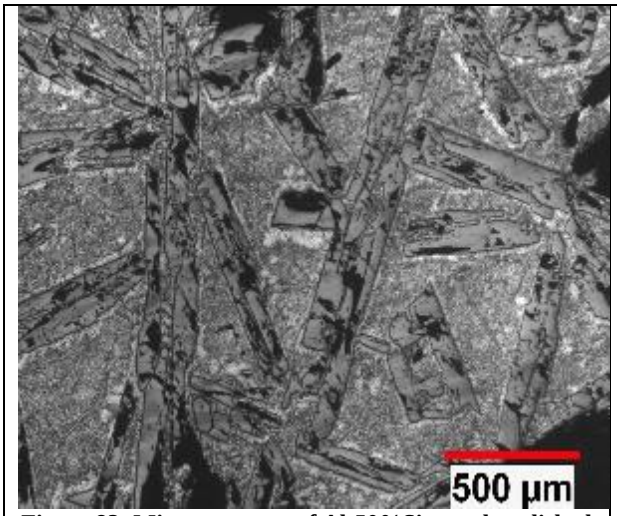

Figure 82: Microstructure of Al-50%Si sample polished with 800 grit size sand paper

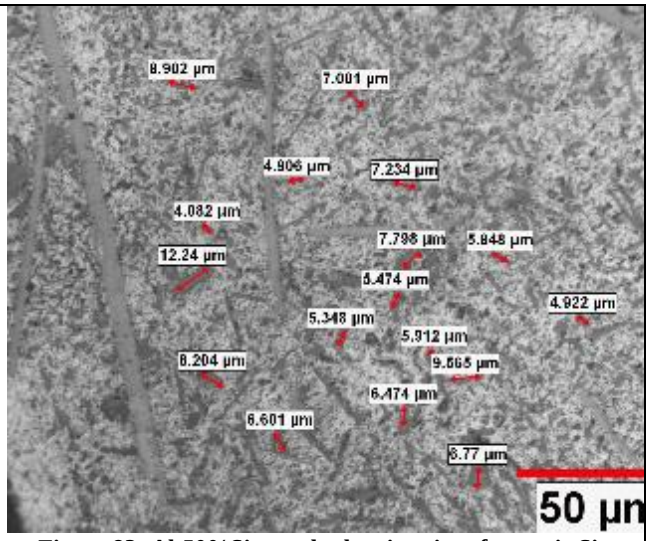

Figure 83: Al-50%Si sample showing size of eutectic Si

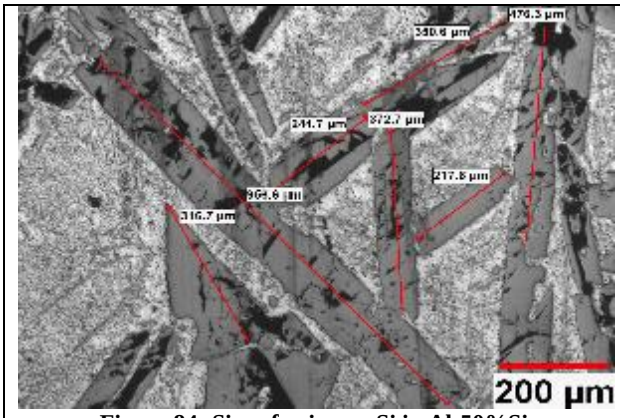

Figure 84: Size of primary Si in Al-50%Si

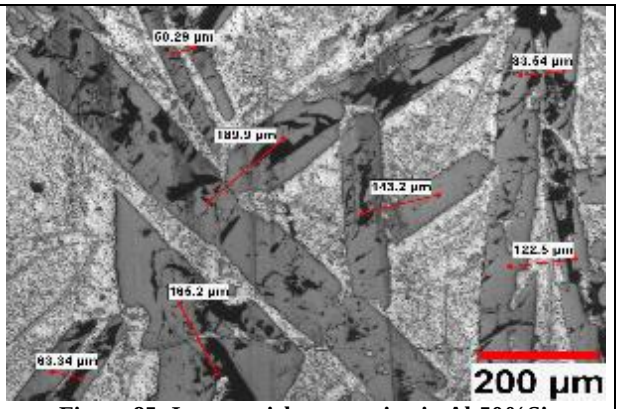

Figure 85: Interparticle separation in Al-50%Si

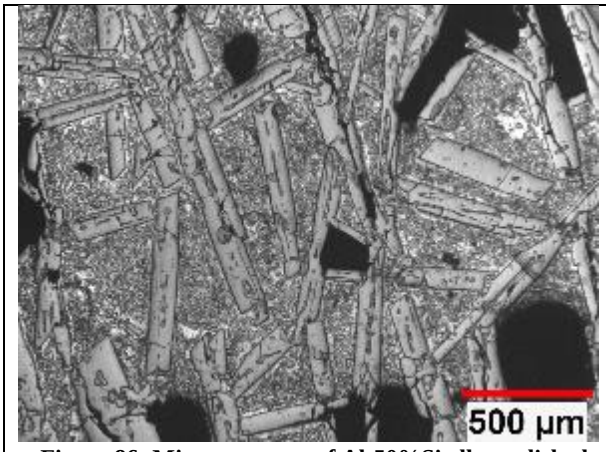

Figure 86: Microstructure of Al-50%Si alloy polished with 1200 grit size sand paper

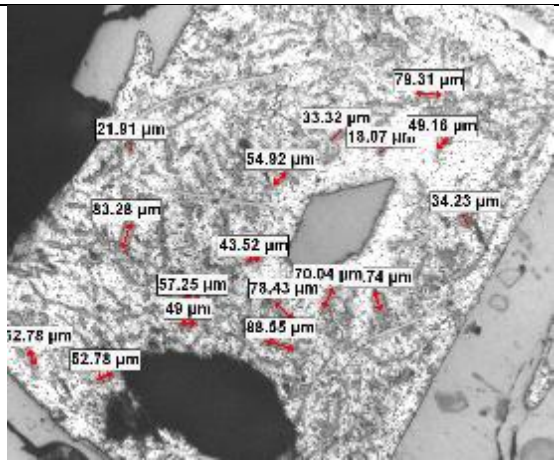

Figure 87: Size of eutectic Si in Al-50%Si sample polished with 1200 grit sand paper

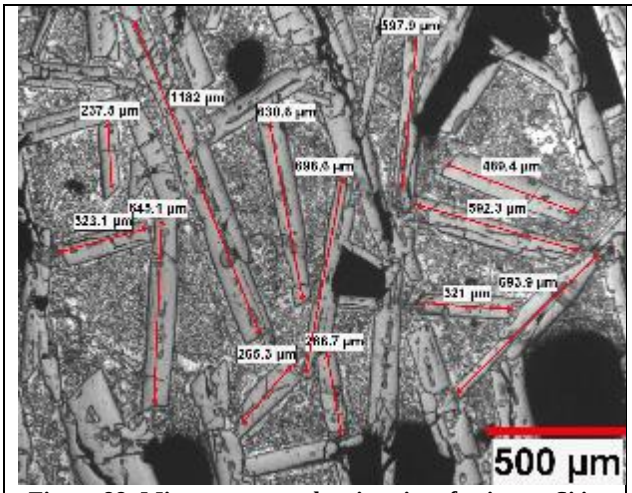

Figure 88: Microstructure showing size of primary Si in Al-50%Si sample polished with 1200 grit sand paper

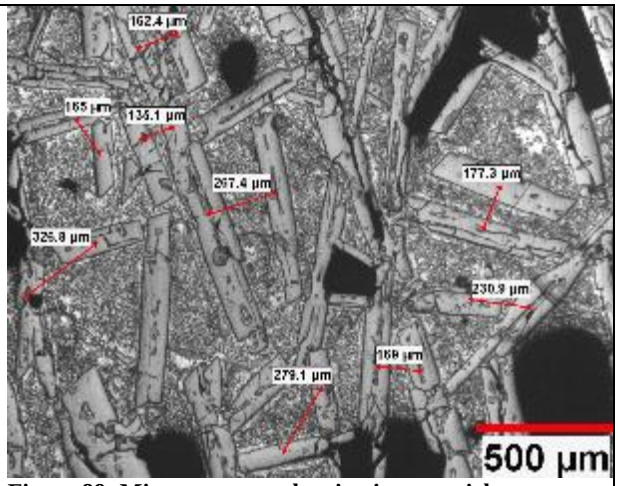

Figure 89: Microstructure showing interparticle separation in Al-50%Si sample polished with 1200 grit sand paper

Appendix C

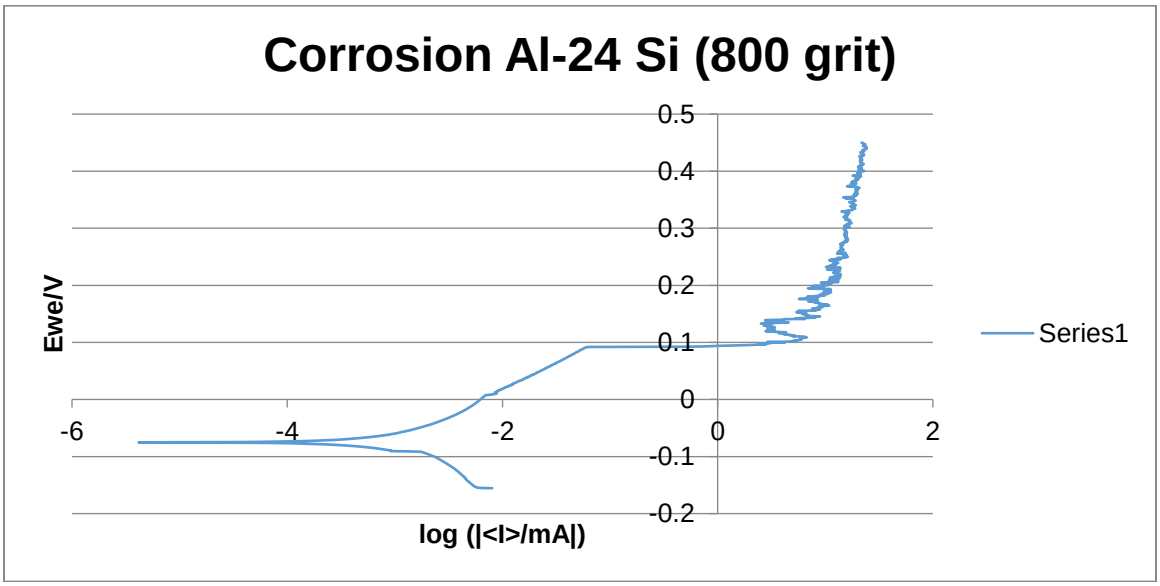

Figure 90: Corrosion Al-24 Si alloy (800 grit) – Corrosion test result.

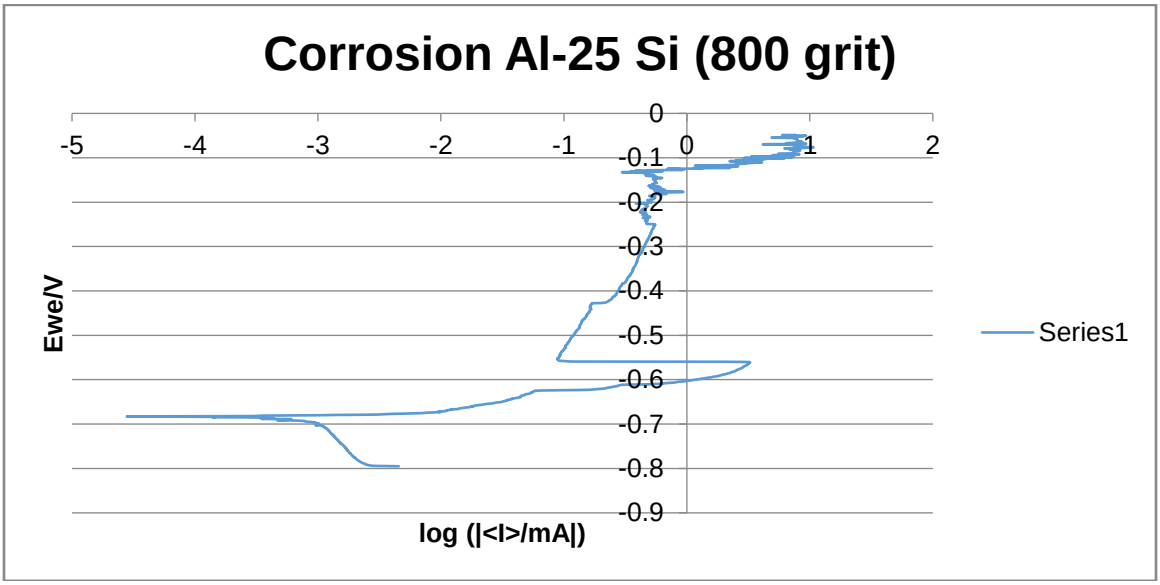

Figure 91: Corrosion Al-25 Si alloy (800 grit) – Corrosion test result.

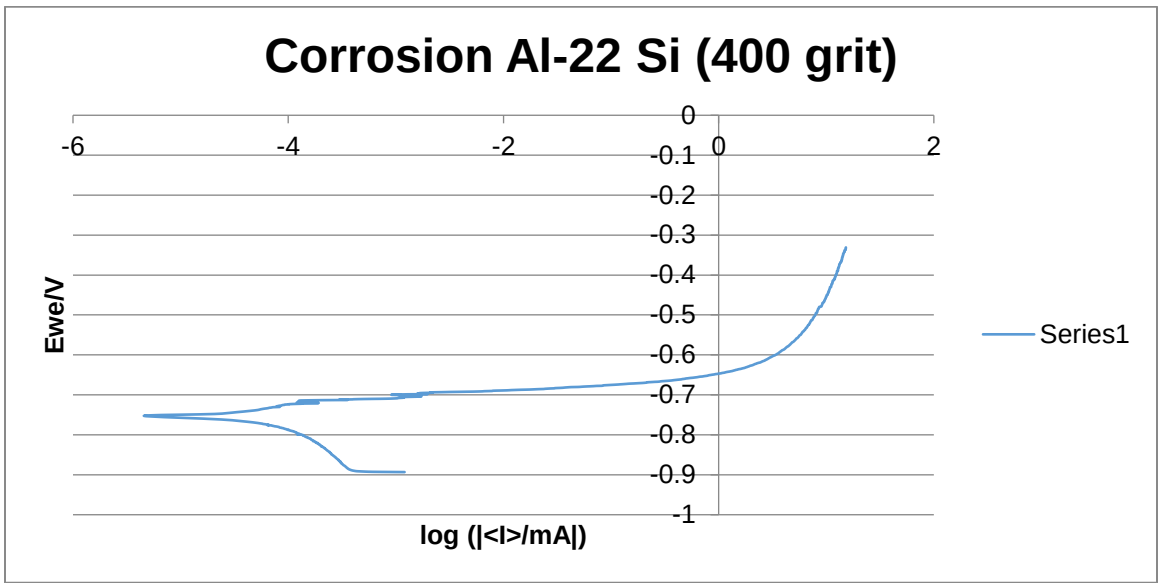

Figure 92: Corrosion Al-22 Si alloy (400 grit) – Corrosion test result.

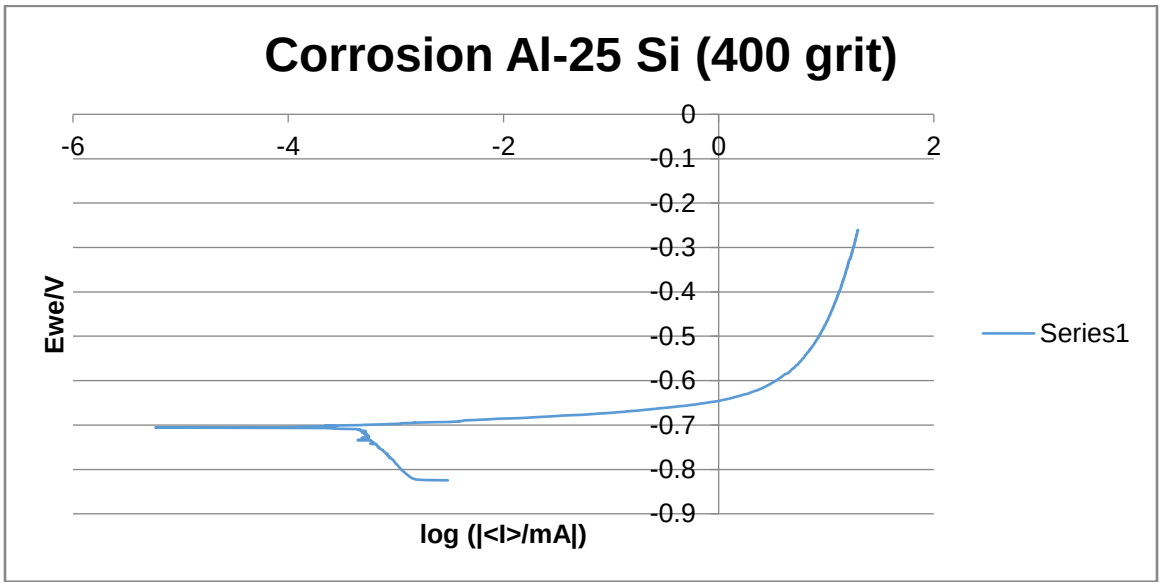

Figure 93: Corrosion Al-25 Si alloy (400 grit) – Corrosion test result.

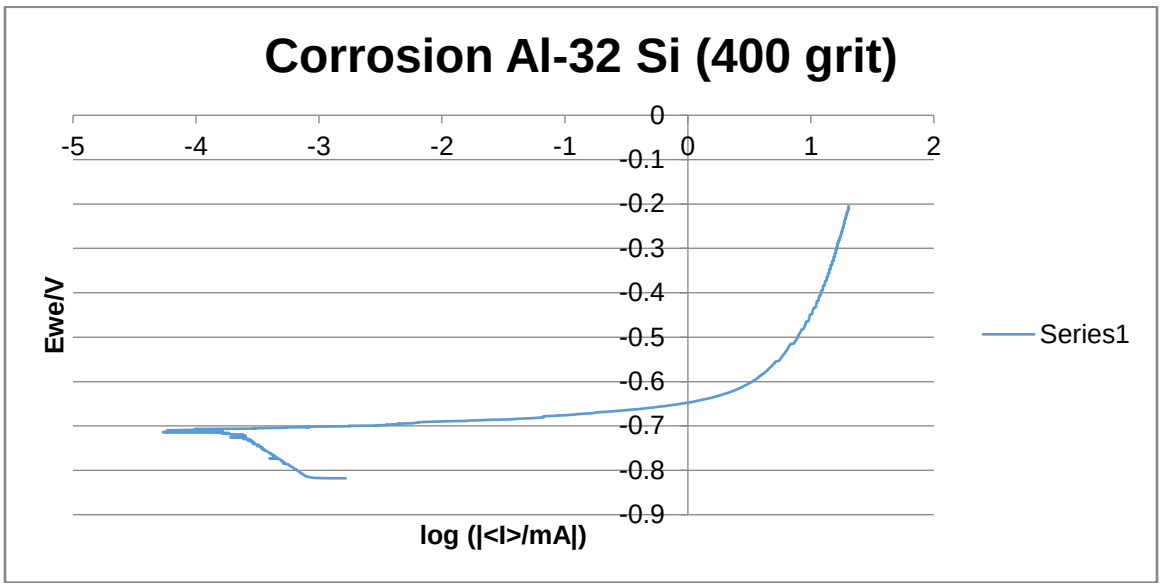

Figure 94: Corrosion Al-32 Si alloy (400 grit) – Corrosion test result.

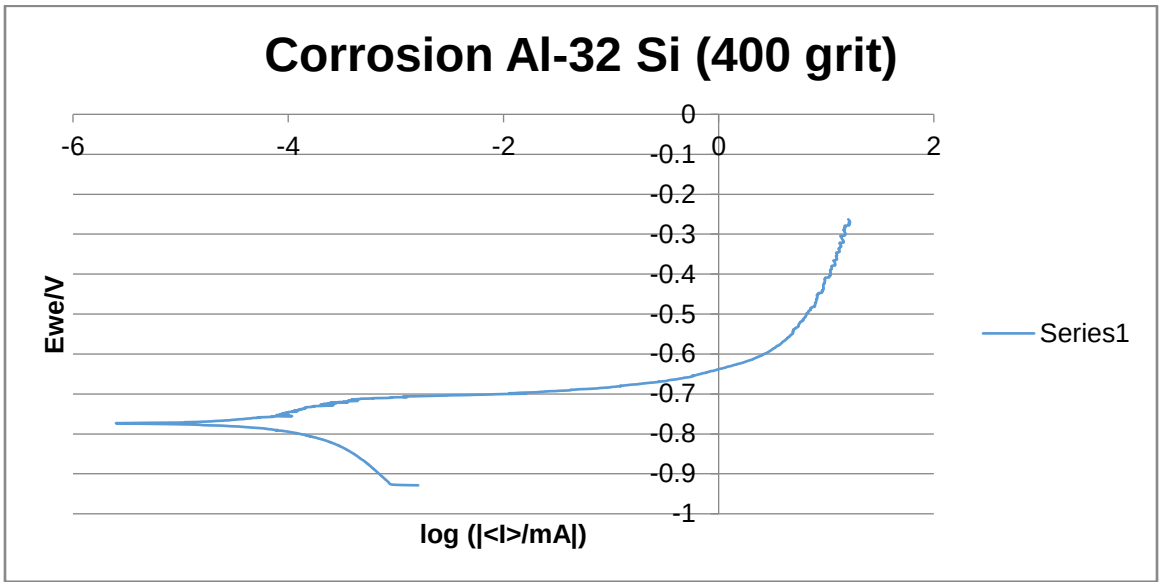

Figure 95: Corrosion Al-32 Si alloy (400 grit) – Corrosion test result.

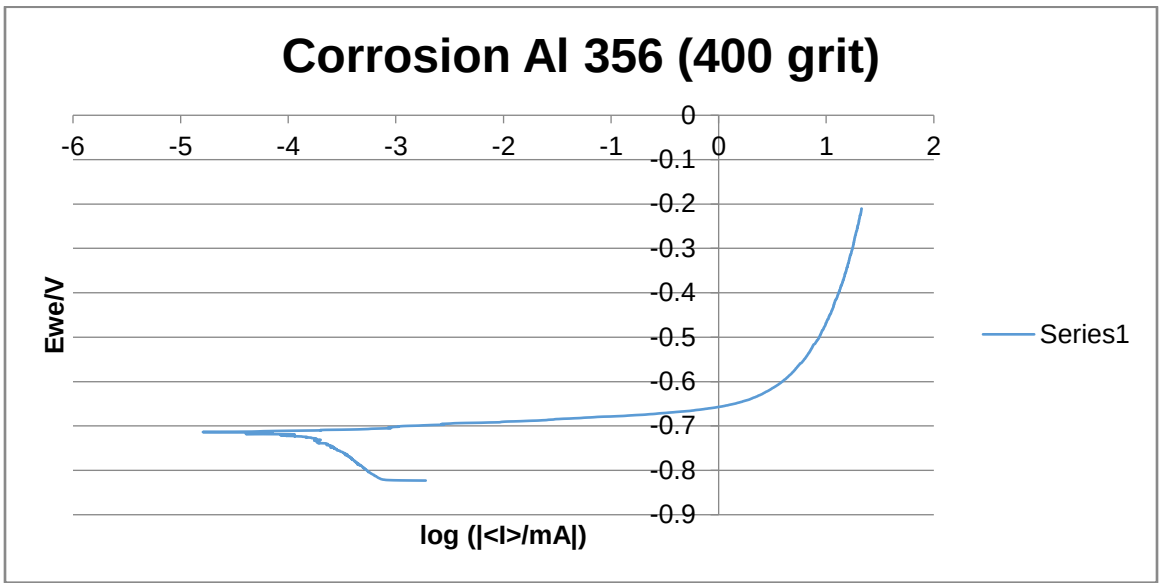

Figure 96: Corrosion Al 356 alloy (400 grit) – Corrosion test result.

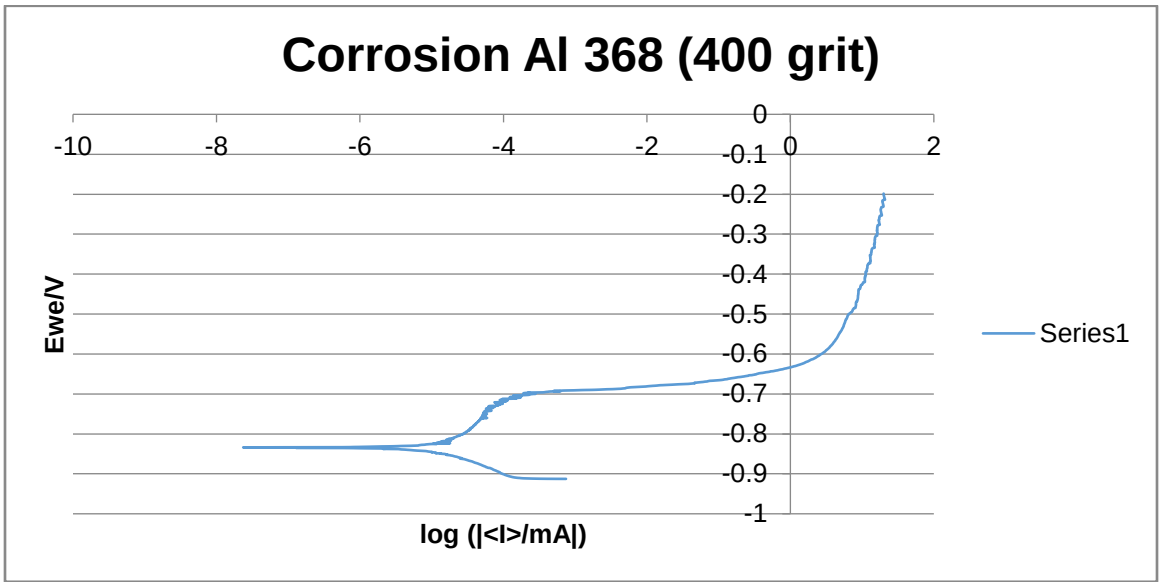

Figure 97: Corrosion Al 368 alloy (400 grit) – Corrosion test result.

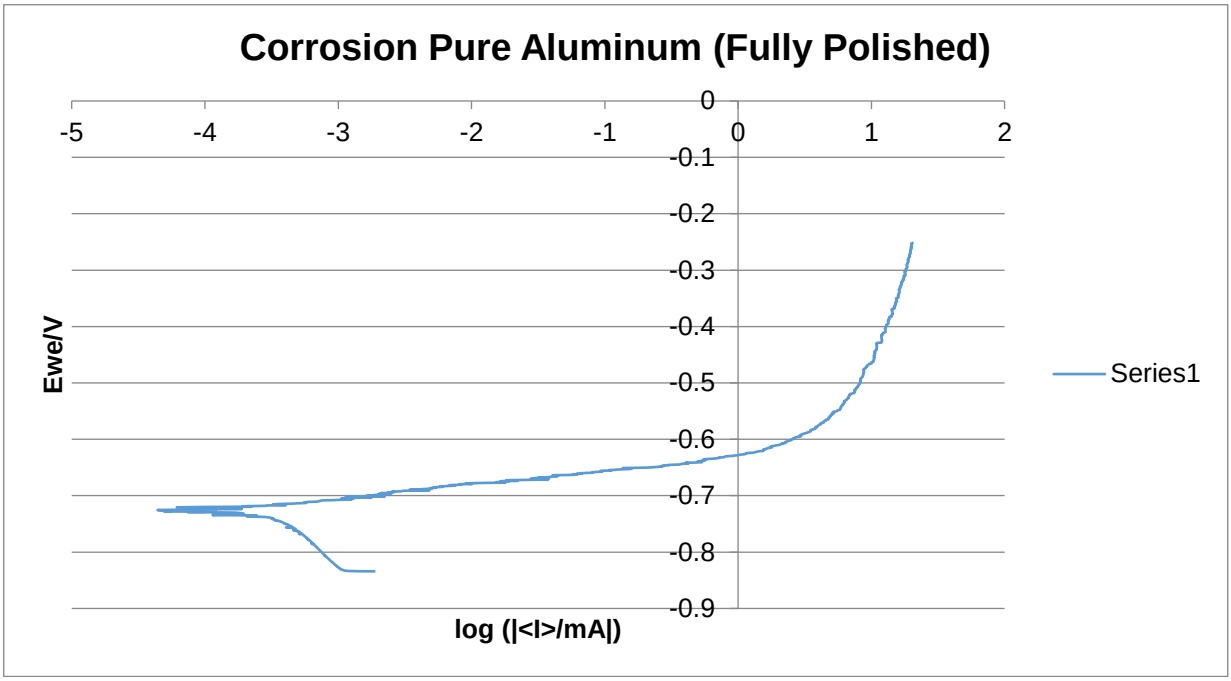

Figure 98: Pure Aluminum (Fully Polished – 1 micrometer) Corrosion test result.

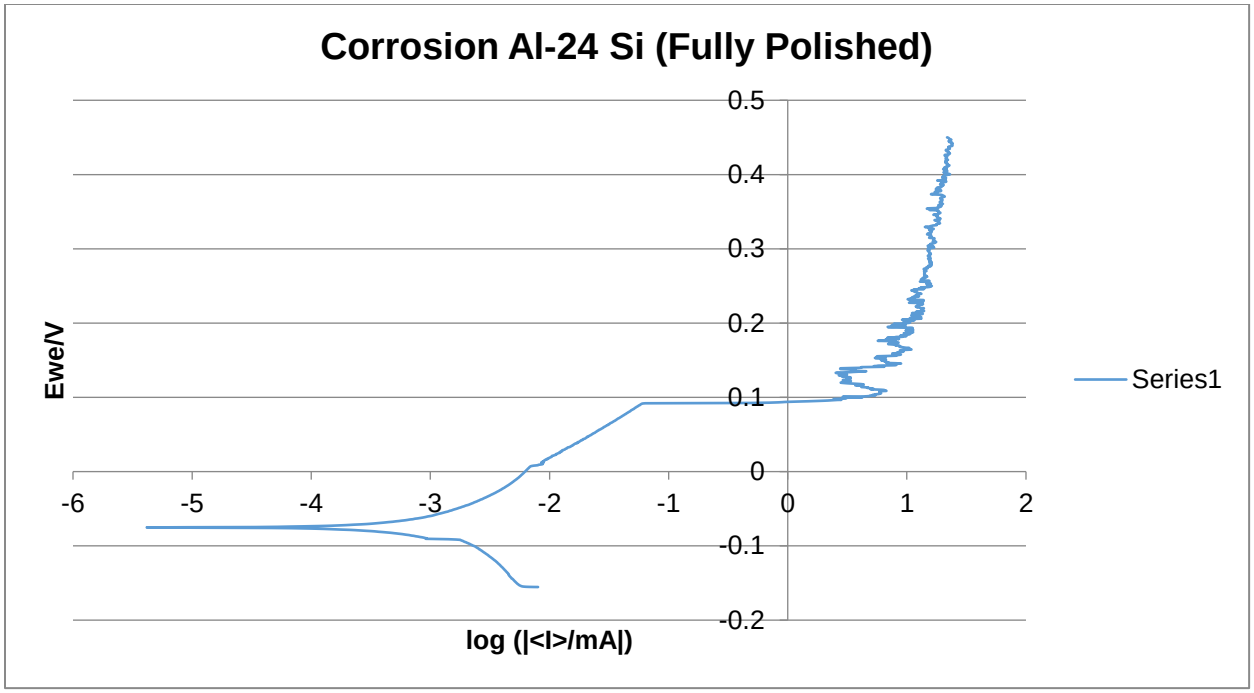

Figure 99: Corrosion results for fully polished Al-24%Si samples

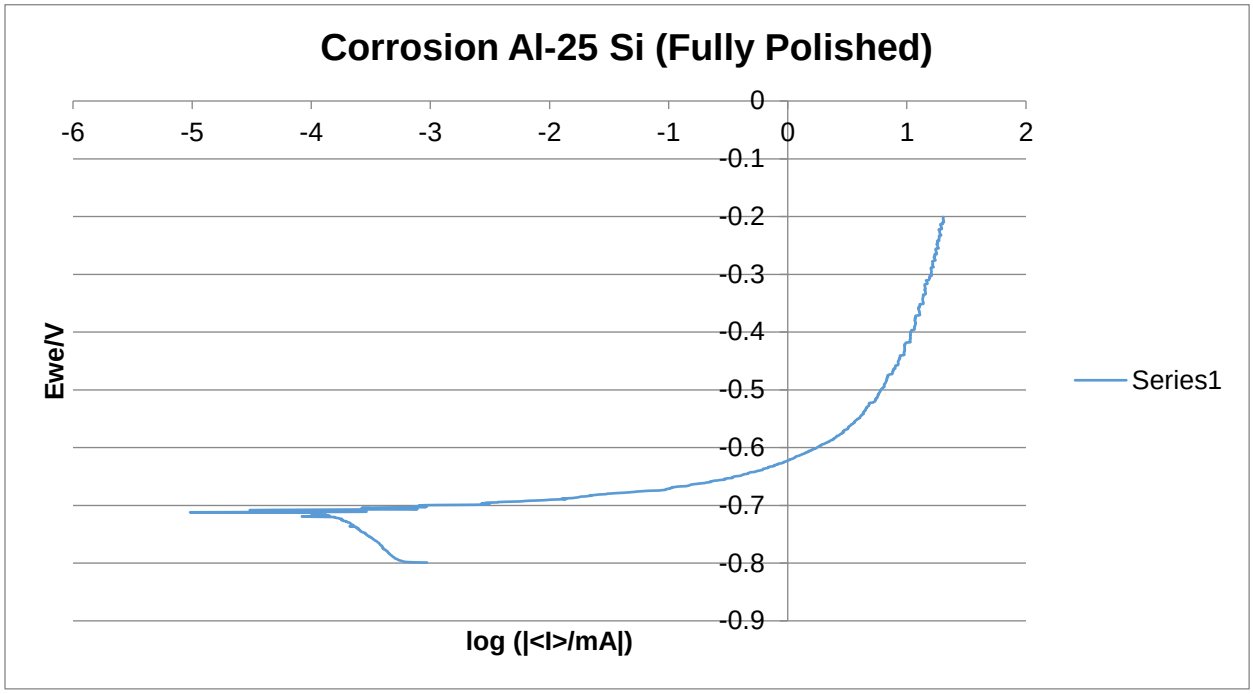

Figure 100: Corrosion results for fully polished Al-25%Si sample

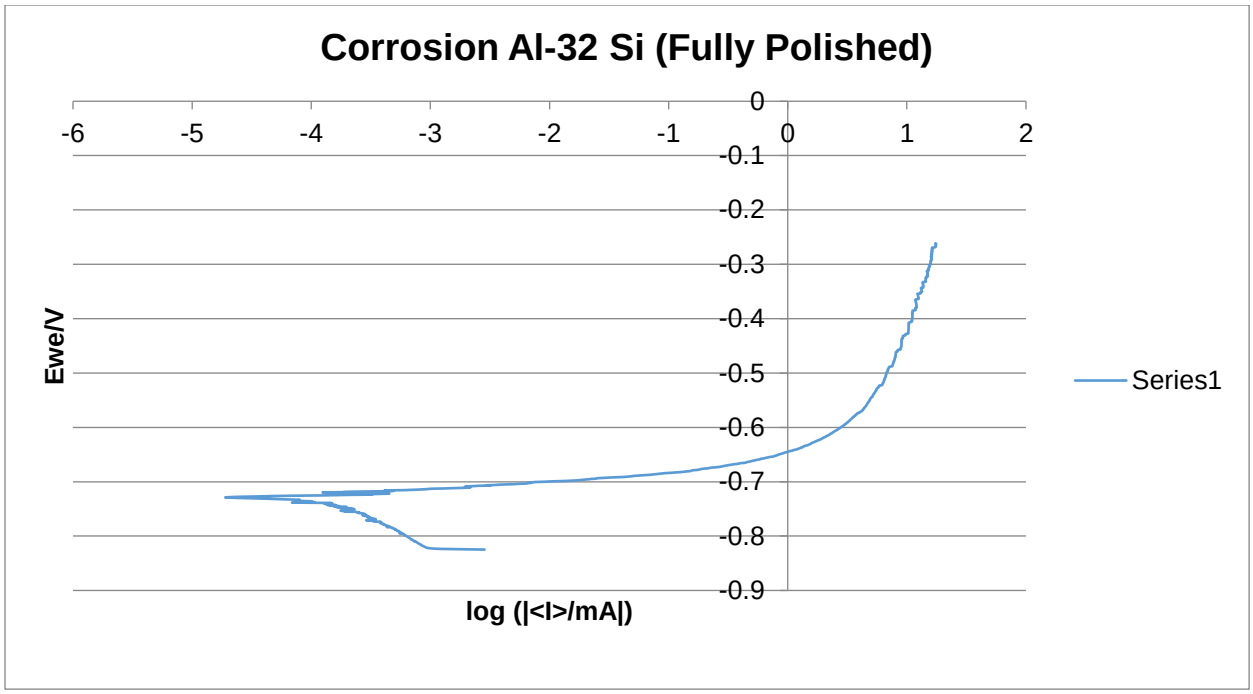

Figure 101: Corrosion results for fully polished Al-32%Si sample